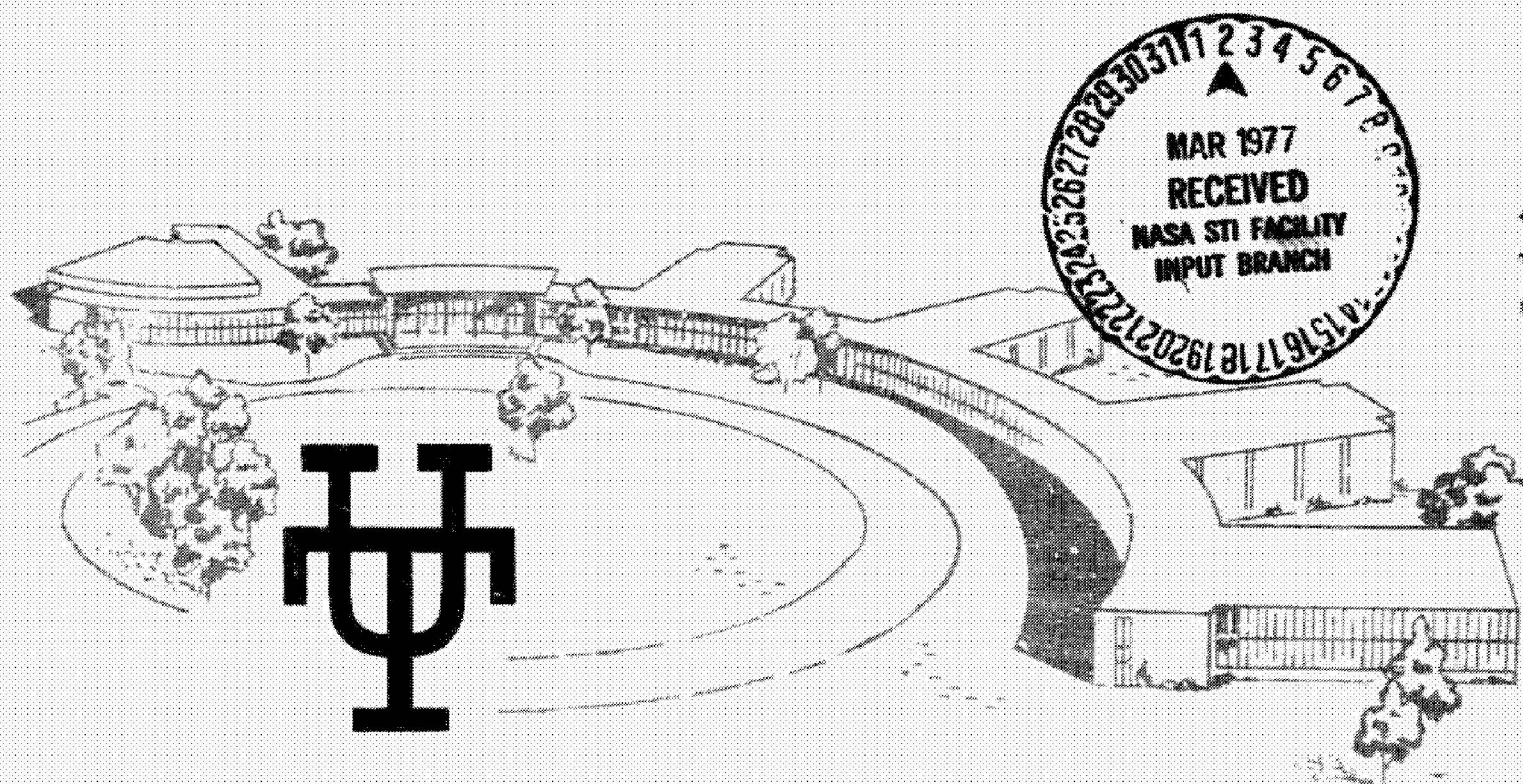
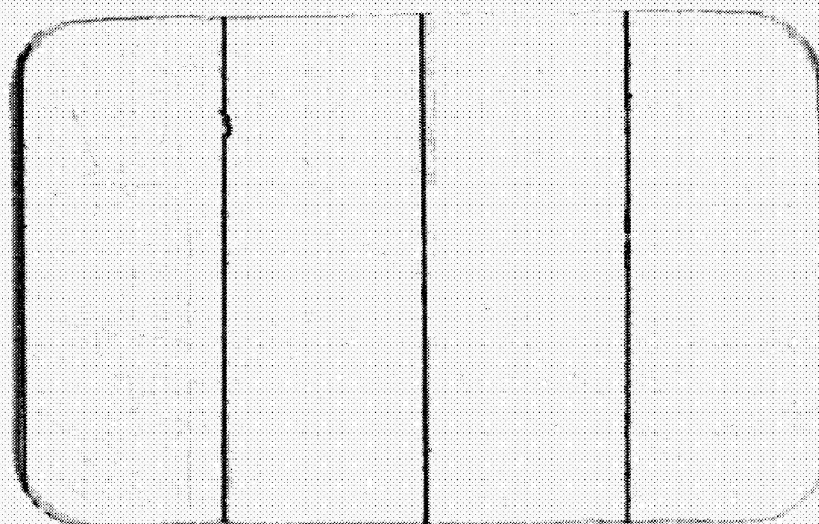


(NASA-CR-149589) ACOUSTIC SOURCE LOCATION
IN A JET-BLOWN FLAP USING A
CROSS-CORRELATION TECHNIQUE Final Report
(Tennessee Univ. Space Inst., Tullahoma.)
176 p HC A-3/EF A01

N77-17830

Unclas

CSCI 203 G3/71 15617



THE UNIVERSITY of TENNESSEE SPACE INSTITUTE

Tullahoma, Tennessee

ACOUSTIC SOURCE LOCATION IN A
JET-BLOWN FLAP USING A
CROSS-CORRELATION TECHNIQUE

by

Robert S. Becker and James R. Maus

Final Report for
NASA Grant NGR 43-001-135

The University of Tennessee Space Institute
Tullahoma, Tennessee

February 1977

FORWARD

This research was supported by the National Aeronautics and Space Administration under Grant NASA NGR-43-001-135 which was administered by Mr. Meyer Reshotko, V-STOL-NOISE Division, Lewis Research Center, Cleveland, Ohio. Appreciation is expressed to Mr. Reshotko for his assistance during all phases of this project. Appreciation is also due to Mr. Jeff Essary and Mr. Mike MacKinnon in the Operations Branch.

ABSTRACT

The results of an experimental investigation which was performed in an attempt to locate the acoustic sources in a jet-blown flap (jet-flap) are presented. The method employed was a direct correlation technique which is based upon the theoretical work of Curle. The acoustic source strength distribution in the turbulent flow field was measured for two far-field microphones at 45° above and below the plane of the flap surface by cross-correlating a processed signal from an inclined hot-film anemometry probe with the signal from the appropriate far-field microphone. An estimate of the contribution made by the sources associated with the fluctuating pressure on the flap surface to the sound received at a far-field microphone was made by cross-correlating the processed signals of microphones which were embedded in the flap surface with the far-field microphone signals. In addition, detailed fluid dynamic measurements were made in the flow field of the jet-flap using dual-sensor hot-film anemometry probes.

It was concluded that the secondary mixing region which is formed downstream of the flap trailing edge is a region of high acoustic emission, and that the acoustic sources there are highly directional, radiating much more

effectively to the far-field microphone below the flap than to the one above it. Furthermore, a minor portion of the sound received at the 45° -microphones is generated by the pressure fluctuations on the flap surface, and that this contribution comes from a small surface area near the flap trailing edge. It appears that a large portion of the sound received at the -45° -microphone was due to an edge amplification effect which was theoretically predicted by Ffowcs Williams and Hall

TABLE OF CONTENTS

CHAPTER		PAGE
I.	INTRODUCTION	1
II.	THEORETICAL DEVELOPMENT FOR ACOUSTIC SOURCE	
	LOCATION.	8
	Derivation of an Inhomogeneous Wave	
	Equation.	8
	The Lighthill Analogy.	10
	General Solution of the Wave Equation. . .	12
	Approximations for the Jet-Blown Flap. . .	15
	Correlation Analysis	21
	Modifications for Measurement.	24
III.	EXPERIMENTAL EQUIPMENT AND DATA ACQUISITION. . .	29
	The Jet Facility	29
	The Test Set-Up.	33
	Data Acquisition from Cross-Correlation	
	Analysis.	38
	Data Acquisition for Fluid-Dynamic	
	Measurements.	45
	The Cross-Correlation Analysis	51
IV.	FLUID DYNAMIC MEASUREMENTS	56
	General Flow Characteristics	56
	The Axial Mean Velocity Profiles	59
	The Axial Turbulence Intensity Profiles. .	65

CHAPTER	PAGE
The Transverse Mean Velocity Profiles . .	71
The Transverse Turbulence Intensity	
Profiles	74
The Reynold's Stress Profiles	79
V. ACOUSTIC MEASUREMENTS AND SOURCE LOCATION . . .	86
Introduction.	86
Directivity and Spectra of the Far-Field	
Sound.	86
Acoustic Source Distribution on the	
Flap Surface	95
Acoustic Source Distribution in the Flow	
Field.	109
VI. SUMMARY AND CONCLUSIONS	125
BIBLIOGRAPHY	133
APPENDICES	137
A. USE OF A HOT-FILM PROBE FOR THE MEASUREMENT OF	
M_x	138
B. PROBE NOISE	146
VITA	160

LIST OF FIGURES

FIGURE		PAGE
1.	Jet Blown Flap.	2
2.	Boeing EOW Prototype.	2
3.	Jet-Flap Model.	6
4.	Notation for Eq. (2-9).	13
5.	Jet-Flap Configuration.	16
6.	Vector Notation for the Jet-Flap Configuration. .	17
7.	Acoustic Source Measurement Scheme.	28
8.	Test Hardware	30
9.	The Test Model.	32
10.	Overhead View of Test Set-Up.	34
11.	Traversing Mechanism.	36
12.	Probe-Mounting Configuration.	37
13.	Test Set-Up in Anechoic Chamber	39
14.	DISA 55R02 Probe and Probe Holder	40
15.	Comparison of Linearized and Unlinearized Probe Calibration Curves	42
16.	Data Acquisition for the Cross-Correlation Analysis	44
17.	DISA 55R51 Probe and Associated Geometry.	46
18.	Data Acquisition for the Dual Sensor Probe Fluid Dynamic Measurements	48

FIGURE	PAGE
19. Cross-Correlation Analysis.	54
20. Flow Features of the Slot-Nozzle Jet and the Jet Flap	57
21. Axial Mean Velocity Profiles for the Slot-Nozzle Jet.	60
22. Centerline Axial Velocity Decay	62
23. Axial Mean Velocity for the Slot-Nozzle Jet with Flap	63
24. Axial Turbulence Intensity Profiles for the Slot- Nozzle Jet	66
25. Axial Turbulence Intensity Profiles for the Slot- Nozzle Jet with Flap	68
26. Maximum Axial Turbulence Intensities.	69
27. Transverse Mean Velocity Profiles for Slot-Nozzle Jet.	72
28. Transverse Mean Velocity Profiles for Slot-Nozzle Jet with Flap.	73
29. Transverse Turbulence Intensity Profiles for Slot- Nozzle Jet	75
30. Maximum Transverse Turbulence Intensities	76
31. Transverse Turbulence Intensity Profiles for Slot Nozzle with Flap	78
32. Reynold's Stress Profiles for Slot-Nozzle Jet	81
33. Reynold's Stress Profiles for Slot Nozzle with Flap	82

FIGURE	PAGE
34. Maximum Values of the Reynold's Stress.	84
35. Sound Pressure Level Contours	87
36. Intensity Level vs. Jet Exit Velocity	92
37. 1/3-Octave Spectra, X_1X_2 Plane.	93
38. 1/3-Octave Spectra.	97
39. Autocorrelation Functions of Embedded Microphones .	99
40. Autocorrelation Functions of the Far-Field Microphones.	100
41. Cross Correlation of Embedded Microphone 1 and the Far-Field Microphones.	106
42. Cross Correlation of Embedded Microphone 2 and the Far-Field Microphone at -45°	108
43. Variation of $\sqrt{m_x^2}$ with Downstream Distance for the Jet-Flap at Mach =	111
44. One Third Octave Spectra of $\sqrt{m_x^2}$	113
45. Turbulence Autocorrelation Functions ($X_1 = 7$; Primary M.R.).	116
46. Shear and Self Noise Components ($X_1/h = 15$, Sec. Mix. Reg.)	117
47. Axial Distribution of Acoustic Source Strength in the Jet-Flap Flow Field for the $+45^\circ$ -Microphone.	120
48. Axial Distribution of Acoustic Source Strength in the Jet-Flap Flow Field for the -45° -Microphone.	122

FIGURE	PAGE
49. Autocorrelation Function of m_x at $X_1/h = 4$147
50. Probe Noise Intensity Levels149
51. Test Schematic151
52. Space-time Correlation Curves for a Circular Jet (2-Inch Diameter; Exit Mach Number = .3).154
53. Effect of Probe Noise on the Value of $S_{p,m_x}(-\tau_o)$ Measured for $\bar{f}_o = 6300$ Hz157
54. The Effect of Probe Noise Contamination on the Measurement of $S_{p,m_x}(-\tau_o)$158

NOMENCLATURE

A	Surface which bounds a region R that contains a turbulent flow field embedded in an ambient atmosphere at rest
A, B, b	Constants in hot-film probe response equation
c_o	Sonic velocity in the ambient atmosphere at rest
c^*	Sonic velocity at the nozzle exit plane
$(CF)_p$	Correction factor for anemometry data
dA	Area element on surface A
dV	Volume element in the region R
E_o	Anemometer output voltage when there is no flow
e	Linearizer output voltage
e_n, e_z, e_p	Unit vectors in a coordinate system attached to the inclined hot-film probe
e_ϵ, e_ψ	Unit vectors in a reference coordinate system for the hot-film probe
f	Frequency
f_o	Center frequency of a bandpass filter
f_b	Signal bandwidth
h	Slot-nozzle height

ℓ	Characteristic length of the turbulent flow field
M	Instantaneous momentum vector
M_{eff}	Effective corling momentum vector
M_ϵ, M_ψ, M_z	Instantaneous momentum components in $\epsilon\psi z$ -system
$\bar{M}_\epsilon, \bar{M}_\psi, \bar{M}_z$	Mean values of the $\epsilon\psi z$ -momentum components
m_ϵ, m_ψ, m_z	Deviation of M_ϵ, M_ψ, M_z from their respective mean values
M_n, M_p	Instantaneous momentum components in npz -system
\bar{M}_n, \bar{M}_p	Mean values of M_n, M_p
m_n, m_p	Deviation of M_n, M_p from \bar{M}_n, \bar{M}_p
M_x	Instantaneous momentum component in the x -direction
$(M_x)_{\text{ref}}$	Reference mass flux
\bar{M}_x	Mean value of M_x
m_x	Deviation of M_x from \bar{M}_x
\ddot{m}_x	$\partial^2 m_x / \partial t^2$
n_i	Unit vector normal to dA
p	Pressure
\dot{p}	$\partial p / \partial t$
p'	Acoustic pressure

\hat{p}_i	Fluctuation of the resultant force which dA exerts upon the fluid
p_m	Local ensemble averaged value of the pressure
p_o	Pressure in the ambient atmosphere at rest
q_i	Components of the instantaneous velocity vector; q_1, q_2, q_3
R	Region containing the ambient atmosphere at rest and the embedded turbulent flow field
$R_{p'p'}$	Autocorrelation function of the acoustic pressure
$R_{p'\ddot{m}_x}$	Cross-correlation function of p' and \ddot{m}_x
$R_{p'\ddot{m}_x}$	Cross-correlation function of p' and \ddot{m}_x
$R_{p'\ddot{m}_x^2}$	Cross-correlation function of p' and \ddot{m}_x^2
$R_{p'\dot{p}}$	Cross-correlation function of p' and \dot{p}
R_{pp}	Autocorrelation function of \dot{p}
r	Distance between field point and source point = $ x_i - y_i $
S	$1/c_o^2 (p - c_o^2 \rho)$
$S_{p'm_x}$	Cross spectral density function of p' and m_x
$S(\omega)$	Power spectral density function
T_{ij}	$(\rho q_i q_j - \tau_{ij})$

t	Time
t^*	Retarded time = $t - \tau_0$
(TSC)	Total surface contribution to the sound at a far-field position
V	Region occupied by the turbulent flow
V_1, V_2, V_3	Instantaneous velocity components in the X_1, X_2, X_3 directions
$\bar{V}_1, \bar{V}_2, \bar{V}_3$	Mean values of V_1, V_2, V_3
v_1, v_2, v_3	Deviation of V_1, V_2, V_3 from $\bar{V}_1, \bar{V}_2, \bar{V}_3$
V_n	Velocity component normal to hot-film probe sensor-element
V_{eff}	Effective cooling velocity vector
X_1, X_2, X_3	Axis of a coordinate system whose origin is in the nozzle exit plane
X_{2-MTI}	X_2 -coordinate corresponding to point of maximum turbulence intensity
x_i	Coordinates of a field point
y_i	Coordinates of a source point
<u>Greek</u>	
α	Direction sensitivity constant for inclined hot-film probe
β	Proportionality constant for the linearizer output voltage

γ	Ratio of specific heats
ϵ	A number much less than 1
ζ	Angle from jet-axis in X_1X_3 -plane
θ	Angle between n_i and x_i
κ	Linearizer constant
$\bar{\Lambda}_3$	v_3 -component of mean vorticity vector
∇	Acoustic source strength per unit volume
ϵ, ψ	Coordinate axes used for geometry of hot-film probe sensor-element
ρ	Fluid density
ρ_0	Fluid density in the ambient atmosphere at rest
ρ'	Acoustic density
τ, τ'	Arbitrary time increments
τ_0	Acoustic transmission time = r/c_0
τ_p	Value of τ at which the maximum value of a cross-correlation function occurs
τ_{ij}	Components of the instantaneous stress tensor
$(\tau_{ij})_m$	Local ensembled averaged value of viscous stress tensor
τ^*	Reynolds stress
Φ	Axial turbulence intensity

ϕ	Angle from jet-axis in the X_1X_2 -plane
Ω	Transverse turbulence intensity
ω	Angular frequency

CHAPTER I

INTRODUCTION

A promising contender for use on STOL (Short Takeoff and Landing) aircraft is the jet-blown flap (jet flap). This device, which is shown in Figure 1, consists of an airfoil with a trailing edge flap, whose upper surface is blown tangentially by a high velocity slot-nozzle jet which would be supplied via the bypass flow of a turbofan engine. Another design which is similar in principle to the jet-flap is the engine over-the-wing concept (EOW). In this configuration, the aircraft's engines are mounted above the wing in such a manner that the upper wing surface is blown by the full exhaust of the jet. Figure 2 shows a prototype of an aircraft using the EOW concept which is currently under development at the Boeing Aerospace Company.

The development of future STOL programs depends on the ability of STOL devices to meet existing Federal jet-noise emission standards. Upper surface blowing (USB) schemes, such as the jet-flap and the EOW, were initially considered to be very attractive from the acoustic standpoint, since it was believed that the solid surface might act as a shield against high frequency noise produced in the jet mixing region

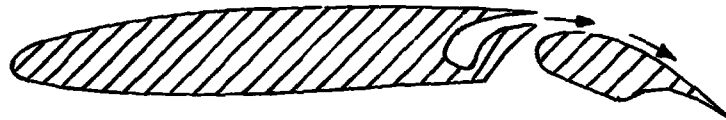


Figure 1. Jet-Blown Flap.

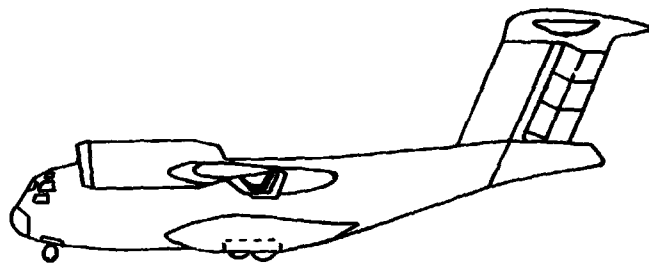


Figure 2. Boeing EOW Prototype.

Source: Foody, J. J. "YC-14 Status Report,"
Air Transportation Meeting of the Society of Automotive
Engineers, Inc., New York, N.Y. SAE paper 760539,
May, 1976.

above it, and, for the EOW, turbomachinery noise produced by the engine. However, early tests [1] of USB models showed that the interaction of the flow field and acoustic field of the jet with the solid surface caused serious noise problems. With the recent progress which has been made in reducing jet-noise by the use of high bypass engines and acoustically treated inlets, it seems possible that a "noise floor" for a STOL aircraft using USB, may be set by the noise which is produced by the device itself.

In order to develop a successful noise suppression program for USB configurations, detailed knowledge of the acoustic sources is required. To date almost everything which is known about the acoustic sources in USB configurations has been derived indirectly from far-field acoustic measurements made in parametric studies. A notable exception is the work done by Schrecker [2]. Because the acoustic sources are distributed throughout relatively large regions of space, it is difficult to obtain quantitative information about the source strength at a particular point using only far-field microphone measurements. Improvement in resolution can be obtained by the use of a directional microphone. Such a technique was employed by Grosche [3] in an attempt to locate the acoustic sources in a model jet-flap configuration. Unfortunately, these devices offer adequate spatial

resolution only at high frequencies. Nevertheless, Grosche was able to show that the flap trailing edge and the turbulent flow region which is formed downstream of the edge are locations of high acoustic emission.

A more promising method for acoustic source location is the cross-correlation technique. In this method, an acoustic source quantity, such as the fluctuating pressure on a solid surface or turbulent flow fluctuations, is cross-correlated with the sound at a far-field location, making it possible to measure directly the cause-effect relationship between a source point and field point. This technique was used by Lee and Ribner [4], and more recently by Seiner [5], to locate the acoustic sources in a laboratory-scale incompressible, circular jet. In these investigations, the filtered signals of a hot-wire (film) anemometry probe and a far-field microphone were cross-correlated to yield the power spectrum of the acoustic source strength at positions in the jet. Siddon [6] measured the acoustic source strength associated with the pressure fluctuations on the surface of a small plate immersed in a turbulent jet, by cross-correlating the signal of a far-field microphone with that of a microphone embedded in the plate surface.

In the present investigation, acoustic source strength distributions are measured for a laboratory-scale jet-flap

at two far-field positions using the cross-correlation technique. The test model, which is shown in Figure 3, consists of a rigid, smooth, straight flap whose upper surface is blown tangentially by a slot-nozzle jet. A straight-flap model was chosen because it is easier to fabricate and instrument than an airfoil, but it possess similar flow characteristics which are relevant to noise generation. The acoustic source strength at a point in the turbulent flow field is obtained by cross-correlating the processed signal of a hot-film anemometry probe with that of a far-field microphone. The acoustic source strength associated with the fluctuating pressures on the flap surface is obtained by cross-correlating the processed signal of an embedded microphone with that of a far-field microphone. In addition, turbulence quantities and far-field acoustic data are measured for the jet-flap and compared with that of the slot-nozzle jet without the flap.

This dissertation is arranged into six chapters. Chapter II presents a theoretical foundation for acoustic source location using the cross-correlation technique. Chapter III gives the details of the test model and instrumentation used for data acquisition. Chapter IV contains the results of the turbulence measurements performed for the jet-flap and the slot-nozzle jet without the flap. In Chapter V the acoustic source strength

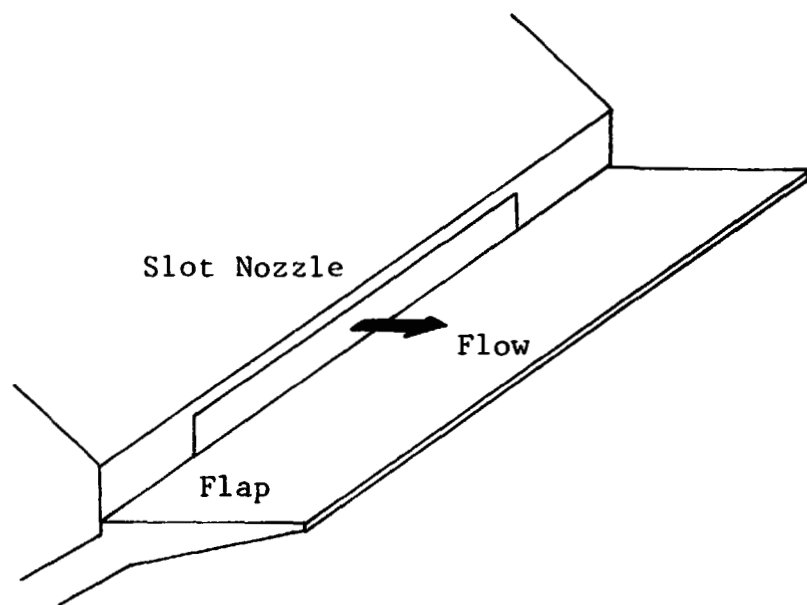


Figure 3. Jet-Flap Model.

distributions for the jet-flap are presented, in addition to far-field acoustic data for the jet with and without the flap. Finally, Chapter VI summarizes this study and presents the conclusions that can be drawn.

CHAPTER II

THEORETICAL DEVELOPMENT FOR ACOUSTIC SOURCE LOCATION

1. DERIVATION OF AN INHOMOGENEOUS WAVE EQUATION

In this chapter, a causal relationship will be established between a general turbulent flow field and its associated acoustic field. Appropriate simplifications are then made for the specific flow under investigation, and the causal relationship is developed in terms of cross-correlation functions between acoustic and flow parameters.

The conservation equations for mass and momentum for a single-phase fluid with negligible body forces are:

$$\frac{\partial \rho}{\partial t} + \frac{\partial}{\partial x_i} (\rho q_i) = 0, \quad (2-1)$$

$$\frac{\partial}{\partial t} (\rho q_i) + \frac{\partial}{\partial x_j} (\rho q_i q_j) + \frac{\partial p}{\partial x_i} - \frac{\partial \tau_{ij}}{\partial x_j} = 0 \quad (2-2)$$

where,

- x_i = Cartesian coordinates; x_1, x_2, x_3 ,
- q_i = the components of the instantaneous velocity vector,
- τ_{ij} = the components of the instantaneous viscous stress tensor,
- ρ = the instantaneous fluid density,
- p = the instantaneous fluid pressure.

Differentiating Equation (2-2) by x_i and equation (2-1) by t , then subtracting the former from the latter yields:

$$\frac{\partial^2 \rho}{\partial t^2} - \frac{\partial^2 p}{\partial x_i \partial x_i} = \frac{\partial^2}{\partial x_i \partial x_j} (\rho q_i q_j - \tau_{ij}). \quad (2-3)$$

Now by adding $c_0^{-2} \partial^2 p / \partial t^2$ to both sides of Equation (2-3), it is possible to form an inhomogeneous wave equation:

$$\begin{aligned} \frac{1}{c_0^2} \frac{\partial^2 p}{\partial t^2} - \frac{\partial^2 p}{\partial x_i \partial x_i} &= \frac{\partial^2}{\partial x_i \partial x_j} (\rho q_i q_j - \tau_{ij}) + \\ \frac{1}{c_0^2} \frac{\partial^2}{\partial t^2} (p - c_0^2 \rho), \end{aligned} \quad (2-4)$$

where c_0 is the speed of sound in the fluid at rest.

Define:

$$T_{ij}(x_i, t) = (\rho q_i q_j - \tau_{ij}),$$

$$S(x_i, t) = \frac{1}{c_0^2} (p - c_0^2 \rho),$$

and

$$F(x_i, t) = \frac{\partial^2 T_{ij}}{\partial x_i \partial x_j} + \frac{\partial^2 S}{\partial t^2}.$$

Then Equation (2-4) can be written as:

$$\frac{1}{c_0^2} \frac{\partial^2 p}{\partial t^2} - \frac{\partial^2 p}{\partial x_i \partial x_i} = F(x_i, t). \quad (2-5)$$

This non-homogeneous wave equation forms the basis of the Lighthill [7] acoustic analogy.

2. THE LIGHTHILL ANALOGY

In a region which contains a uniform medium at rest, Equation (2-5) reduces to the equation of linear acoustics. The pressure perturbations about the ambient pressure, p_0 , are governed by:

$$\frac{1}{c_0^2} \frac{\partial^2 p'}{\partial t^2} - \frac{\partial^2 p'}{\partial x_i \partial x_i} = 0 \quad (2-6)$$

where,

$$p' = (p - p_0).$$

The right-hand side of Equation (2-5) vanishes for the following reasons:

- (i) $q_i q_j$ are the products of the perturbation velocities, and are negligible compared to the linear terms. Also the effect of viscosity on the perturbed quantities is known to be negligible except over extreme distances, therefore

$$\frac{\partial^2}{\partial x_i \partial x_j} (\rho q_i q_j - \tau_{ij}) \approx 0, \quad (2-7)$$

(ii) the perturbations in density above the ambient density, ρ_0 , are related to the pressure perturbations by an isentropic equation of state:

$$p' = c_0^2 \rho' , \quad (2-8)$$

where the perturbed density, ρ' , is written as

$$\rho' = (\rho - \rho_0) .$$

Then expressing $S(x_i, t)$ in terms of the perturbation quantities, it is clear that $S(x_i, t)$ is identically zero.

If there is a turbulent flow field embedded within an ambient medium at rest, then $F(x_i, t)$ will be different from zero there. However, in the ambient fluid which surrounds the turbulent flow, $F(x_i, t)$ will again vanish according to the previous arguments, and the relevant pressure fluctuations will be acoustic. Lighthill proposed that the effect of the turbulent flow field upon the acoustic field in the ambient medium could be described by an analogy between $F(x_i, t)$ and a distribution of acoustic sources in a medium at rest. That is, one may imagine that the turbulent flow is replaced by a distribution of sources in the ambient medium which are equal to $F(x_i, t)$. Then the pressure field in the ambient

medium is described by Equation (2-5), which, in view of Lighthill's analogy, may be treated as a classical inhomogeneous wave equation.

3. GENERAL SOLUTION OF THE WAVE EQUATION

If $F(x_i, t)$ can be regarded as known, at least in principle, then a solution of Equation (2-5) exists, and has been developed rigorously by Stratton [8]. The solution for the pressure field in the ambient media is given by:

$$\begin{aligned}
 p'(x_i, t) = & \frac{1}{4\pi} \int_V \frac{1}{r} [F] dV(y_i) \\
 & + \frac{1}{4\pi} \int_A \frac{1}{r} \left[\frac{\partial p}{\partial n} \right] + \frac{1}{r^2} \frac{\partial r}{\partial n} [p] \\
 & + \frac{1}{c_0 r} \frac{\partial r}{\partial n} \left[\frac{\partial p}{\partial t} \right] dA(y_i) , \quad (2-9)
 \end{aligned}$$

where,

- V = the region occupied by the turbulent flow,
- A = the surface that bounds a region, R , which contains the ambient fluid and the embedded turbulent flow,
- x_i = coordinates of a field point where the acoustic pressure is to be calculated,
- y_i = coordinates of a source point where $F(y_i, t)$ is considered known,

n_i = a unit vector normal to and drawn outward
 from a differential area dA (y_i),
 r = the distance between the field point and
 source point, i.e., $|x_i - y_i|$.

The square brackets in the integrand denote evaluation at
 a retarded time, $t^* = (t - \tau_0)$, where $\tau_0 = r/c_0$.

Figure 4 illustrates the notation of Equation (2-9)
 for a general region R , where a Cartesian coordinate system
 has its origin at 0.

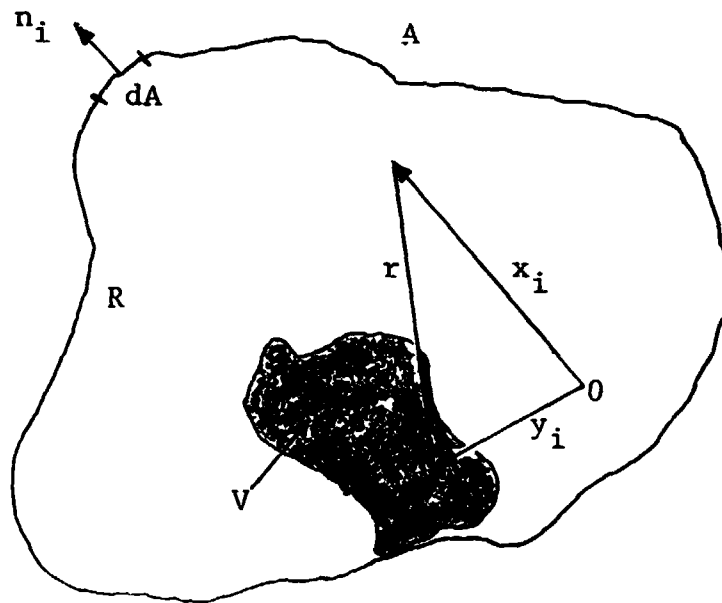


Figure 4. Notation for Eq. (2-9)

The shaded region in Figure 2-1 is the embedded turbulent flow field.

If only the sound far from the flow field is of interest, Equation (2-9) can be simplified by using vector identities and requiring that:

$$r \gg \frac{c_0}{2\pi f} ,$$

and

$$r \gg \ell ,$$

where,

f = the frequency of the pressure fluctuations,

i.e., acoustic frequency,

ℓ = characteristic length of the turbulent flow field.

The first condition insures that the pressure perturbations and velocity perturbations are in phase, and is known as the acoustic far-field condition. For the acoustic far-field, it can be shown that the space derivatives of Equation (2-9) can be replaced by time derivatives. The second condition, upon placing the origin of the coordinate system near the source region, allows the approximation $r \approx |x_i|$. The algebra involved in these simplifications is quite lengthy and will not be presented here. Complete details may be found in reference [9]. The solution for the far-field acoustic pressure is:

$$\begin{aligned}
p'(x_i, t) \approx & \frac{x_i x_j}{4\pi c_0^2 |x_i|^3} \int_V \left[\frac{\partial^2}{\partial t^2} (T_{ij} + S) \right] dV(y_i) \\
& + \frac{x_i}{4\pi c_0 |x_i|^2} \int_A \left[\frac{\partial}{\partial t} \hat{p}_i \right] dA(y_i), \quad (2-10)
\end{aligned}$$

where \hat{p}_i , the fluctuation of the resultant force which the area element dA exerts upon the fluid, is given by:

$$\hat{p}_i = n_j \left((p - p_m) \delta_{ij} - (\tau_{ij} - (\tau_{ij})_m) \right);$$

where p_m and (τ_{ij}) are the local ensemble averaged values of the pressure and the viscous stress tensor, respectively. Furthermore, Equation (2-10) assumes that any material surfaces which comprise a part of A can be treated as either rigid or anechoic. The contribution of an integration over an anechoic surface is zero.

4. APPROXIMATIONS FOR THE JFT-BLOWN FLAP

In the present analysis, the turbulent flow field and acoustic field of a laboratory-scale jet-blown flap is investigated. The jet-blown flap configuration consists of a slot nozzle air-jet with an attached straight flap which has a tapered trailing edge. Figure 5 is a schematic representation of the jet-flap configuration. Figure 6 illustrates the vector notation of Figure 4 as applied

- | | |
|--------------------------|----------------------------|
| 1. Slot Nozzle | 5. Flap Boundary Layer |
| 2. Primary Mixing Region | 6. Secondary Mixing Region |
| 3. Potential Core | 7. Fully-developed Region |
| 4. Smooth Flat Flap | |

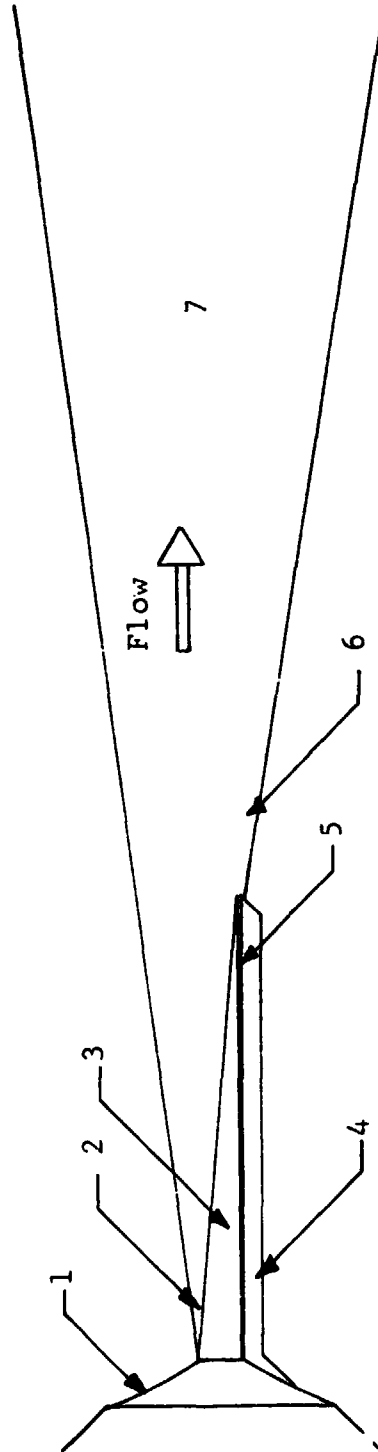


Figure 5. Jet-Flap Configuration.

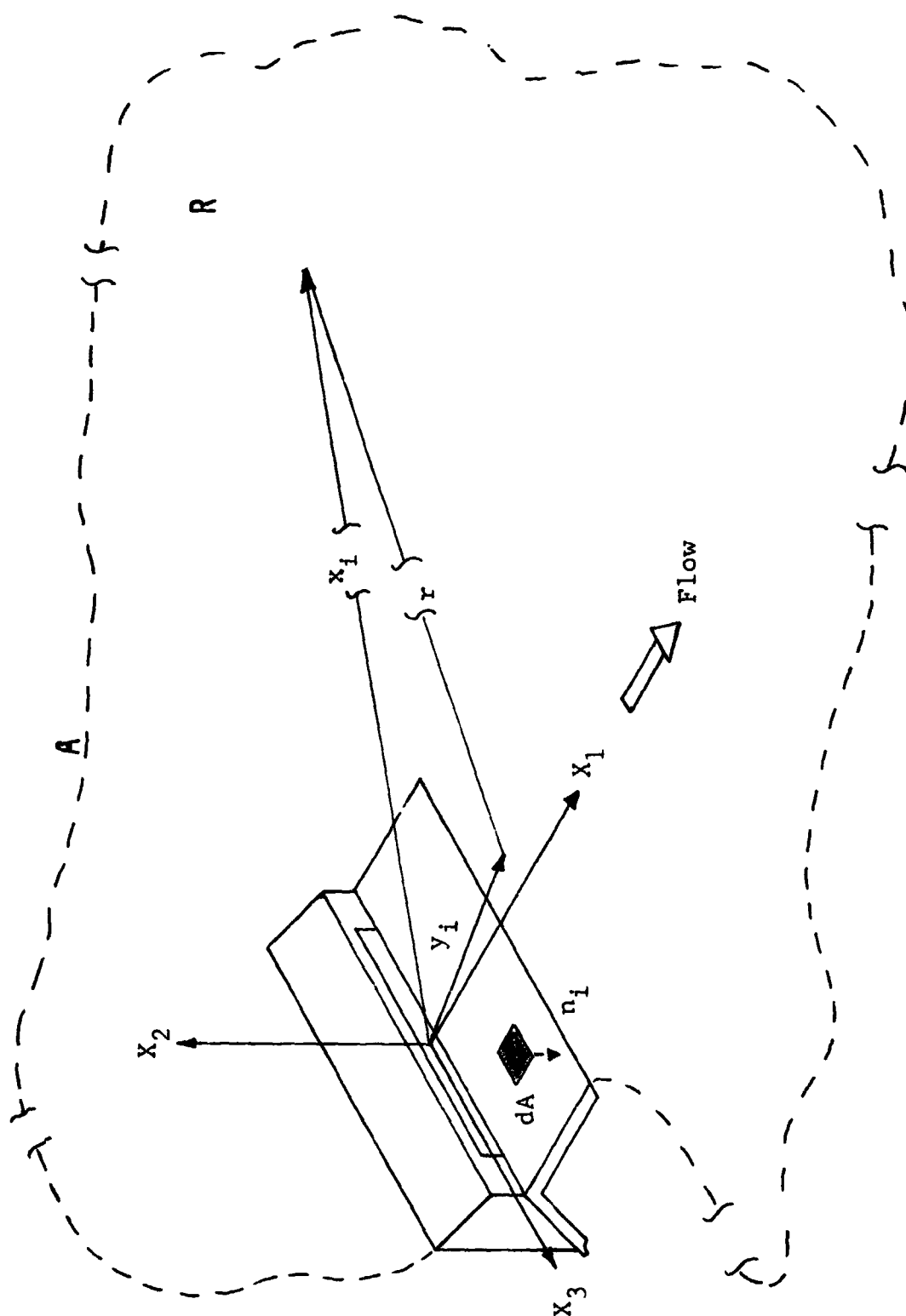


Figure 6. Vector Notation for the Jet-Flap Configuration.

to the jet-flap configuration. The origin of the coordinate system is at the exit-plane of the slot nozzle; the X_1X_3 -plane is parallel to the plane of the flap surface. The vector y_i sweeps the entire turbulent flow-field and the surface of the flap. The surfaces that enclose the region are assumed anechoic, except for the flap surface, which is rigid.

The flow field of the jet-blown flap can be divided into five regions: the potential core, the primary mixing region, the secondary mixing region, the fully-developed region, and the turbulent boundary layer on the flap surface. These regions are shown in Figure 5. In all of these regions, except perhaps in the laminar sub-region of the turbulent boundary layer, inertia effects dominate viscous effects, and it is possible to make the approximation,

$$\frac{\partial^2}{\partial t^2} T_{ij} \approx \frac{\partial^2}{\partial t^2} \rho q_i q_j \quad (2-11)$$

In the mixing region of a cold subsonic jet, the effects of heat conduction should be small. This is because the temperature differences in the flow are small, as is the thermal conductivity of air. The irreversible effects of viscosity on the flow are considered small to the extent that deviations from

$$dp = c_0^2 d\rho$$

are not large. Then:

$$p - c_0^2 \rho \approx \text{constant}$$

and,

$$\frac{\partial^2}{\partial t^2} S \approx 0 \quad (2-12)$$

Using Equations (2-11) and (2-12) Equation (2-10) is written:

$$\begin{aligned} p'(x_i, t) \approx & \frac{x_i x_j}{4\pi c_0 |x_i|^3} \int_V \left[\frac{\partial^2}{\partial t^2} \rho q_i q_j \right] dV(y_i) \\ & + \frac{x_i}{4\pi c_0 |x_i|^2} \int_A \left[\frac{\partial}{\partial t} \hat{p}_i \right] dA(y_i) \quad (2-13) \end{aligned}$$

The second order tensor, $x_i x_j$, is not a function of time or the source vector y_i , therefore $x_i x_j$ can be taken inside the volume integral and included in the argument of the derivative operator. Then by carrying out the indicated tensor operations, it can be shown that:

$$x_i x_j q_i q_j = |x_i|^2 V_x^2,$$

where V_x is the instantaneous velocity component in the x_i direction and,

$$|\mathbf{x}_i|^2 = x_1^2 + x_2^2 + x_3^2$$

Similarly for the surface integral:

$$\mathbf{x}_i \cdot \hat{\mathbf{p}}_i = |\mathbf{x}_i| |\hat{\mathbf{p}}_i| \cos \theta,$$

where θ is the angle between \mathbf{n}_i and \mathbf{x}_i . Furthermore, Curle [10] has reported that the mean square value of the pressure fluctuations in a turbulent boundary layer are at least 30 times larger than the mean square value of the skin-friction fluctuations. Therefore, $|\hat{\mathbf{p}}_i|$ can be approximated by the fluctuations of the hydrodynamic pressure. i.e.,

$$|\hat{\mathbf{p}}_i| \approx (p - p_m),$$

and

$$\frac{\partial}{\partial t} |\hat{\mathbf{p}}_i| = \frac{\partial}{\partial t} p$$

Equation (2-13) then reads

$$\begin{aligned} p'(\mathbf{x}_i, t) \approx & (4\pi\rho_0\gamma |\mathbf{x}_i|)^{-1} \int_V \left[\frac{\partial^2}{\partial t^2} (\rho_0 \rho V^2_{\mathbf{x}}) \right] dV(\mathbf{y}_i) \\ & + \cos \theta (4\pi c_0 |\mathbf{x}_i|)^{-1} \int_A \left[\frac{\partial p}{\partial t} \right] dA(\mathbf{y}_i), \quad (2-14) \end{aligned}$$

where the ideal gas relationship,

$$c_0^2 = \frac{\gamma p_0}{\rho_0}$$

is used in the first term of Equation (2-14). For air, γ , the ratio of the specific heats, equals 1.4. Equation (2-14) is equivalent to an equation developed by Curle in reference [11].

5. CORRELATION ANALYSIS

The turbulence quantities of a jet with steady plenum conditions are, in general, statistically stationary, as is the sound produced by the jet. The autocorrelation function of the far-field sound is written as:

$$R_{p'p'}(x_i, \tau') = \overline{p'(x_i, t) p'(x_i, t + \tau')}, \quad (2-15)$$

where τ' is an arbitrary time increment and the overbar denotes a time average. It should be noted that $R_{p'p'}(x_i, \tau')$ is not a function of t , but depends only on x_i and τ' . Multiplying both sides of Equation (2-14) by $p'(x_i, t + \tau')$ and averaging yields:

$$R_{p'p'}(x_i, \tau') \approx (4\pi p_0 |x_i| \gamma)^{-1} \quad (2-16)$$

$$\begin{aligned} & * p'(x_i, t + \tau') \int_V \left[\frac{\partial^2 M_x^2}{\partial t^2} \right] dV(y_i) \\ & + \cos \theta (4\pi c_0 |x_i|)^{-1} p'(x_i, t + \tau') \int_A \left[\frac{\partial}{\partial t} p \right] dA \end{aligned}$$

where,

$$M_x^2 = \rho_0 c V_x^2.$$

Since p' is not a function of y_i it may be placed inside the integrals. The averaging process is assumed to commute with the integration process, so that:

$$\begin{aligned} R_{p'p'}(x_i, \tau') &\approx (4\pi\rho_0 |x_i| \gamma)^{-1} \\ &\int_V \left[\frac{\partial^2}{\partial t^2} M_x^2 \right] p'(x_i, t + \tau') dV(y_i) \\ &+ \cos \theta (4\pi c_0 |x_i|)^{-1} \int_A \left[\frac{\partial p}{\partial t} \right] p'(x_i, t + \tau') dA(y_i). \end{aligned} \quad (2-17)$$

It is convenient at this time to introduce a different notation scheme for retarded-time evaluation. The square brackets, which indicate retarded-time evaluation of the integrands, will be replaced by conventional functional notation, i.e.,

$$\left[\frac{\partial^2}{\partial t^2} M_x^2 \right] = \frac{\partial^2}{\partial t^2} M_x^2(t^*),$$

where, as before, $t^* = t - \tau_0$. Using this notation, the integrands of Equation (2-17) can be written as cross-correlation functions between the far-field sound and flow parameters:

$$\begin{aligned}
R_{p'p'}(x_i, \tau') \approx & \\
(4\pi\gamma\rho_0|x_i|)^{-1} \int_V R_{\ddot{M}_x^2 p'}(\tau) dV(y_i) & \\
+ \cos\theta (4\pi c_0|x_i|)^{-1} \int_A R_{\dot{p} p'}(\tau) dA(y_i), & \quad (2-18)
\end{aligned}$$

where

$$\begin{aligned}
R_{\ddot{M}_x p'}(\tau) &= \overline{\frac{\partial^2}{\partial t^2} M_x^2(t^*) p'(t^* + \tau)}, \\
R_{\dot{p} p'}(\tau) &= \overline{\frac{\partial}{\partial t} p(t^*) p'(t^* + \tau)},
\end{aligned}$$

and

$$\tau = \tau_0 + \tau'.$$

The mean-square value of the far-field sound is equal to its autocorrelation function evaluated at $\tau' = 0$, i.e.,

$$\overline{p'^2(x_i, t)} = R_{p'p'}(x_i, \tau') \Big|_{\tau' = 0}.$$

Then,

$$\overline{p'^2(x_i, t)} \approx (4\pi p_0 |x_i|)^{-1} \int_V \ddot{R}_{M_x p'}(\tau_0) dV(y_i) \\ + \cos\theta (4\pi c_0 |x_i|)^{-1} \int_A R_{p p'}(\tau_0) dA(y_i) \quad (2-19)$$

The volume integrand, $\ddot{R}_{M_x p'}(\tau_0)$, represents the contribution to the mean-square value of the far-field sound produced by a differential volume of turbulence. Similarly, $R_{p p'}(\tau_0)$ is the contribution from a differential area on the flap surface. The measurement of these integrands is the primary purpose of this investigation.

6. MODIFICATIONS FOR MEASUREMENT

The measurement of $R_{p p'}(\tau_0)$ can be accomplished directly by cross-correlating the signal from a far-field microphone with the time derivative of the signal from a microphone embedded in the flap surface. The time derivative of the embedded microphone signal can be obtained using an analog differentiation circuit. The measurement of $\ddot{R}_{M_x p'}(\tau_0)$ can be obtained indirectly by cross-correlating a twice-differentiated hot-film anemometer signal with the signal from a far-field microphone. Recall that:

$$M_x^2 = \rho_0 \rho V_x^2 = (\rho_0 V_x) (\rho V_x) .$$

The output signal of a hot-film anemometer probe is a function of the momentum component normal to the probe axis (See Chapter 3 for probe detail.) Therefore it would be convenient to be able to express M_x^2 in terms of the quantity (ρV_x) , so that direct measurement with a suitably positioned probe would be possible. For this reason it will be assumed that:

$$M_x^2 \approx (\rho V_x)^2 ,$$

or

$$M_x \approx (\rho V_x) .$$

The instantaneous momentum, M_x , can be decomposed into a mean value and a deviation from the mean value, i.e.,

$$M_x = \bar{M}_x + m_x$$

where

$$\bar{M}_x = \text{the mean value of } M_x ,$$

and

$$m_x = \text{the deviation of } M_x \text{ from } \bar{M}_x .$$

Then:

$$\frac{\partial^2}{\partial t^2} M_x^2 = 2\bar{M}_x \frac{\partial^2}{\partial t^2} m_x + \frac{\partial^2}{\partial t^2} m_x^2 .$$

and:

$$\ddot{R}_{m_x^2 p'}(\tau) = 2\bar{M}_x \ddot{R}_{m_x p'}(\tau) + \ddot{R}_{m^2 p'}(\tau) \quad (2-20)$$

where:

$$\ddot{R}_{m_x p'}(\tau) = \overline{\frac{\partial^2}{\partial t^2} m_x^2(t^*) p'(t^* + \tau)},$$

$$\ddot{R}_{m^2 p'}(\tau) = \overline{\frac{\partial^2}{\partial t^2} m_x^2(t^*) p'(t^* + \tau)}.$$

Placing these results into Equation (2-19) yields:

$$\begin{aligned} \overline{p'^2(x_i, t)} &\approx (4\pi\rho_0 |x_i| \gamma)^{-1} \int_V \left[2\bar{M}_x \ddot{R}_{mp'}(\tau_0) + \right. \\ &\quad \left. \ddot{R}_{m^2 p'}(\tau_0) \right] dV(y_i) \\ &\quad + \cos\theta (4\pi c_0 x_i)^{-1} \int_A \ddot{R}_{pp'}(\tau_0) dA(y_i) \quad (2-21) \end{aligned}$$

The first term in the volume integrand is known as shear noise because it is thought to represent the noise generated by the interaction of the turbulence with the mean flow. This quantity is obtained by measuring m' with a hot-film anemometer probe at y_i , differentiating the anemometer signal twice with an analog device, and cross correlating the differentiator output with the output

of a far-field microphone at x_i . The second term in the volume integrand is the "self noise" contribution; so called because it is thought to represent the noise produced by the interaction of the turbulence with itself. This term is obtained in a similar manner as the shear noise term, except that the anemometer signal is squared in an analog multiplier before being differentiated. A schematic of the measurement technique is shown in Figure 7.

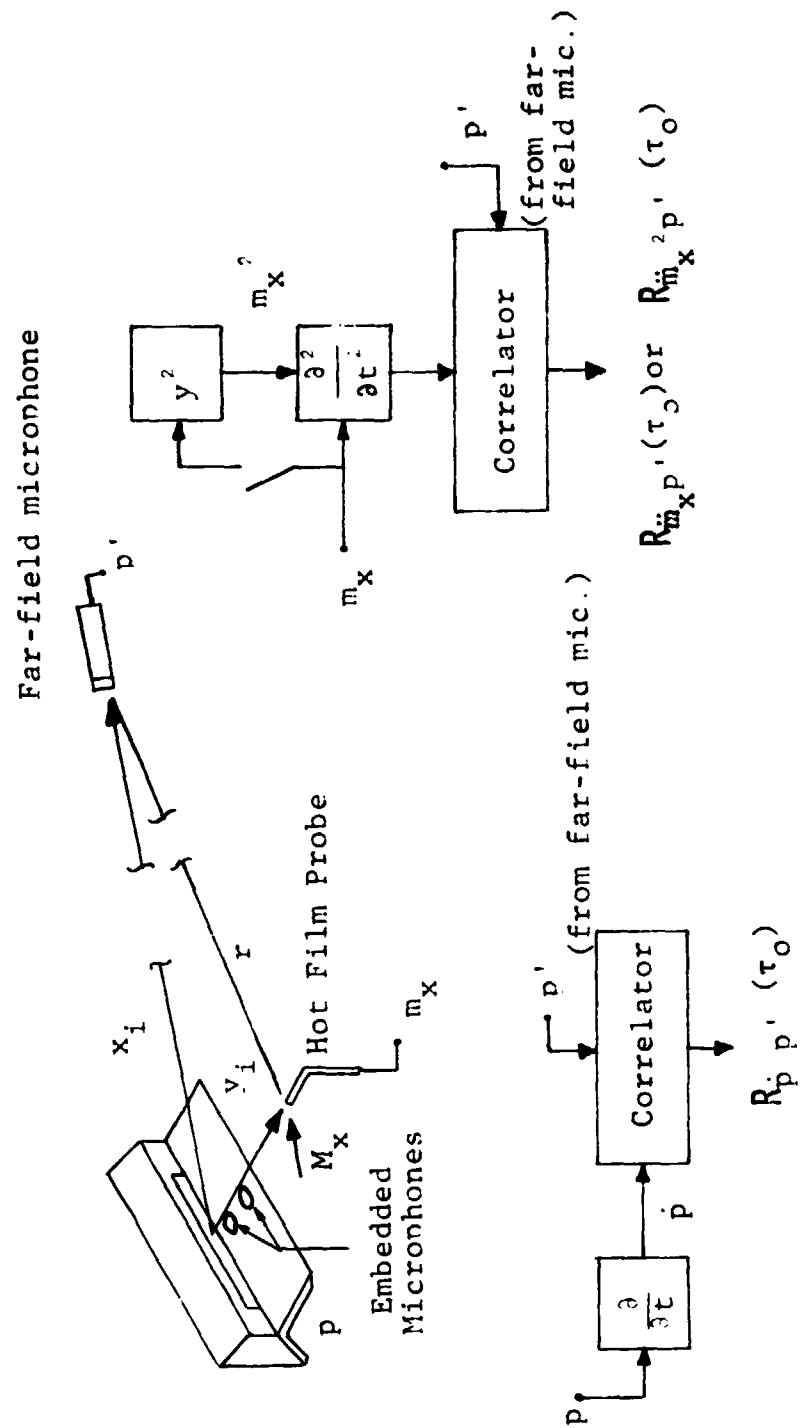


Figure 7. Acoustic Source Measurement Scheme

CHAPTER III

EXPERIMENTAL EQUIPMENT AND DATA ACQUISITION

1. THE JET FACILITY

The experiments were conducted in an anechoic room located at the NASA Lewis Research Center in Cleveland, Ohio. The working dimensions for the anechoic room are 50' x 44' x 18', and the room's cut-off frequency is 350 Hz. High-pressure air is supplied to the anechoic chamber from a central supply station, which supplies air to other laboratories at Lewis Center. The high-pressure air enters the anechoic room via a 4 inch diameter supply pipe. Connected to the supply pipe is a 10 inch diameter stilling chamber, which is 44 inches in length and mated to the slot nozzle by a transition piece, as shown in Figure 8. The air within the stilling chamber is expanded isentropically by the test nozzle to the ambient atmosphere in the anechoic room. About midway in the stilling chamber there are two screens used to damp large scale flow disturbances and stop the passage of any large particles which might be suspended in the flow.

In the stilling chamber, near the transition piece, there are two taps for measuring the static pressure and temperature. The stilling-chamber pressure is controlled by means of a remotely operated Globe valve which regulates

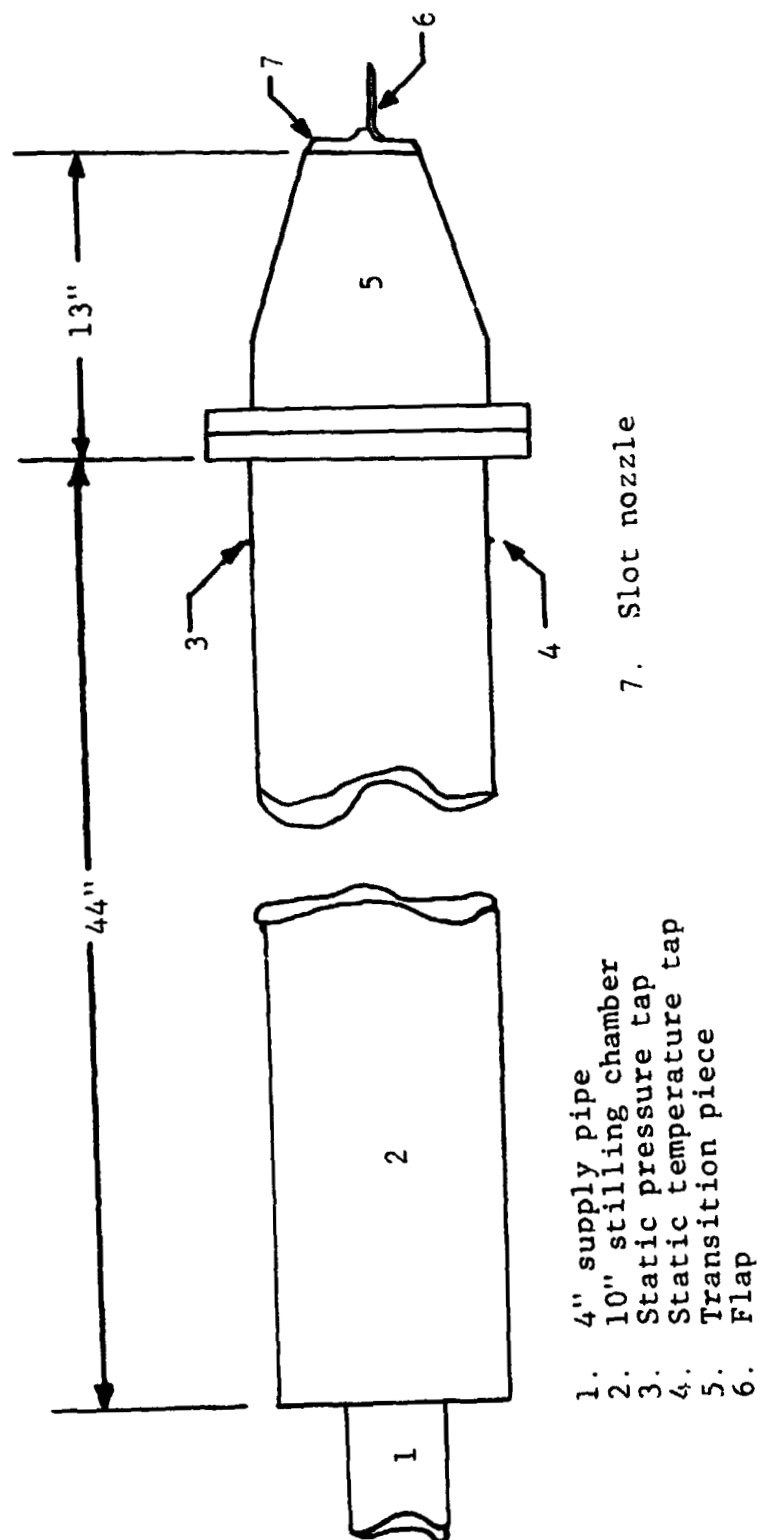


Figure 8. Test Hardware.

the flow-rate from the central high-pressure supply. Two electrical pressure transducers were used to measure the stilling chamber pressure and the ambient pressure in the anechoic room. The signal from the ambient pressure transducer was divided by that of the stilling chamber transducer by an analog ratio circuit, processed by analog-to-digital converter, and displayed at the flow controller's console as a 3 digit decimal fraction. The pressure ratio indicates directly the isentropic Mach number at the nozzle exit plane. The pressure ratio was extremely stable during all of the tests, indicating the lack of large-scale disturbances or other unsteady phenomena within the stilling chamber. The stilling chamber temperature was, in general, within 10 degrees Fahrenheit of the anechoic room ambient temperature.

The test model consists of a aluminum slot nozzle with an attached aluminum straight flap that contains two microphones mounted flush with the flap surface. The slot-nozzle height is .3 inches, and its span is 3.9 inches, thus making the aspect ratio of the slot nozzle equal to 13. The flap is 3 inches long and has a span of 10 inches. The non-dimensional length of the flap, based on the slot-nozzle height is 10. The test model is shown in Figure 9. The flap with the embedded microphones was only used for obtaining the data for the cross correlation of

1. Embedded Microphone 1
2. Embedded Microphone 2

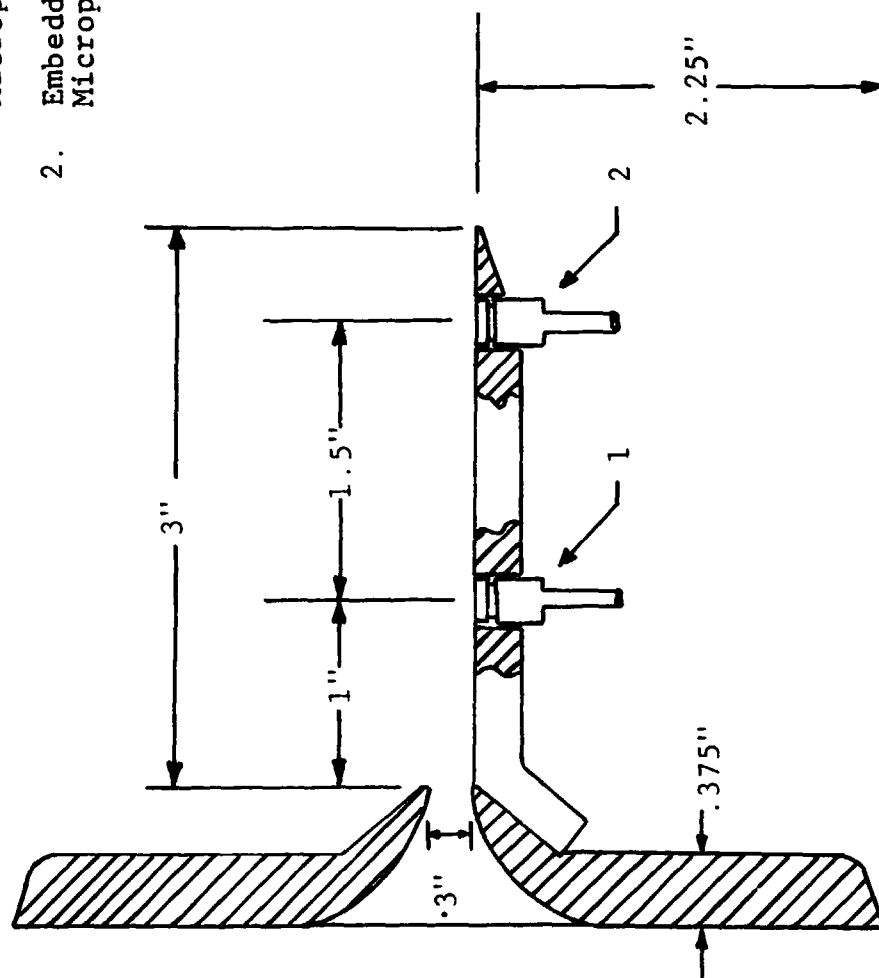


Figure 9. The Test Model.

the surface pressure and the far-field sound. For all other tests, this flap was replaced with an unperforated smooth flap in order to save the embedded microphones from needless exposure to the turbulent flow.

2. THE TEST SET-UP

The test model, transition piece, and stilling chamber are suspended 9 feet above the floor of the anechoic room. A quarter-circle of stand-mounted microphones is placed at a radius of 12.666 feet from the nozzle exit plane, as shown schematically in Figure 10. The 45-degree microphone was used for the cross-correlation experiments, and with the hot film probe removed from the flow, the entire quarter circle was used for acoustic measurements. Both the free-field and embedded microphones are manufactured by the B & K Company and are $\frac{1}{2}$ " in diameter. Mounting of the embedded microphones was facilitated by flexible adapters supplied by B & K. The transition piece and test model could be rotated, so that acoustic and flow data could be obtained for the X_1X_2 -plane and the X_1X_3 -plane, without moving any of the far-field microphones.

The hot-film probes were positioned in the flow by a remotely-operated 3-axis traversing mechanism. The traversing mechanism was mounted beneath the stilling chamber on 4 massive steel columns which were anchored to the

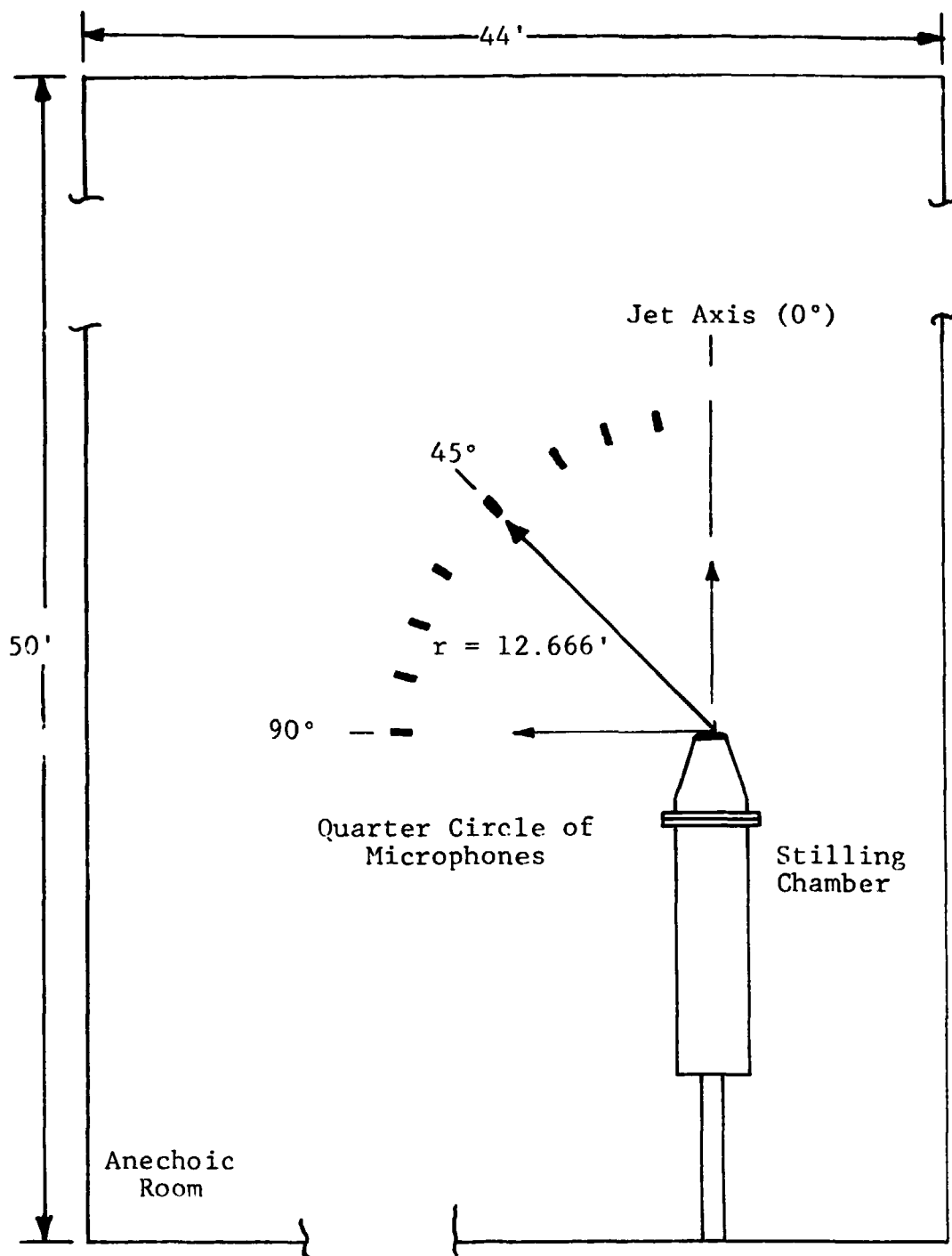


Figure 10. Overhead View of Test Set-Up.

concrete sub-floor of the anechoic room. The traversing mechanism is shown in Figure 11. This photograph was made during the installation of the traversing mechanism; the test model was not mounted. The traversing system consists of two moving platforms, A and B, a rigid boom, C, and a mounting tube assembly, D, which moves vertically at the end of the rigid boom. Platform A moves parallel to the jet axis along rails and a threaded shaft which are attached to the supporting frame, E. The rigid boom is fixed to platform B. The probe holder, F, is held by the mounting-tube assembly, which moves vertically along its threaded shaft as A and B move in the horizontal plane. The threaded shaft is the right-hand shaft in the mounting-tube assembly. Figure 12 shows the probe-mounting configuration and directions of traverse.

Three remotely controlled electric drive-motors move the two platforms and probe-mounting assembly. The position of A establishes the X_1 -coordinate of the probe, and the position of B and D establishes the X_2 and X_3 -coordinate, respectively. The positions of A, B, and D are measured by 3 absolute-displacement digital encoders which are connected to the threaded drive-shafts of A, B, and D by precision gears. The encoders measure the displacement of A, B, and D along their threaded shafts relative to a fixed origin. The outputs of the encoders are digital

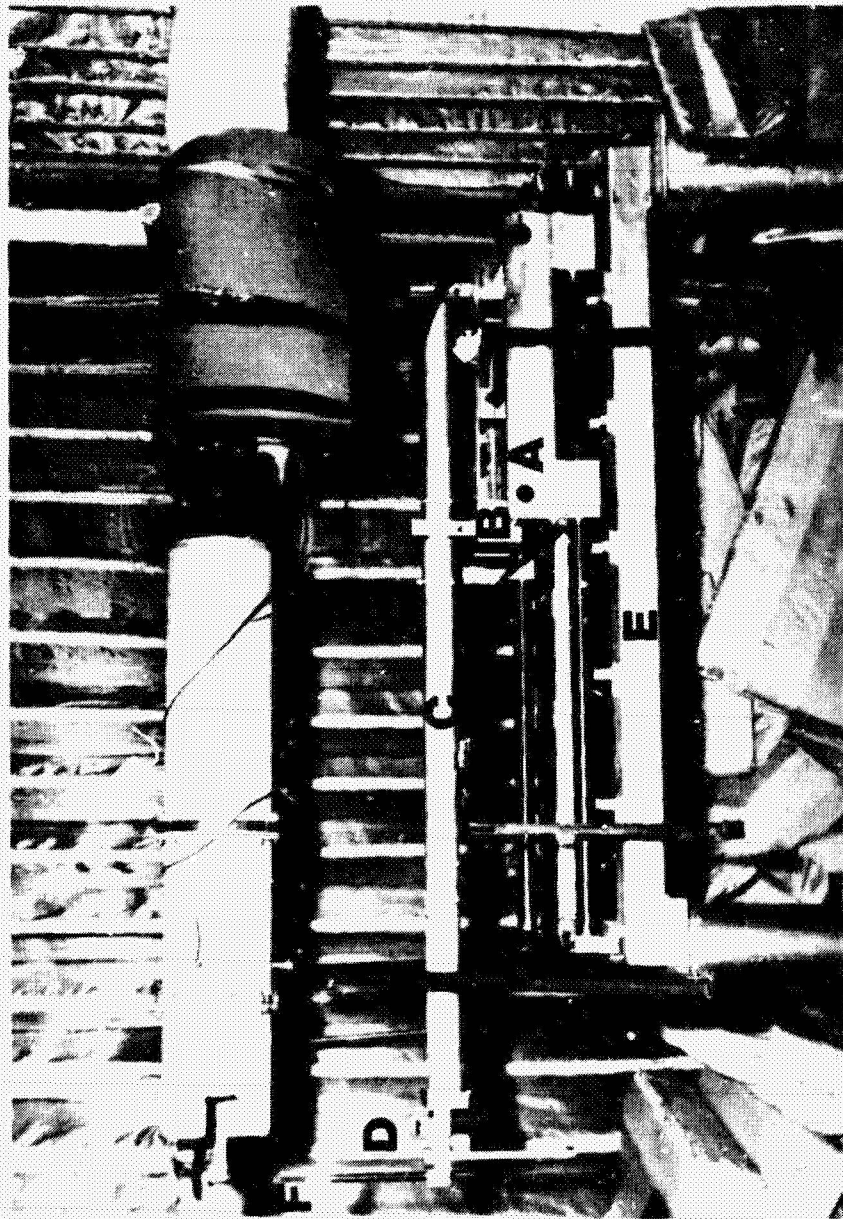
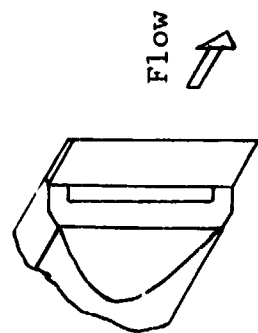


Figure 11. Traversing Mechanism.

ORIGINAL PAGE IS
OF POOR QUALITY



1. Hot-film probe
2. Probe holder
3. Mounting-tube assembly

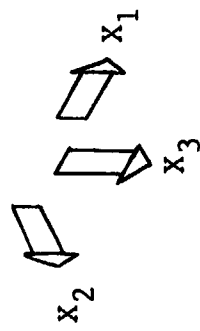
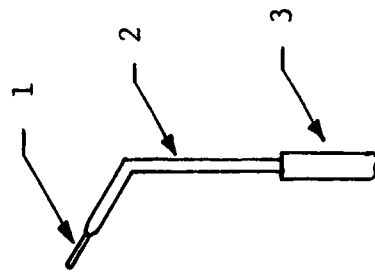


Figure 12. Probe-Mounting Configuration.

signals which were processed and displayed remotely at control-boxes located in the anechoic-chamber control room. There is a control-box for each axis, and movement along an axis is accomplished by entering the desired coordinate via a thumbwheel-switch which is located directly above the position display on the front of the control-box. The axis drive-motor is then energized by the control-box logic until the axis position corresponds to the thumbwheel-switch setting. There is also a non-automatic option which allows axis-movement under manual control. The traversing system, which was custom-built by the L. C. Smith Company, Cleveland, Ohio, was judged accurate to within ± 1 millimeter. An actual test set-up is shown in Figure 13. The dust covers on the microphones are removed during data acquisition.

3. DATA ACQUISITION FOR CROSS-CORRELATION ANALYSIS

The measurement of M_x , which was needed for the off-line evaluation of $R_{M_x p}(\tau_0)$, was accomplished using a constant temperature hot-film anemometry probe whose sensor filament is inclined at a 45-degree angle. The axis of the sensor is normal to M_x , and, since the heat transferred from the sensor element is almost totally determined by the momentum normal to its axis, M_x can be measured directly. Figure 14 shows an exaggerated view of the DISA 55R02 probe used

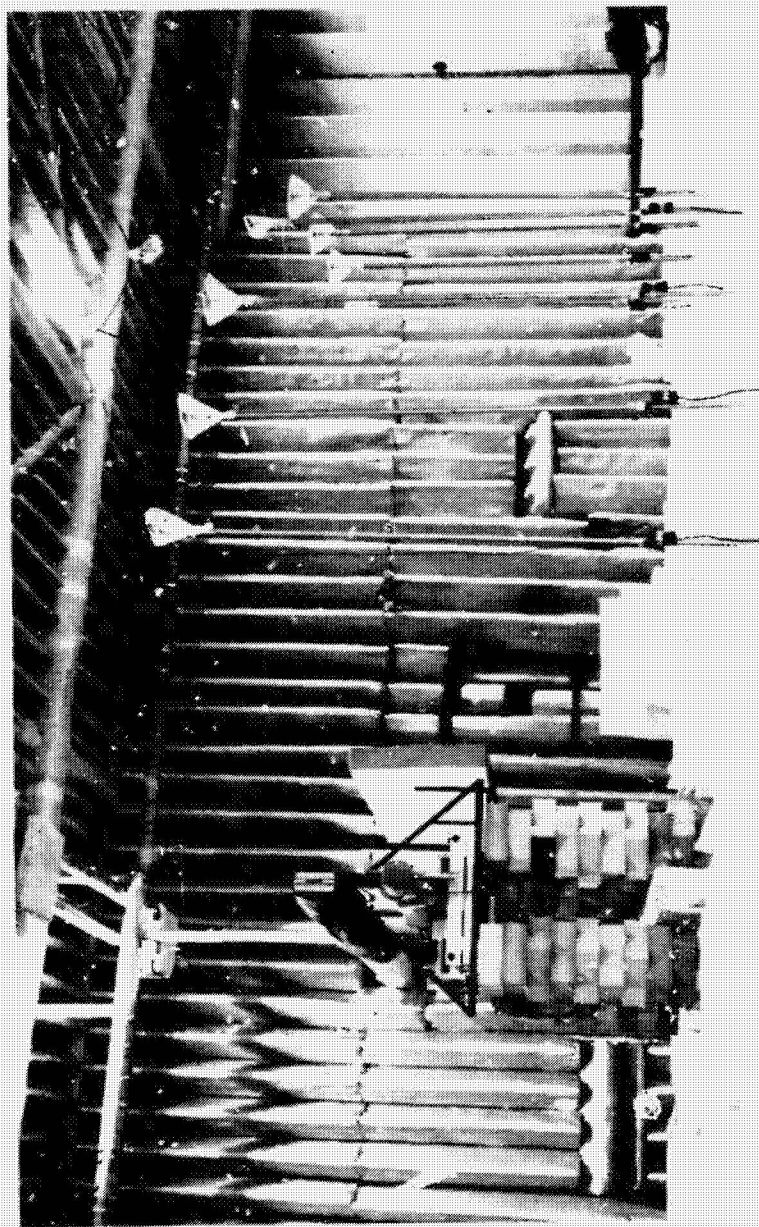


Figure 13. Test Set-up in Anechoic Chamber.

ORIGINAL PAGE IS
OF POOR QUALITY

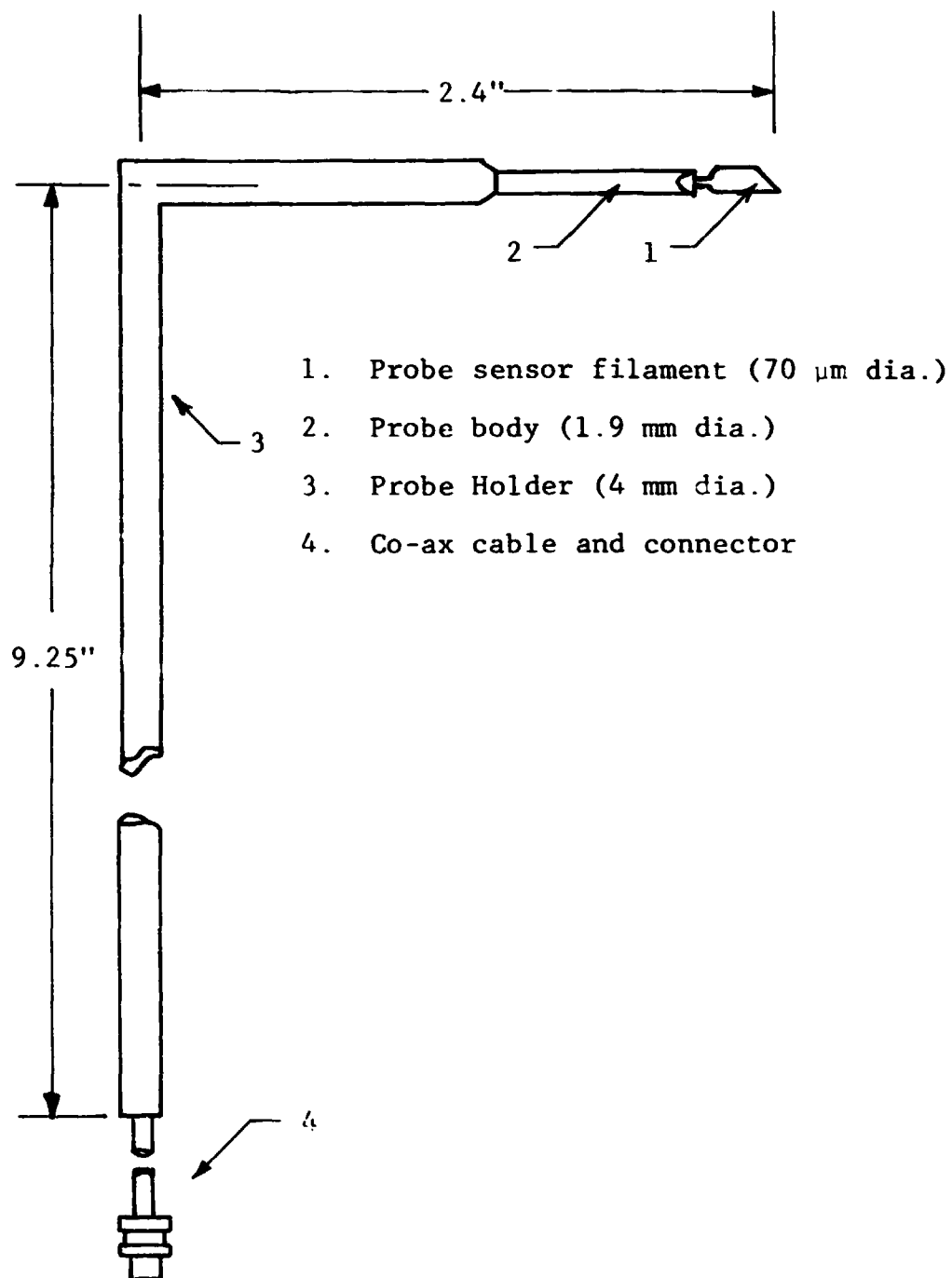


Figure 14. DISA 55R02 Probe and Probe Holder.

for measuring M_x . The probe sensor filament is maintained at a constant temperature by a DISA CONSTANT TEMPERATURE ANEMOMETER (CTA), Model 55D01. The CTA electronically senses the heat transfer from the sensor element and provides an output voltage which is a function of M_x . The output of the CTA is not a linear function of M_x , so it is electronically processed by a DISA 55D10 Linearizer, whose output voltage, e_{M_x} , is directly proportional to M_x . That is:

$$M_x = \beta e_{M_x}$$

where,

$$\beta = \frac{(M_x)_{\text{ref}}}{(e_{M_x})_{\text{ref}}},$$

$$(M_x)_{\text{ref}} = \text{a known reference mass flux,}$$

$$(e_{M_x})_{\text{ref}} = \text{the value of } e_{M_x} \text{ with the probe inserted in the reference flow.}$$

A detailed discussion on the measurement of M_x by use of a hot-film probe is presented in Appendix A. A reference mass flux is available at the slot-nozzle exit-plane, where flow conditions can be calculated using isentropic flow theory. A typical linearization curve is shown in Figure 15A, which is a graph of the linearizer output voltage for a given mass flux. Figure 15B is a graph of

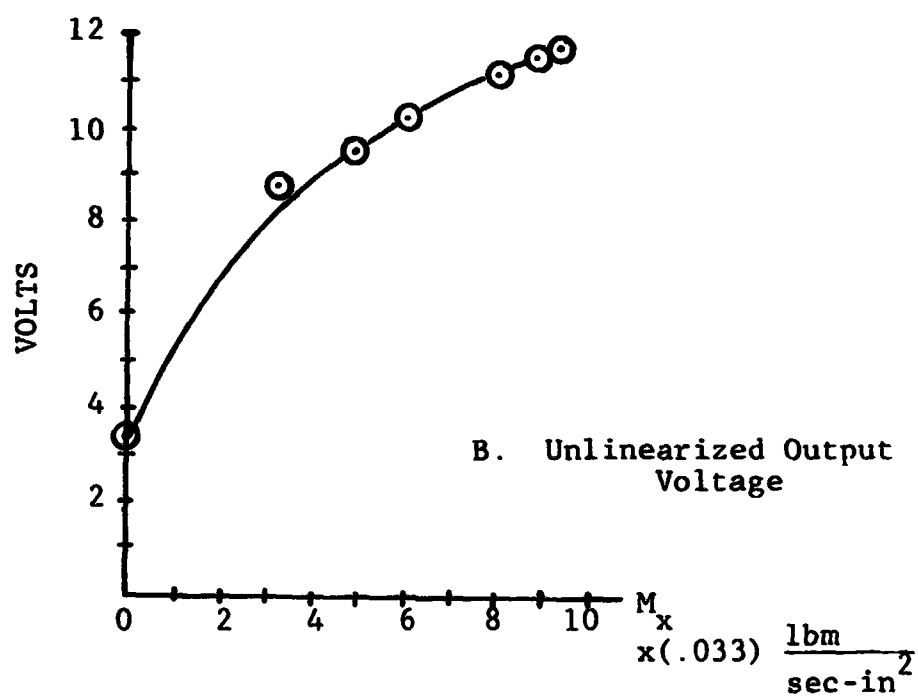
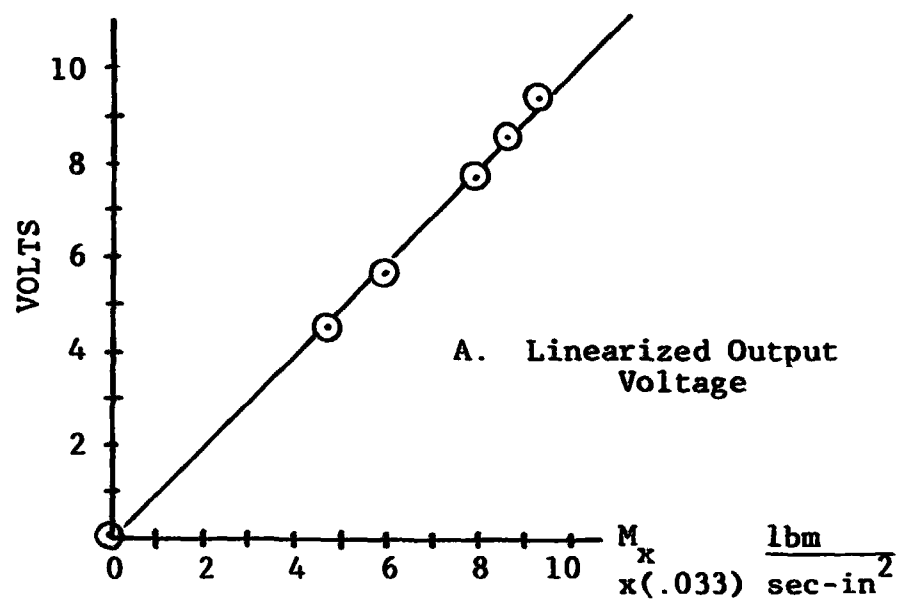


Figure 15. Comparison of Linearized and Unlinearized Probe Calibration Curves.

the corresponding unlinearized voltage at the CTA output.

Since the cross-correlation analysis was an off-line operation, all requisite data had to be recorded on magnetic tape. A Sangamo Sabre III, FM, 14-Channel recorder was used for this purpose. The Sabre III recorder was operated at a speed of 60 inches per second in the wide-band mode. In this configuration the Sabre III has a bandwidth of 40 kHz. Only fluctuating quantities were recorded, therefore all of the CTA signals that were to be recorded were AC-coupled (DC-component removed) to the tape deck with B & K general purpose amplifiers. Use of the amplifiers also allowed the amplitudes of the signals to be adjusted so that the full dynamic range of the tape recorder could be utilized.

A schematic representation of signal processing and recording of turbulence and acoustic data is shown in Figure 16. Note that physical quantities appear in the schematic instead of their voltage analogs in order to avoid confusion. The unlinearized output of the CTA was recorded on channel 1 of the tape deck. The output voltage of the linearizer was monitored with a B & K digital voltmeter, by which \bar{M}_x was measured, and then recorded on channel 3 after the DC-component had been removed by amplifier 3. The output of amplifier 3 was connected to

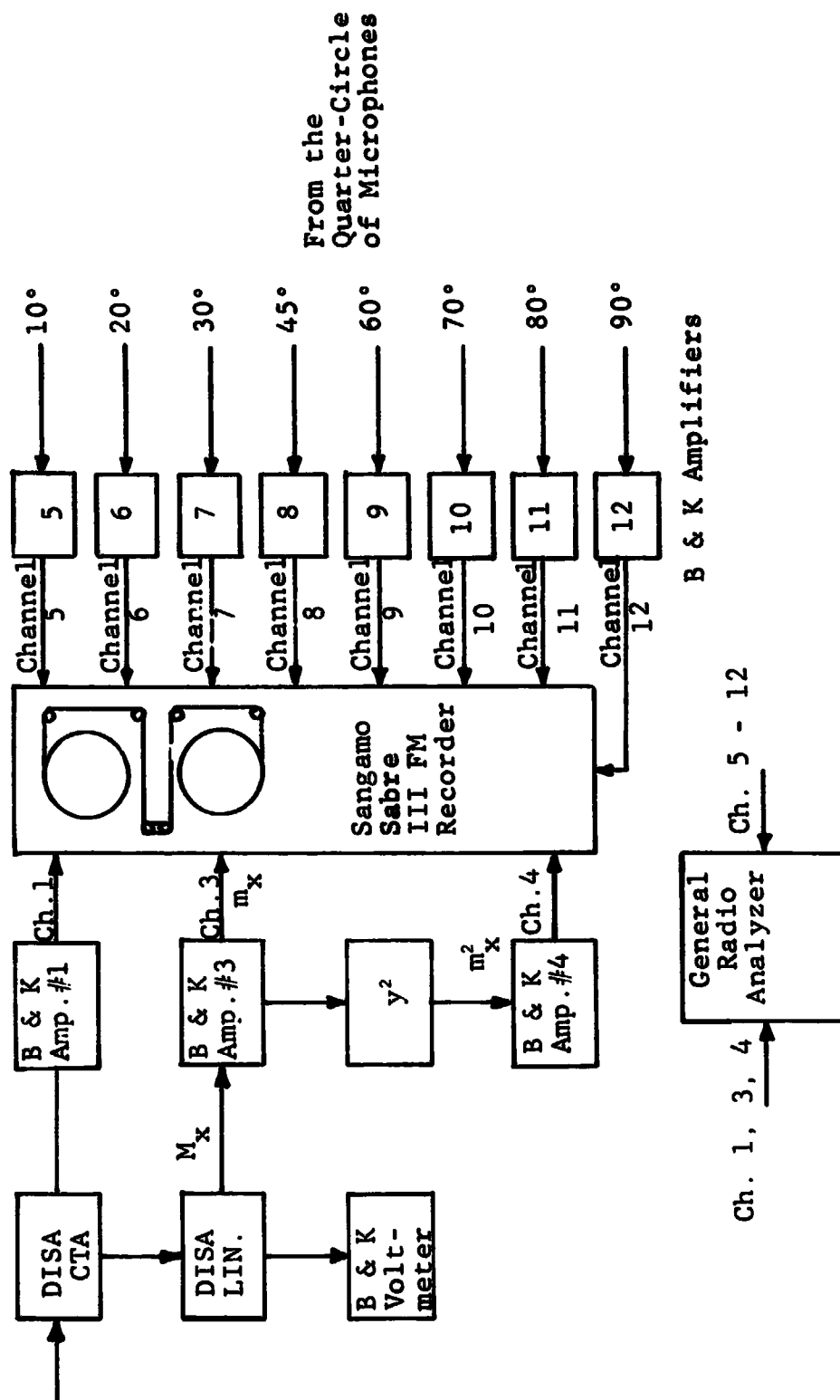


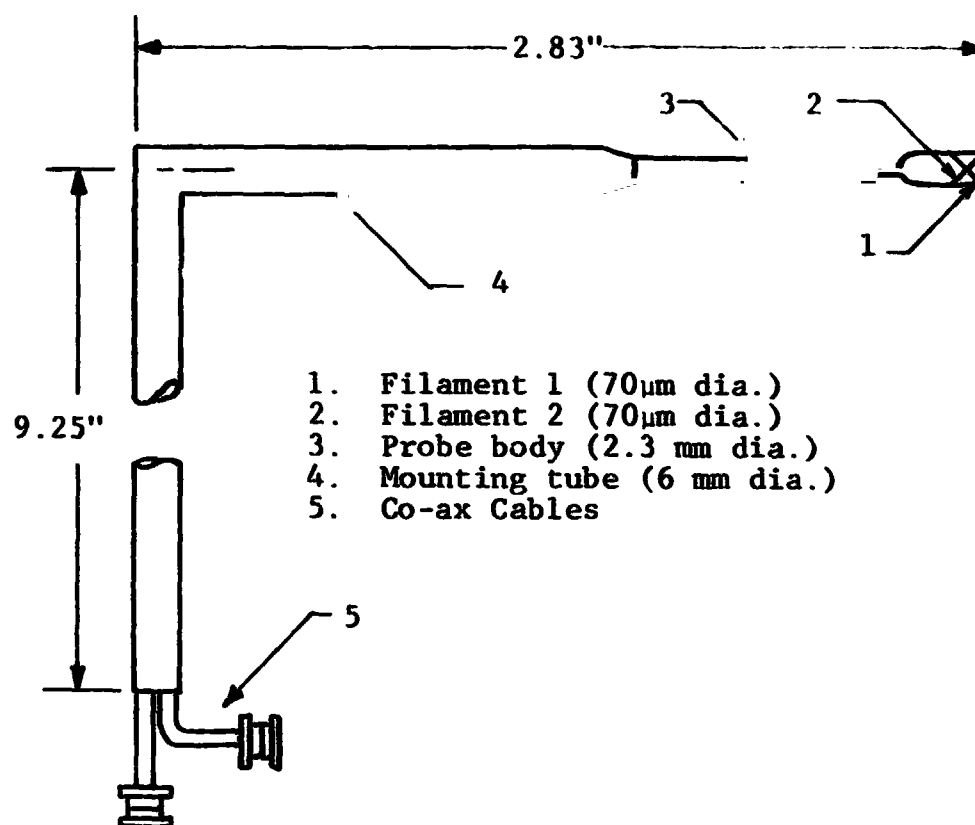
Figure 16. Data Acquisition for the Cross-Correlation Analysis.

an analog squaring circuit whose output was recorded on Channel 4. Amplifier 4 was used solely to optimize the amplitude of the squared signal for recording. Channels 5 through 12 were used to record the acoustic data from the quarter circle of microphones. Channels 3, 4 and 8 are used off-line for the cross-correlation analysis. The outputs of the amplifiers were connected to a General Radio 1/3 octave analyzer so that on-line spectra of all channels could be obtained.

Data acquisition for the off-line evaluation of $R_{p'p'}(\tau_0)$ was similar to that shown in Figure 16, except that the fluctuating surface pressure, p_1 and p_2 from the embedded microphones were recorded on Channels 1 and 3 respectively. No hot-film probe was present in the flow during this test. As before, an on-line 1/3-octave analysis is carried out on all data channels.

4. DATA ACQUISITION FOR FLUID-DYNAMIC MEASUREMENTS

The fluid-dynamic measurements, which are discussed in Chapter IV, were acquired on-line using a dual-sensor hot-film probe, DISA 55R51. The probe consists of two sensor filaments which are inclined at 45 degrees and 135 degrees, so that when viewed in a plane parallel to the probe-axis plane, an "X" is seen. The dual sensor probe is shown in Figure 17A. Each of the sensor filaments is connected to its own CTA and linearizer, thus forming two separate



A. Probe and Holder

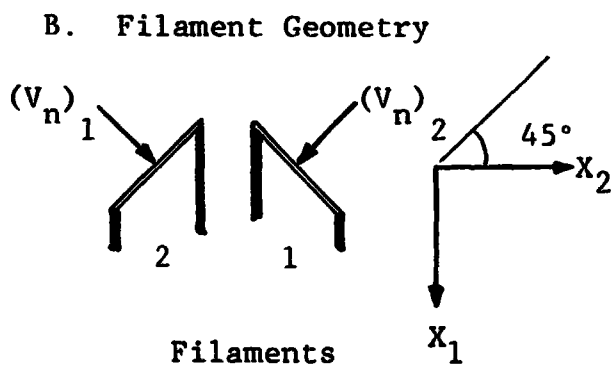


Figure 17. DISA 55R51 Probe and Associated Geometry

channels as shown in Figure 18, which is the data acquisition schematic for the fluid-dynamic measurements. Each channel is linearized independently using the same value of β . Linearization is done with respect to velocity, so that

$$\beta = \frac{\left(\frac{V_n}{c^*}\right)_{\text{ref}}}{(e_n)_{\text{ref}}} ,$$

where

- c^* = the speed of sound at the nozzle exit plane,
- V_n = the velocity normal to the sensor filament
which is known from a reference flow,
- $(e_n)_{\text{ref}}$ = the linearizer output voltage when its
associated probe sensor filament is in the
reference flow.

The non-dimensional axial and lateral velocities, V_1/c^* and V_2/c^* , are proportional to the sum and difference of the two linearizer signals, respectively. This may be demonstrated by letting $(V_n/c^*)_1$ and $(V_n/c^*)_2$ be the velocity components normal to sensor filaments 1 and 2, respectively. Then in terms of the axial and transverse velocities, V_1/c^* , V_2/c^* , $(V_n/c^*)_1$ and $(V_n/c^*)_2$ can be written as:

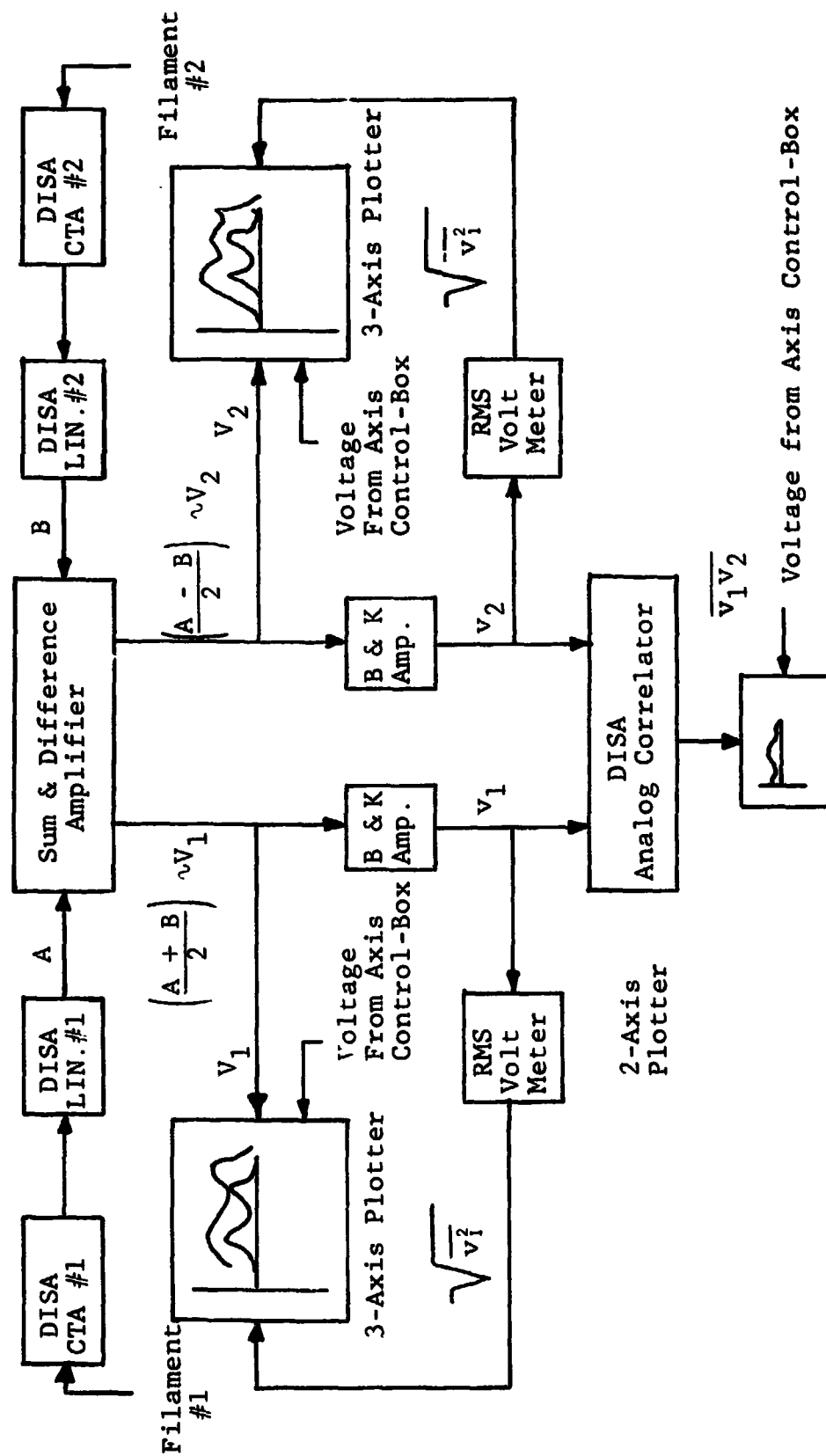


Figure 18. Data Acquisition for the Dual Sensor Probe Fluid Dynamic Measurements.

$$\left(\frac{V_n}{c^*}\right)_1 = \cos 45^\circ \left[\frac{V_1}{c^*} + \frac{V_2}{c^*} \right]$$

$$\left(\frac{V_n}{c^*}\right)_2 = \cos 45^\circ \left[\frac{V_1}{c^*} - \frac{V_2}{c^*} \right] .$$

See Figure 17B for geometry.

Then:

$$\left(\frac{V_n}{c^*}\right)_1 + \left(\frac{V_n}{c^*}\right)_2 = 2 \cos 45^\circ \frac{V_1}{c^*} ,$$

$$\left(\frac{V_n}{c^*}\right)_1 - \left(\frac{V_n}{c^*}\right)_2 = 2 \cos 45^\circ \frac{V_2}{c^*} .$$

In terms of the linearizer voltages these equations read:

$$\beta \left[(e_n)_1 + (e_n)_2 \right] = 2 \cos 45^\circ \left(\frac{V_1}{c^*} \right) ,$$

$$\beta \left[(e_n)_1 - (e_n)_2 \right] = 2 \cos 45^\circ \left(\frac{V_2}{c^*} \right) ,$$

where,

$(e_n)_1$ = the output voltage from linearizer 1,

$(e_n)_2$ = the output voltage from linearizer 2.

The sum and difference of $(e_n)_1$ and $(e_n)_2$ were calculated by analog operational amplifiers manufactured by the Zeltex Corporation.

The traversing mechanism moves the dual-sensor probe across the jet at various axial stations while simultaneously providing an analog voltage to drive the horizontal axis of 3 graphing machines. The non-dimensional instantaneous velocities, V_1/c^* and V_2/c^* , can be decomposed into their mean and fluctuating components, so that:

$$\frac{V_1}{c^*} = \frac{\bar{V}_1 + v_1}{c^*} ,$$

$$\frac{V_2}{c^*} = \frac{\bar{V}_2 + v_2}{c^*} ,$$

where \bar{V}_1 and \bar{V}_2 are the mean values of V_1 and V_2 respectively, and v_1 and v_2 are the corresponding fluctuating components.

Two three axis graphing machines were used to plot \bar{V}_1 , $\sqrt{\overline{v_1^2}}$, and V_2 , $\sqrt{\overline{v_2^2}}$ against the probe's position in the flow. Hewlett-Packard RMS voltmeters were used to measure $\sqrt{\overline{v_1^2}}$ and $\sqrt{\overline{v_2^2}}$. The time-averaged product of the fluctuating velocities, $\overline{v_1 v_2}$, was calculated by a DISA 55D70 Analog Correlator and plotted against the probe's position by a two-axis recorder.

The fluid-dynamic data-acquisition equipment had a minimum bandwidth of 40 kHz, which is adequate for the accurate measurements of the turbulence spectrum. Error in the measurements arise from two principle sources — linearization with respect to velocity and the assumption

that heat transfer from the sensor filaments depends only on the normal flow components $(M_n)_1$, $(M_n)_2$. As discussed in Appendix A the mass flux, ρV_n , is the proper parameter for linearization in a compressible flow. However, it was not possible to use this method with the dual-sensor probe because of the requirement that β be the same for both channels. The linearizers, when set-up to yield a voltage proportional to ρV_n , did not have the control range necessary to establish a common β . Since the solution of this problem would have required extensive equipment modification, linearization with respect to velocity was chosen as an alternative. Also discussed in Appendix A is the error caused by neglecting the heat transfer from a sensor-filament because of tangential and spanwise flow. Therefore, the fluid-dynamic measurements should be interpreted as qualitatively correct and useful for comparative analysis between different flow regions, but lacking in absolute accuracy.

5. THE CROSS-CORRELATION ANALYSIS

The acoustic source distribution in the flow was determined by the evaluation of the integrands of Equation (2-21). The volume integrand consists of the shear-noise component, $R_{\ddot{m}_x p'}(\tau_0)$, and the self-noise component, $R_{\ddot{m}_x^2 p'}(\tau_0)$ where,

$$R_{\ddot{m}_x p'}(\tau_o) = R_{p' \ddot{m}_x}(-\tau_o) = \overline{\left[p'(t) \times \frac{\partial^2}{\partial t^2} m_x(t-\tau) \right]}_{\tau = \tau_o} \quad (3-1)$$

$$R_{\ddot{m}_x^2 p'}(\tau_o) = R_{p' \ddot{m}_x^2}(-\tau_o) = \overline{\left[p'(t) \times \frac{\partial^2}{\partial t^2} m_x^2(t-\tau) \right]}_{\tau = \tau_o} \quad (3-2)$$

where an overbar denotes a time average. The integrand of the surface integral, $R_{p' p'}(\tau_o)$ is given by

$$R_{p' p'}(\tau_o) = R_{p' p'}(-\tau_o) = \overline{\left[p'(t) \times \frac{\partial p}{\partial t}(t-\tau) \right]}_{\tau = \tau_o} \quad (3-3)$$

The cross-correlation functions (3-1), (3-2), and (3-3) were measured using analog differentiators and a Federal Scientific UC-201A digital correlator. The signals to be cross-correlated are selected from the data tape produced at the anechoic facility. A Sangamo Sabre IV FM-tape deck was used to reproduce the recorded signals, which were subsequently re-recorded by a Sangamo 3500 FM-tape deck which was operated in the loop-mode at a speed of 60 inches per second. The Sangamo 3500 has a 20 kHz bandwidth in this configuration. Operation in the

loop-mode allows a tape-loop to be used for recording and reproduction. In this way the one minute record length of the recorded signal was synthesized into a signal with an infinite record length. This technique was necessary because the measurement of a typical cross-correlation function required approximately twenty minutes.

Figure 19 shows schematically the processing of the recorded data for the measurement of $R_{p, \ddot{m}_x}(-\tau_0)$ or $R_{p, \ddot{m}_x^2}(-\tau_0)$. Channel 8 of the tape-loop contained the 45°-microphone signal. Channels 3 and 4 contain the voltage analogs of \ddot{m}_x and \ddot{m}_x^2 , respectively. For the measurement of $R_{p, \ddot{m}_x}(-\tau_0)$, the signal on Channel 3 was processed by two analog devices each of whose output is proportional to the time-derivative of the input. The analog differentiators were designed and built at Lewis Center and had a bandwidth well above the 20 kHz limit imposed by the Sangamo 3500 tape deck. The output of the second differentiator was fed to the correlator along with the 45°-degree microphone signal. The correlator sample-time most frequently used was 5μ seconds with the number of summations being typically 65,536. The correlator digitally computes the cross-correlation function for 256 values of τ . The output of the correlator consists of 256 digital numbers which may be displayed visually on an oscilloscope and transmitted to an IBM 360 computer for

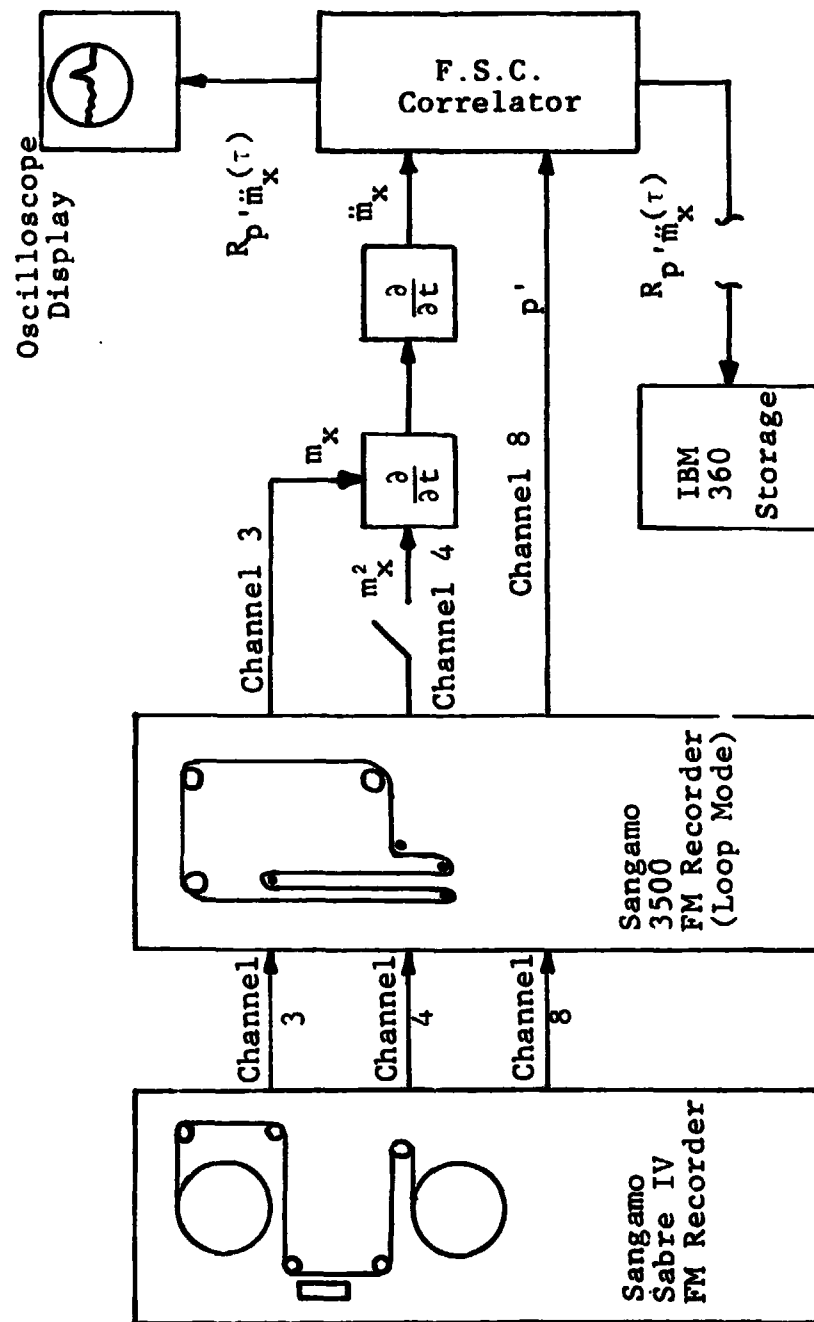


Figure 19. Cross-Correlation Analysis.

later analysis. The value of the measured cross-correlation function at $\tau = \tau_0$ is $R_{p, \ddot{m}_x}(-\tau_0)$.

The measurement of $R_{p, \dot{p}}(\tau_0)$ is similar except that \dot{p} replaces \ddot{m}_x as a correlator input.

CHAPTER IV

FLUID DYNAMIC MEASUREMENTS

1. GENERAL FLOW CHARACTERISTICS

In this chapter some features of the jet-flap flow field, as measured by a dual-sensor hot-film probe, are presented.

The probe was slowly traversed across the flow at various axial positions so that profiles of flow parameters are recorded on x-y plotters, as explained in Chapter III.

Profiles for the following flow parameters were measured for the jet-flap and compared with those made for the slot nozzle jet:

- \bar{v}_1 - the mean value of the axial velocity,
- $\sqrt{v_1'^2}$ - the rms value of the axial velocity fluctuations,
- \bar{v}_2 - the mean value of the transverse velocity,
- $\sqrt{v_2'^2}$ - the rms value of the transverse velocity fluctuations,
- $\bar{\rho} \overline{v_1 v_2}$ - the Reynold's stress.

The main features of the flow-field of the two-dimensional slot-nozzle jet and the jet-flap are shown in Figure 20. The addition of the straight flap causes the following alterations:

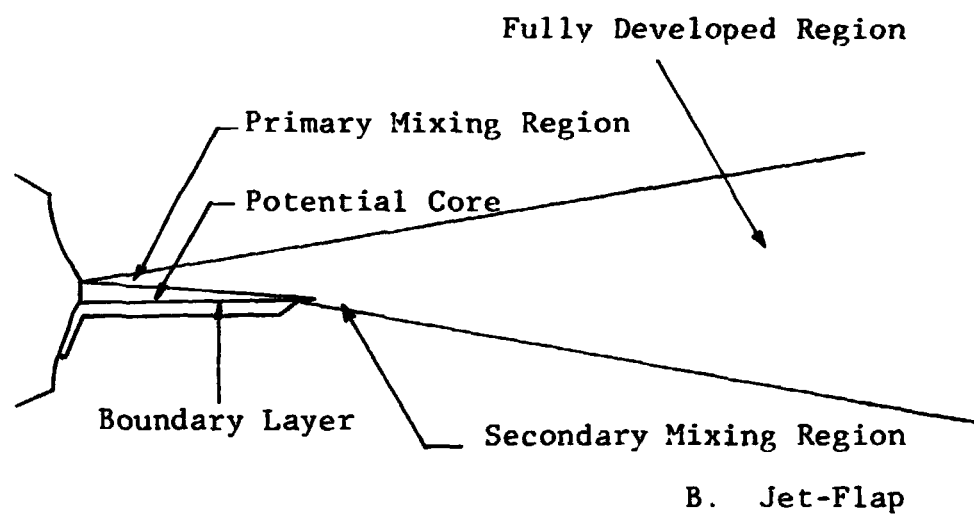
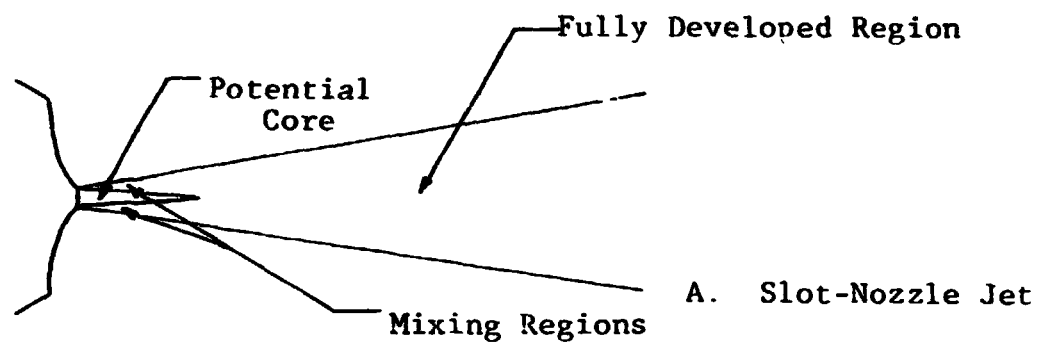


Figure 20. Flow Features of the Slot-Nozzle Jet and the Jet Flap.

- (i) The mixing region on the flap-side of the jet disappears.
- (ii) A boundary layer is formed on the flap surface,
- (iii) A secondary mixing region is formed aft of the flap trailing edge.

Schrecker [2] has conducted a comprehensive acoustic and fluid dynamic study of slot-nozzle jets with and without attached straight flaps and concluded that the secondary mixing region produces at least as much noise as the primary mixing region. Schrecker calculated the acoustic source strength in the primary and secondary mixing regions using an expression derived by Lilley [12], and for some jet-flap configurations, the calculated acoustic source strength was an order of magnitude greater in the secondary region than in the primary region. His measurements indicated that the maximum value of $\sqrt{v_1^2}$ in the secondary region is greater than its maximum value in the primary region, and that high values of mean shear, $\partial V_1 / \partial X_2$, exist near the flap trailing edge.

The test slot-nozzle jet has an exit-plane Mach number of .7 and a flat velocity profile across the width of the jet. The calculated sonic velocity at the nozzle exit-plane, based on the average static temperature of the stilling chamber, was 1150 ft./sec., making the exit velocity 805 ft./sec. The Reynold's number of the jet-flap

configuration, based on the flap length and the exit velocity, was 1.92×10^7 . The flow-field of the jet-flap near the plane of transverse symmetry ($X_3 = 0$) is approximately two dimensional in the sense that:

$$v_3 \approx 0, \quad (4-1)$$

and

$$\frac{\partial \dots}{\partial x_3} \approx 0.$$

Of course, since the slot nozzle has a finite span, the above conditions will not be satisfied near the spanwise boundaries of the flow.

2. THE AXIAL MEAN VELOCITY PROFILES

Figure 21 shows profiles of \bar{V}_1 for the slot-nozzle jet without the flap which have been normalized by c^* the sonic velocity at the jet exit plane. It is clear that the \bar{V}_1 profiles are symmetric with respect to the X_1 -axis. The velocity at $X_1/h = 1$ is still essentially uniform across the width of the jet. The potential core is still evident at $X_1/h = 5$, by the flattened peak at the center of the profile, but it is not present at $X_1/h = 7$. The \bar{V}_1 profile measured $X_1/h = 6$ (not displayed) also has a narrow flattened peak, therefore the end of the potential core is between $X_1/h = 6$ and $X_1/h = 7$.

The highest values of mean shear, $\partial V_1 / \partial X_2$, occur near the nozzle exit, where the mixing layers are very thin. As

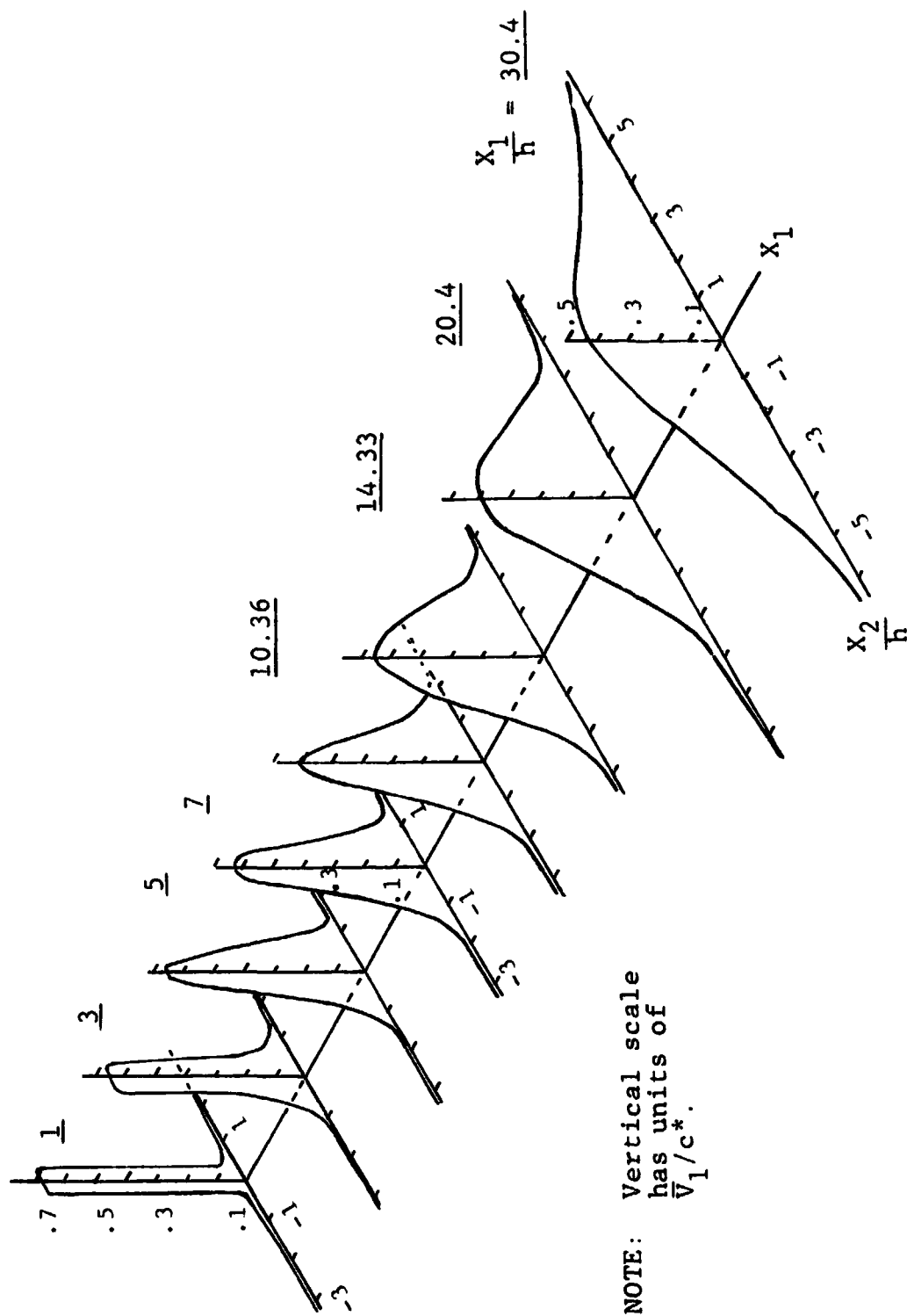


Figure 21. Axial Mean Velocity Profiles for the Slot-Nozzle Jet.

the jet develops, the slope of the \bar{V}_1 profiles decrease because of the entrainment of ambient air and the spreading of the turbulent mixing regions on each side of the potential core.

The maximum value of \bar{V}_1 occurs along the jet centerline and decreases with increasing axial position. The decay of centerline value of \bar{V}_1 is displayed in Figure , where the exit-plane velocity of the jet, $(V_1)_e$, has been used for normalization. The centerline velocity drops only about 8 percent in the first ten slot-nozzle heights because of the existence of the potential core. Downstream of $X_1/h = 10$ the shape of the decay curve changes abruptly, indicating that the two mixing regions have merged. Downstream of $X_1/h = 14$ the centerline velocity can be predicted to within 10 percent using the relationship,

$$\frac{\bar{V}_1}{(V_1)_e} = \frac{3.46}{\sqrt{X_1/h}} \quad (4-2)$$

As may be seen in Figure 22, equation (4-2) becomes more accurate with increasing downstream distance.

The axial mean velocity profiles for the jet-flap are shown in Figure 23. The presence of the flap destroys the symmetry of the flow, although a tendency toward symmetry is apparent far downstream; this is evident from the profile taken at $X_1/h = 30.4$. The first four profiles, which are

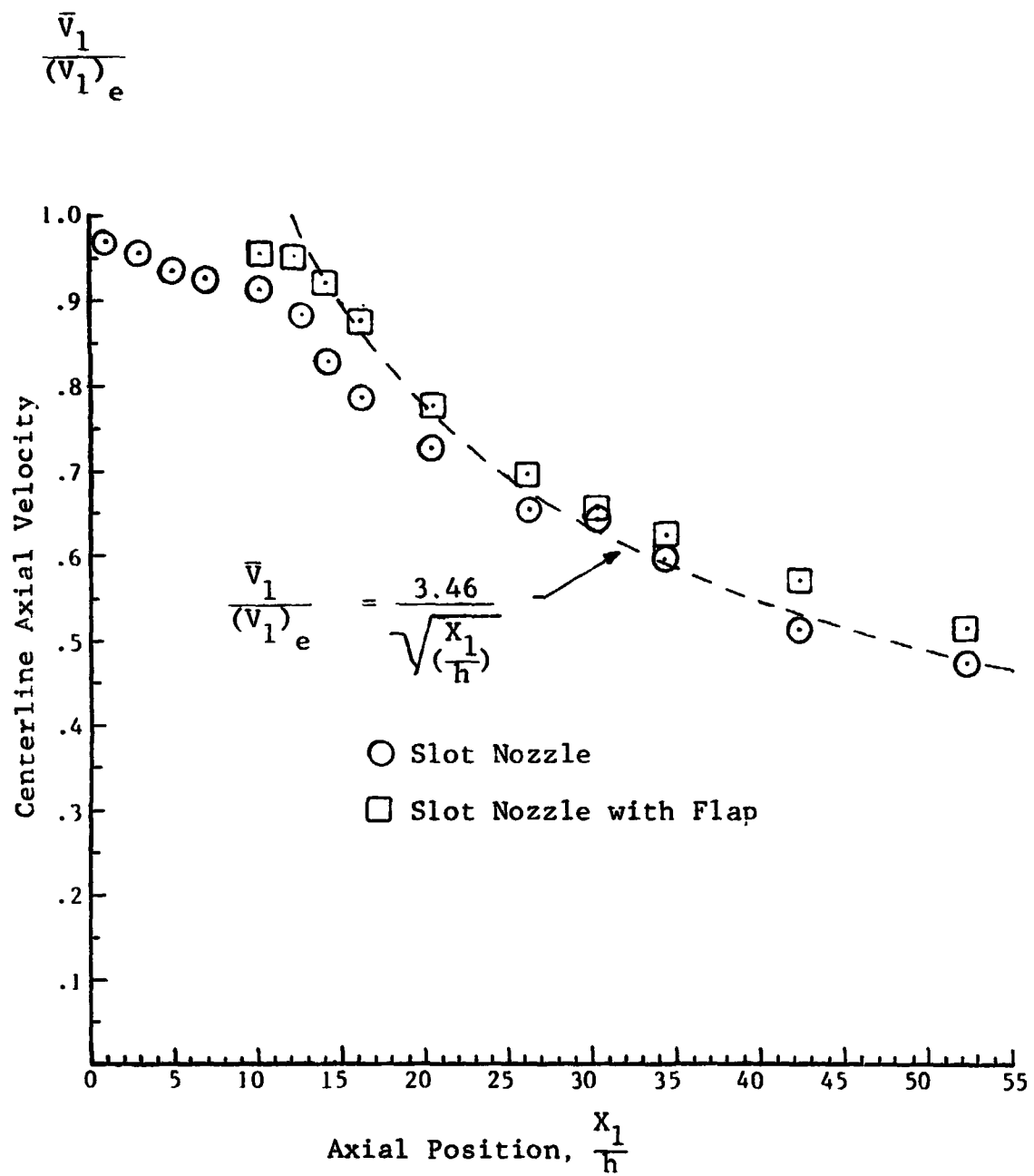


Figure 22. Centerline Axial Velocity Decay.

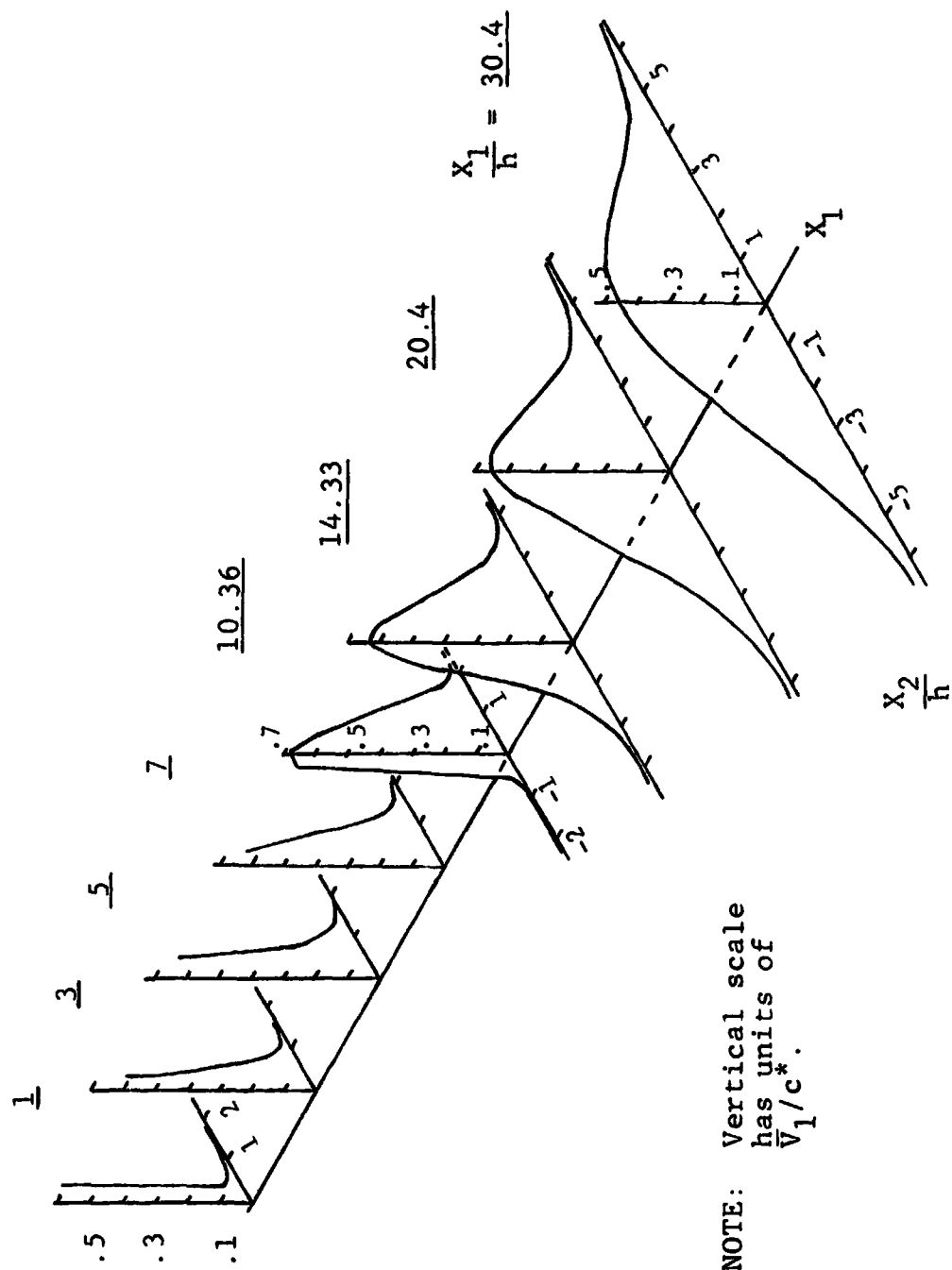


Figure 23. Axial Mean Velocity for the Slot-Nozzle Jet with Flap.

taken above the flap, are truncated because the flap surface prevented further inward movement of the probe. The profiles taken in the primary mixing region above the flap appear to differ little from their counterparts in the free jet.

The truncated profiles do not show the extended length of the potential core above the flap surface. This extension occurs because the presence of the flap allows turbulent mixing only on one side of the jet. The extended potential core is still evident by the flattened peak of the profile measured at $X_1/h = 10.36$ near the flap trailing edge, but it disappears quickly after about one slot-nozzle height.

The maximum value of $\partial \bar{V}_1 / \partial X_2$ in the secondary mixing-region is almost twice the maximum value of $\partial \bar{V}_1 / \partial X_2$ measured in the free jet at $X_1/h = 1$. The mean shear is approximately equal to the X_3 -component of the mean vorticity vector, $\bar{\Lambda}_3$. The concentration of $\bar{\Lambda}_3$ at the flap trailing-edge is rapidly diffused, as is evident by the gentle slope of the axial mean velocity in the secondary region at the downstream position of $X_1/h = 14.33$. The rapid diffusion of $\bar{\Lambda}_3$ is facilitated because the secondary mixing region becomes highly turbulent.

The decay of the centerline value of \bar{V}_1 for the jet-flap is also shown in Figure 22. It is interesting to note that the centerline value of \bar{V}_1 can be accurately predicted

by Equation (4-2) almost to the flap trailing edge. In view of the complicated nature of the flow field aft of the flap trailing edge, it is remarkable that such a simple relationship exists.

3. THE AXIAL TURBULENCE INTENSITY PROFILES

The axial turbulence intensity is defined to be

$$\Phi = \frac{\sqrt{v_1^2}}{(v_1)_e} \times 100 ,$$

where,

v_1 = the fluctuating component of the
axial velocity.

Figure 24 illustrates the axial turbulence intensity profiles for the slot-nozzle jet. The profiles are symmetric with respect to X_1 -axis; the twin peaks are the turbulent mixing regions on each side of the jet. At $X_1/h = 1$, the mixing regions are very thin and are separated by a comparatively wide and deep trough. The trough is the potential core of the jet. The downstream development of the jet is characterized by a spreading of the mixing regions and a "filling-in" of the trough between them. The axial turbulence intensity along the jet centerline is less than 2 percent for the first five slot-nozzle heights. The centerline intensity rises to 3 percent at $X_1/h = 7$, which is slightly downstream of the potential core terminus.

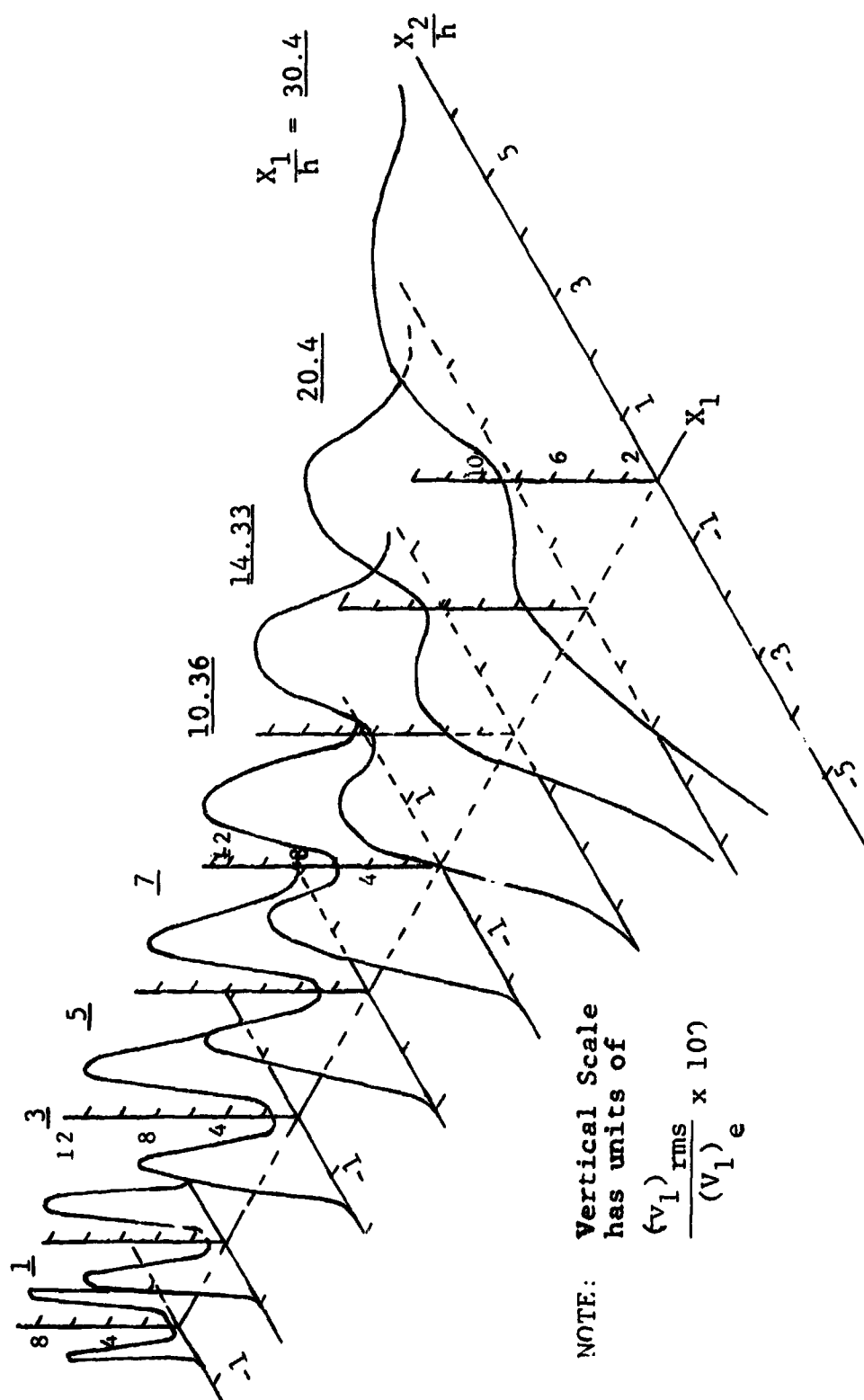


Figure 24 Axial Turbulence Intensity Profiles for the Slot-Nozzle Jet.

The corresponding profiles for the jet-flap are shown in Figure 25. The lack of symmetry is apparent. The truncated profiles of the primary mixing region above the flap differ little from their free-jet counterparts, except near the potential core. The profile made near the trailing edge at $X_1/h = 10.36$, shows the formation of the secondary mixing region which appears as a small peak to the left of the X_1 -axis. Note the low value of axial turbulence intensity near the jet centerline indicating the remnant of the potential core. The strength of the axial turbulence intensity in the secondary mixing region grows rapidly and becomes dominant. This can be seen from the profiles made at $X_1/h = 14.33$ and $X_1/h = 20.4$. However, the strength of the axial turbulence intensity in the secondary region falls quickly so that the profile measured at $X_1/h = 30.4$ shows the turbulence intensity in the secondary mixing region is less than that in the primary region.

The dynamics of the turbulent mixing regions may be seen in Figure 26, which is a plot of the maximum axial turbulence intensity for each profile. The value of ϕ_{\max} for the free jet increases almost linearly for the first 10 slot-heights, where a maximum occurs. This value remains approximately constant for about two slot heights, after which slightly lower values of ϕ_{\max} are measured. However, this trend is reversed near $X_1/h = 16$ and ϕ_{\max} begins to

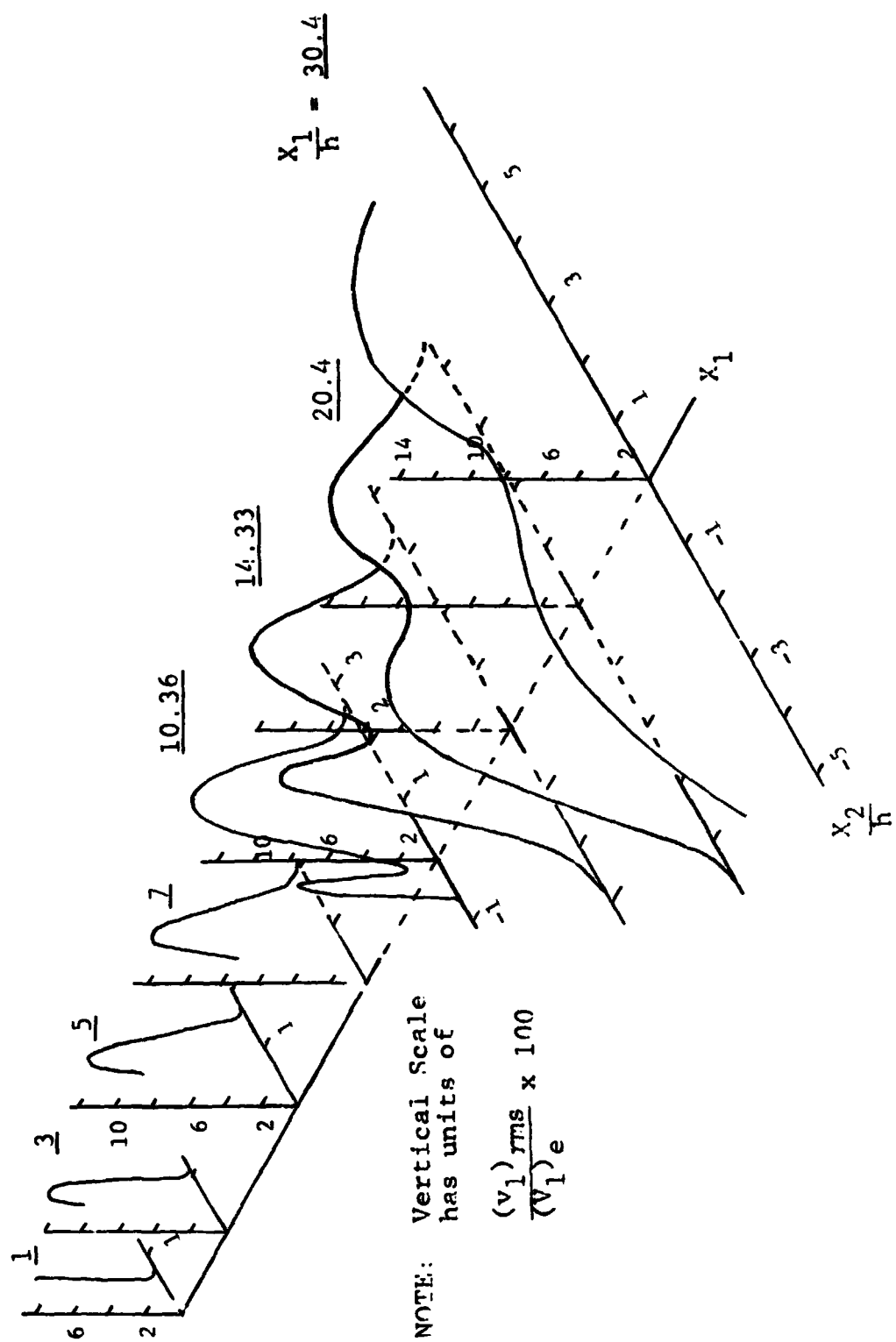


Figure 25. Axial Turbulence Intensity Profiles for the Slot-Nozzle Jet with Flap.

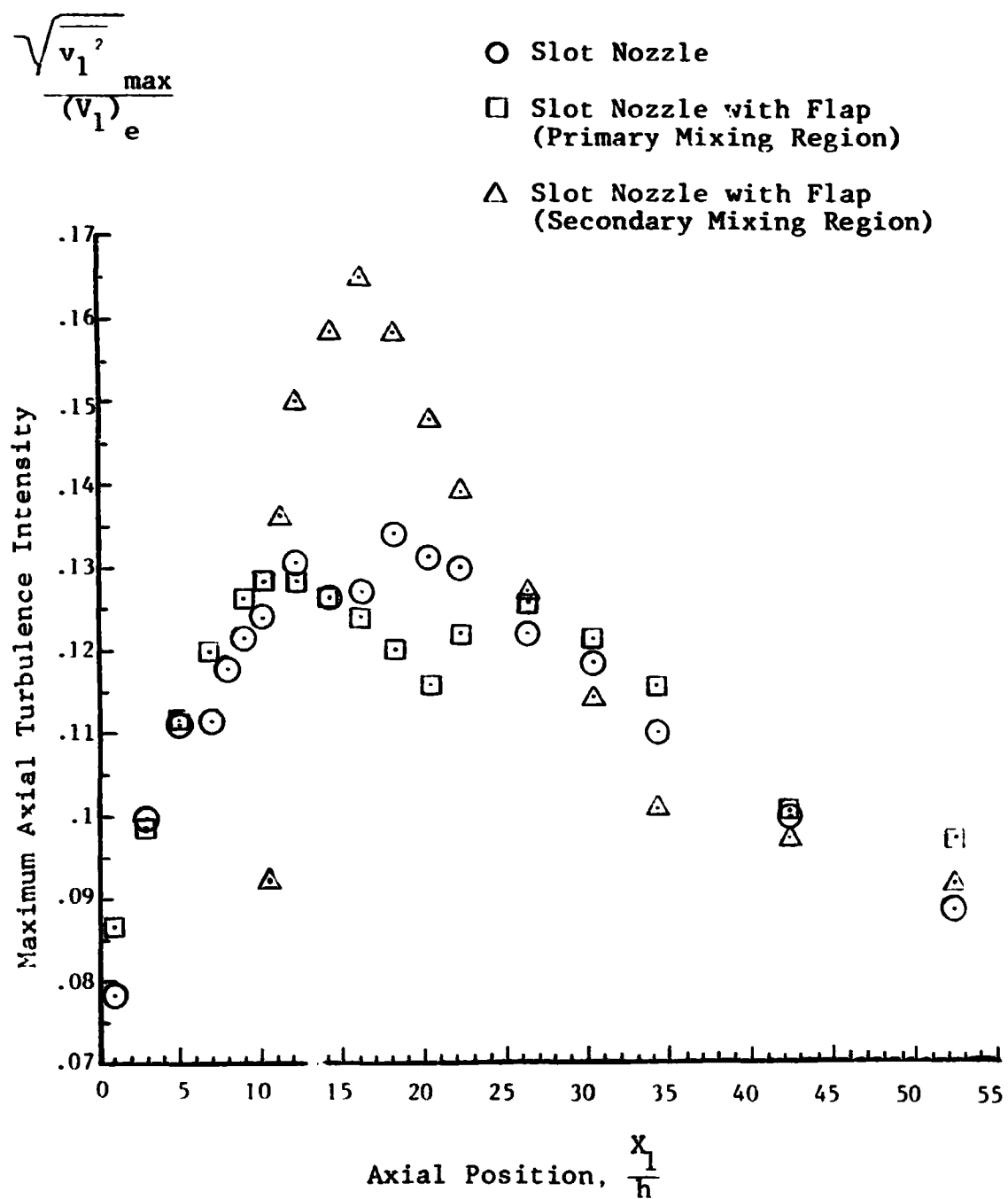


Figure 26. Maximum Axial Turbulence Intensities.

increase. The absolute maximum of ϕ_{\max} occurs about 18 slot heights downstream of the nozzle exit plane, after which ϕ_{\max} decays slowly with X_1/h . At $X_1/h = 22$, ϕ_{\max} is again approximately the same value as it was at the first maximum located near $X_1/h = 11$. The first maximum of ϕ_{\max} occurs at the place where the two mixing regions are merging, which creates a highly turbulent flow field. However, the reason for the existence of the absolute maximum of ϕ_{\max} so far downstream is not understood.

The introduction of the flap does not appreciably change the values of ϕ_{\max} in the primary mixing region above the flap. However, there are some changes in the values of ϕ_{\max} in the primary mixing region aft of the flap trailing edge. The addition of the flap delays the formation of the second maximum until about 26 slot-nozzle heights. Unlike the free jet, the second maximum for the jet-flap is less than the first maximum.

The plot of ϕ_{\max} in the secondary mixing region illustrates the difference between the dynamics of turbulence in the secondary mixing region and in the primary mixing region. The value of ϕ_{\max} in the secondary region increases rapidly to its peak at $X_1/h = 16.3$, and then quickly decreases. About 26 slot-heights downstream the value of ϕ_{\max} in the primary and secondary mixing regions is approximately equal. Further downstream the value of ϕ_{\max} in the primary region dominates.

4. THE TRANSVERSE MEAN VELOCITY PROFILES

The transverse mean velocity profiles for the slot-nozzle jet are shown in Figure 27. The profiles of \bar{V}_2 are anti-symmetric with respect to the X_1 -axis, so that a negative value of \bar{V}_2 on the right side of the jet-centerline and a positive value on the left side indicate a flow toward the jet-centerline. The value of \bar{V}_2 in the potential core is zero, as can be seen in the profiles measured at $X_1/h = 1, 3, 5$, and, unlike the axial mean velocity, the profiles of \bar{V}_2 reach their peak values near the center of the turbulent mixing regions. The highest peak values of \bar{V}_2 are found near the nozzle exit plane; the maximum absolute-value of V_2 appears to decrease monotonically with downstream position. The absolute-value of \bar{V}_2 is small compared with \bar{V}_1 everywhere in the flow, at least within the first 50 slot-nozzle heights, being of the same order of magnitude as the axial turbulence intensity. The profiles made at $X_1/h = 14.33, 20.4, 30.4$, indicate regions of reverse flow exist near the jet boundary. It is possible that these are regions of swirling flow induced by large-scale turbulent eddies in the jet mixing region. The profiles of \bar{V}_2 for the jet-flap are shown in Figure 28. The values of \bar{V}_2 above the flap are not appreciably changed. In the secondary mixing region, near the flap trailing edge, there exist a relatively high maximum value of \bar{V}_2 , as can be seen in the $X_1/h = 10.36$

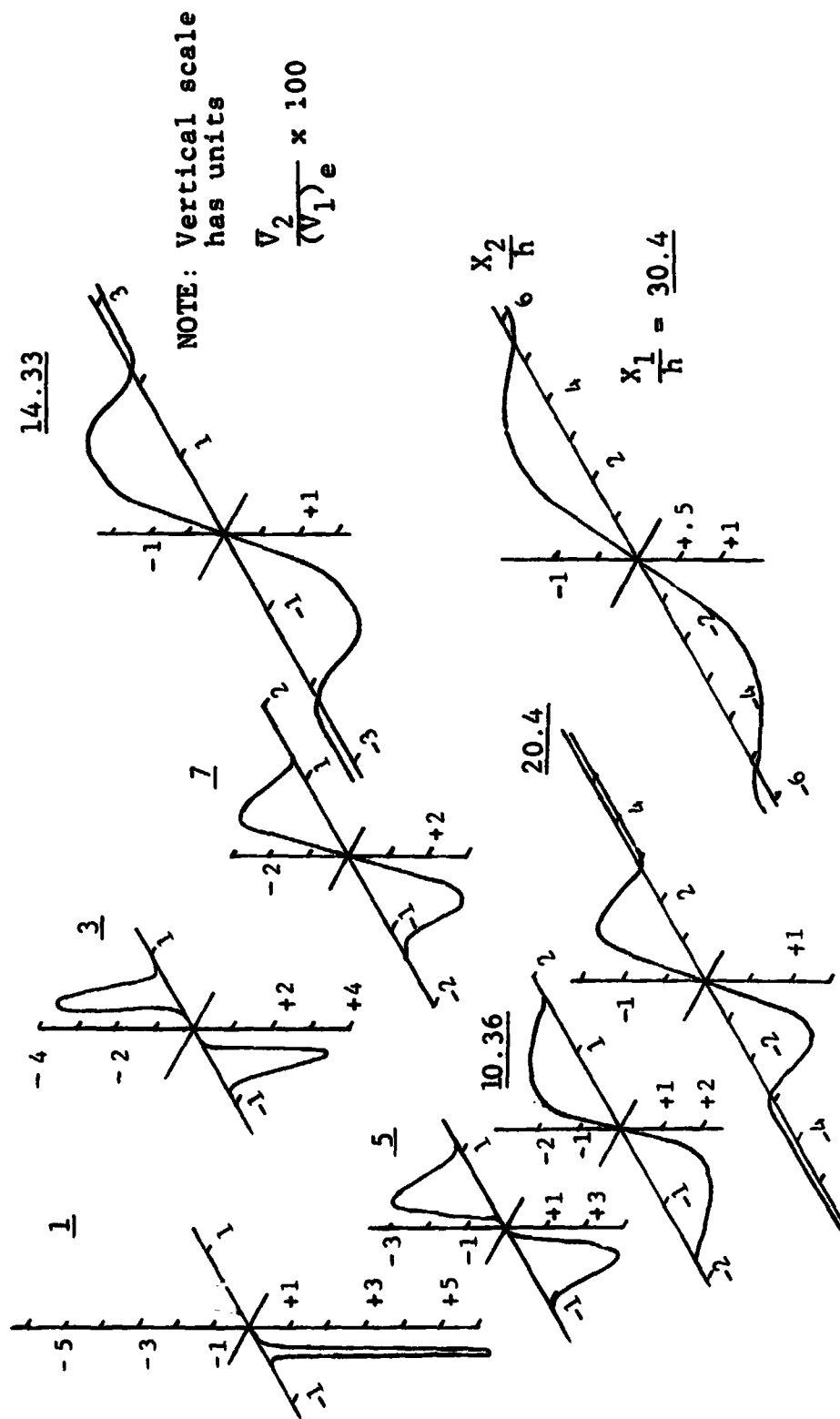


Figure 27. Transverse Mean Velocity Profiles for Slot-Nozzle Jet.

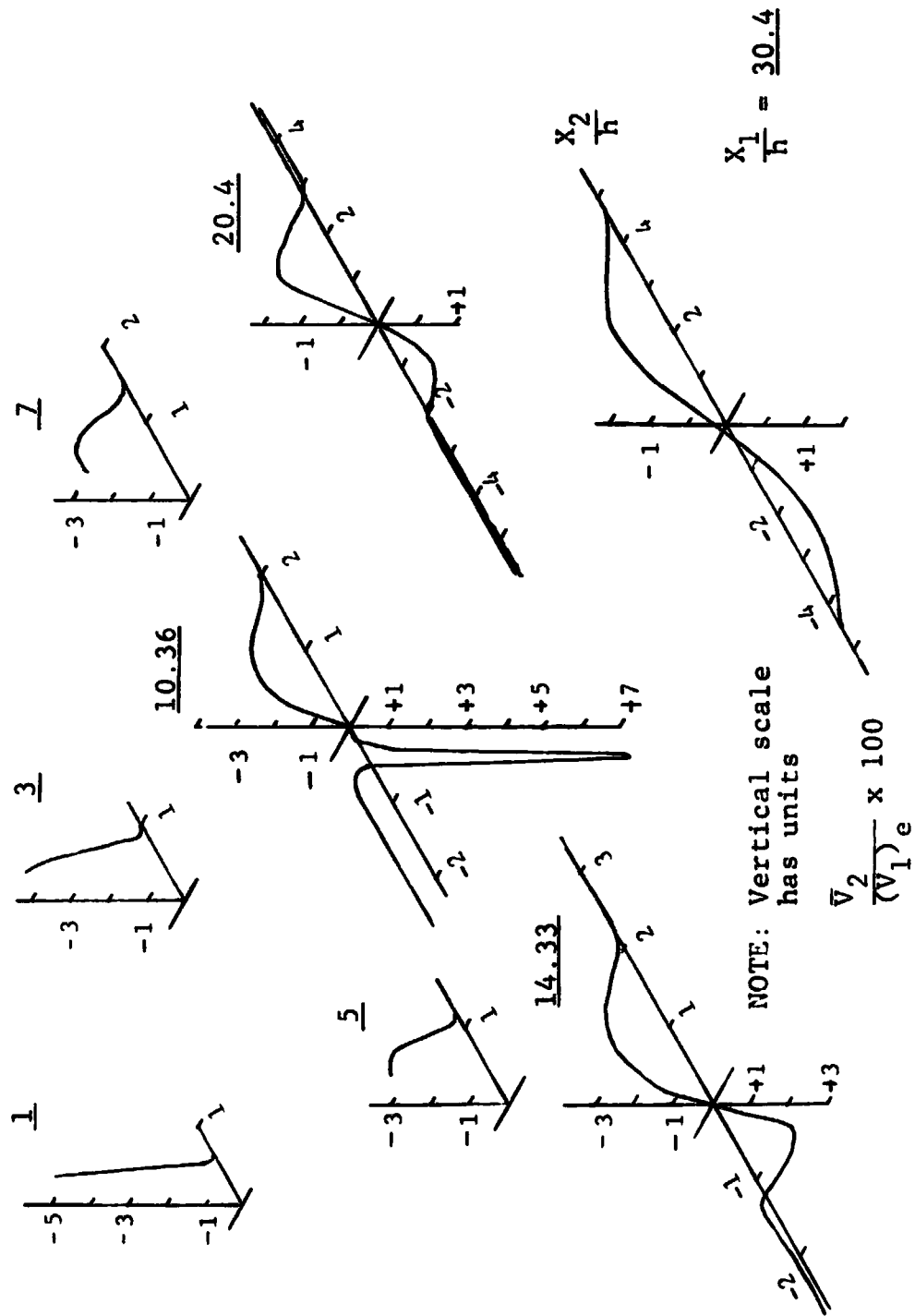


Figure 28. Transverse Mean Velocity Profiles for Slot-Nozzle Jet with Flap.

profile. Note also that outside of the secondary mixing region there exists an area of reverse flow. The maximum value of \bar{V}_2 in the secondary mixing region drops very sharply, so that by $X_1/h = 14.33$, it is approximately the same there as in the primary mixing region. Thereafter, the maximum value of \bar{V}_2 in the secondary mixing region is somewhat less than in the primary mixing region all the way out to $X_1/h = 52.4$.

5. THE TRANSVERSE TURBULENCE INTENSITY PROFILES

The transverse turbulence intensity is defined to be:

$$\Omega = \frac{\sqrt{\overline{v_2^2}}}{(v_1)_e} \times 100 .$$

The profiles of Ω for the slot nozzle jet are displayed in Figure 29. These profiles appear similar in shape to those made for ϕ , the axial turbulence intensity, exhibiting the characteristic spreading of the mixing regions and the erosion of the potential core. However, a graph of Ω_{\max} for each profile reveals a difference in the two turbulence quantities. This graph is shown in Figure 30. The value of Ω_{\max} does not vary more than the 1 percent over the first 30 slot-nozzle heights, after which Ω_{\max} decays slowly with X_1/h . This is in contrast to the behavior of ϕ_{\max} , which rises almost linearly

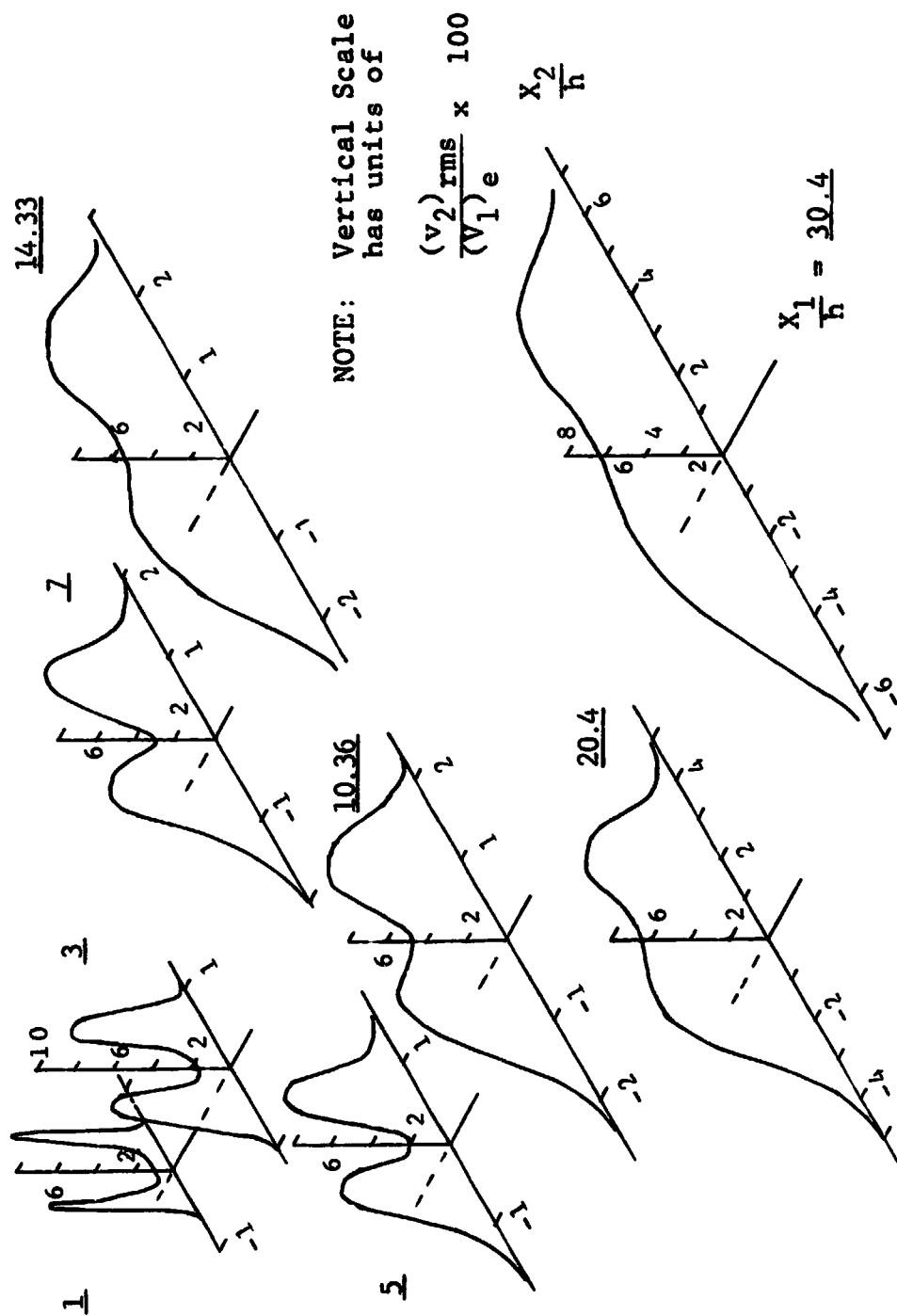


Figure 29. Transverse Turbulence Intensity Profiles for Slot-Nozzle Jet.

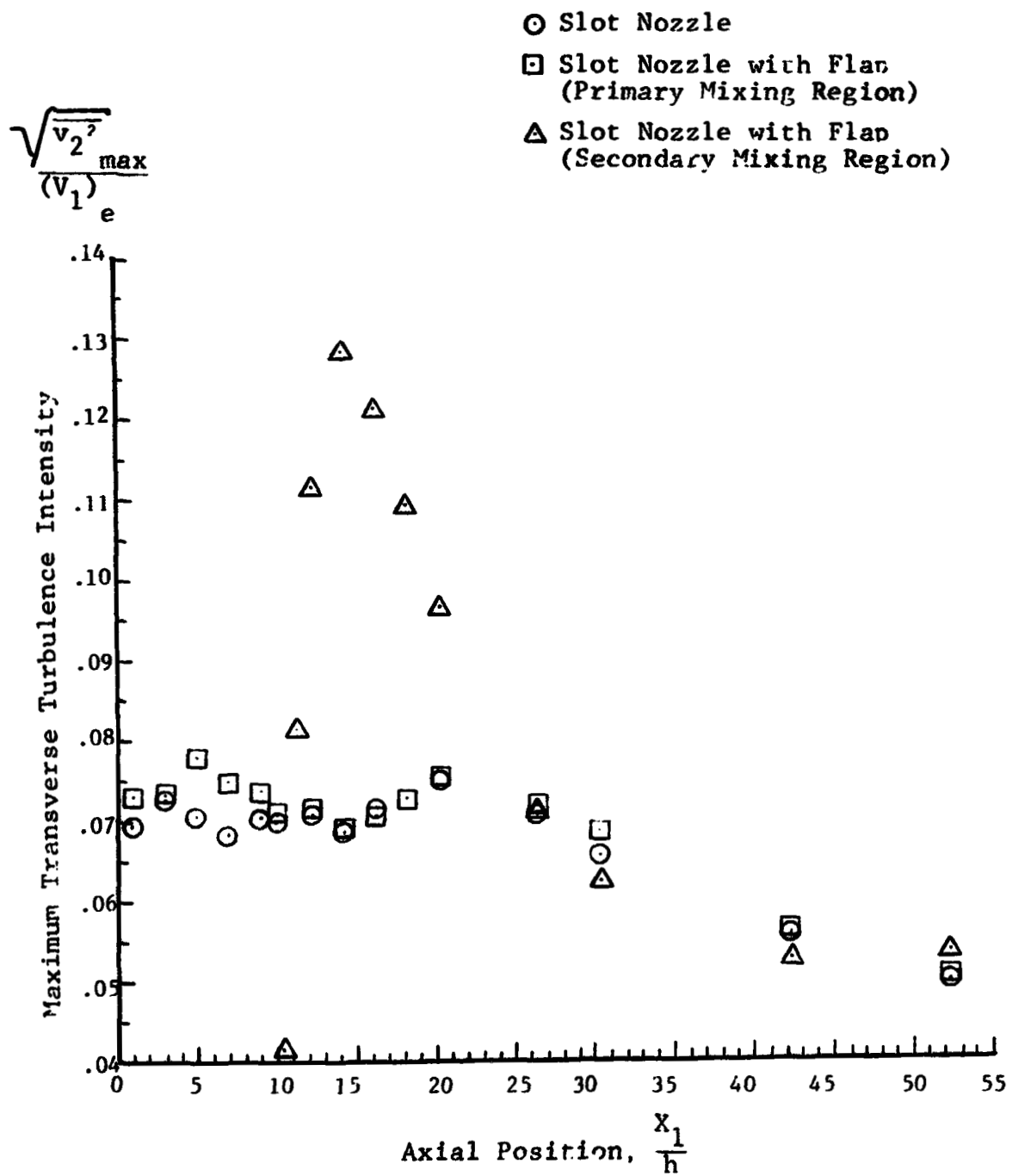


Figure 30. Maximum Transverse Turbulence Intensities.

to about $X_1/h = 10$, remains constant within 1 percent out to about $X_1/h = 26$, and drops steadily with increasing axial position thereafter.

It is interesting to note that while Ω_{\max} is essentially constant over the first 30 slot-nozzle heights, (about 7 percent), the deviation of individual values of Ω_{\max} from this constant value seem to be almost periodic with X_1/h up to $X_1/h = 15$. Relative maximums are seen at $X_1/h = 3$ and $X_1/h = 10$, minimums at $X_1/h = 7$ and $X_1/h = 14$, so that the distribution has a wavelength of $X_1/h = 7$ or 2.1 inches. The physical significance, if any, of this periodic behavior is not clear. Furthermore, note that the spacing between the two maximum values of the axial turbulence intensity in Figure 26, is approximately equal to a value of $X_1/h = 7$.

The profiles of Ω for the jet-flap are shown in Figure 31, and are seen to have about the same appearance as the Φ profiles for the jet-flap. However the "saddle", which results from the relative lower turbulence on the jet-centerline in the Ω profiles is, in general, not as well defined as in the Φ profiles.

Figure 30 shows that the value of Ω_{\max} in the primary mixing regions is about the same compared to its value in the free-jet. However, the apparent periodic distribution of the values has changed with the addition

of the flap, so that the wavelength now as an approximate value of $X_1/h = 15$. This is about twice the value for the free jet. Reference to Figure 26 shows the same behavior for the graph of ϕ_{\max} for the jet-flap; the two maximum values of ϕ_{\max} are separated by a value of approximately $X_1/h = 15$. This is about twice the previous separation.

The graph of Ω_{\max} for the secondary mixing region is also presented in Figure 30. The peak value of Ω_{\max} occurs near $X_1/h = 14$, approximately 2 slot-heights upstream of the position of ϕ_{\max} . While the peak value of Ω_{\max} in the secondary-mixing region is slightly lower than the corresponding peak value of ϕ_{\max} , its dominance over the peak value of Ω_{\max} in the primary mixing region is more pronounced. Also, while Ω_{\max} rises to its peak and decays more rapidly than ϕ_{\max} , both become equal to their corresponding values in the primary mixing region at about the same axial position of $X_1/h = 25$.

6. THE REYNOLD'S STRESS PROFILES

Following Schubauer and Tchen [13], the Reynold's Stress for a compressible, two dimensional, boundary-layer type flow, is

$$\tau^* = \bar{\rho} \overline{v_1 v_2} ,$$

where $\bar{\rho}$ is the average value of the local density in the jet.

In the equation for the turbulence kinetic energy (see Schubauer and Tchen) the product

$$\tau^* \frac{\partial V_1}{\partial X_2}$$

is interpreted as a source term. Furthermore, since $|\tau^*| \ll |\partial V_1 / \partial X_2|$ in the early development of the primary and secondary mixing regions, τ^* assumes the role of a coupling factor. That is, the local value of τ^* determines how efficiently the turbulence can extract energy from the main flow.

Profiles $\tau^* / \bar{\rho}$ measured for the slot-nozzle jet are shown in Figure 32, and are seen to be anti-symmetric with respect to the X_1 -axis. The value of $|\tau^*|$ in the potential core is zero, as is evident from the spacing between the anti-symmetric peaks of the first three profiles. Downstream of the potential core terminus the two mixing regions of the jet merge, causing the space between the peaks of the profiles measured at $X_1/h = 7$ and 10.36 to be eliminated. Downstream of $X_1/h = 10.36$, τ^* is seen to vary almost linearly with X_2/h between anti-symmetric peaks.

Figure 33 illustrates the profiles for $\tau^* / \bar{\rho}$ for the jet-flap configuration. The first two profiles taken above the flap surface indicate significantly higher absolute values of τ^* there compared to their free-jet

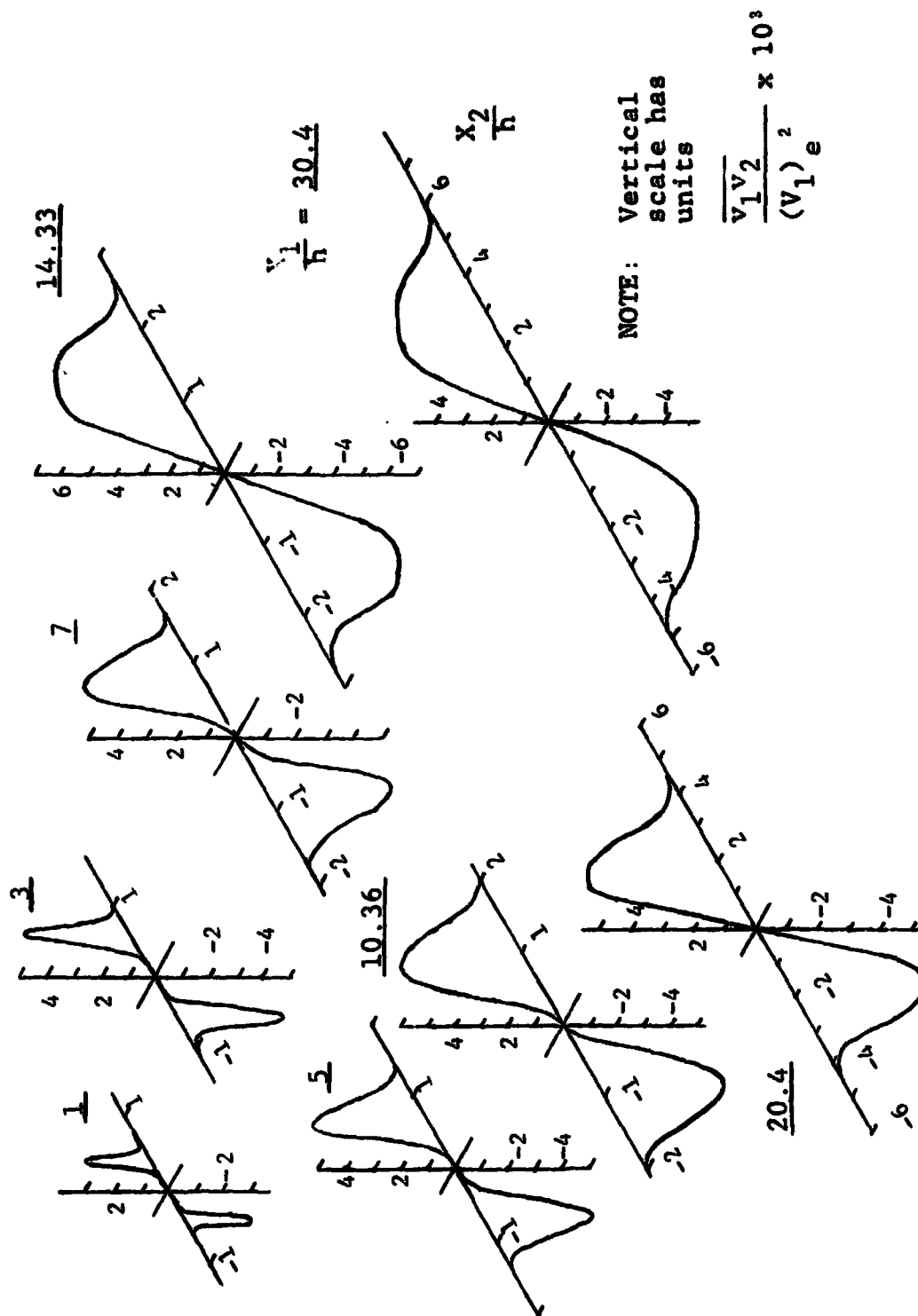


Figure 32. Reynolds's Stress Profiles for Slot-Nozzle Jet.

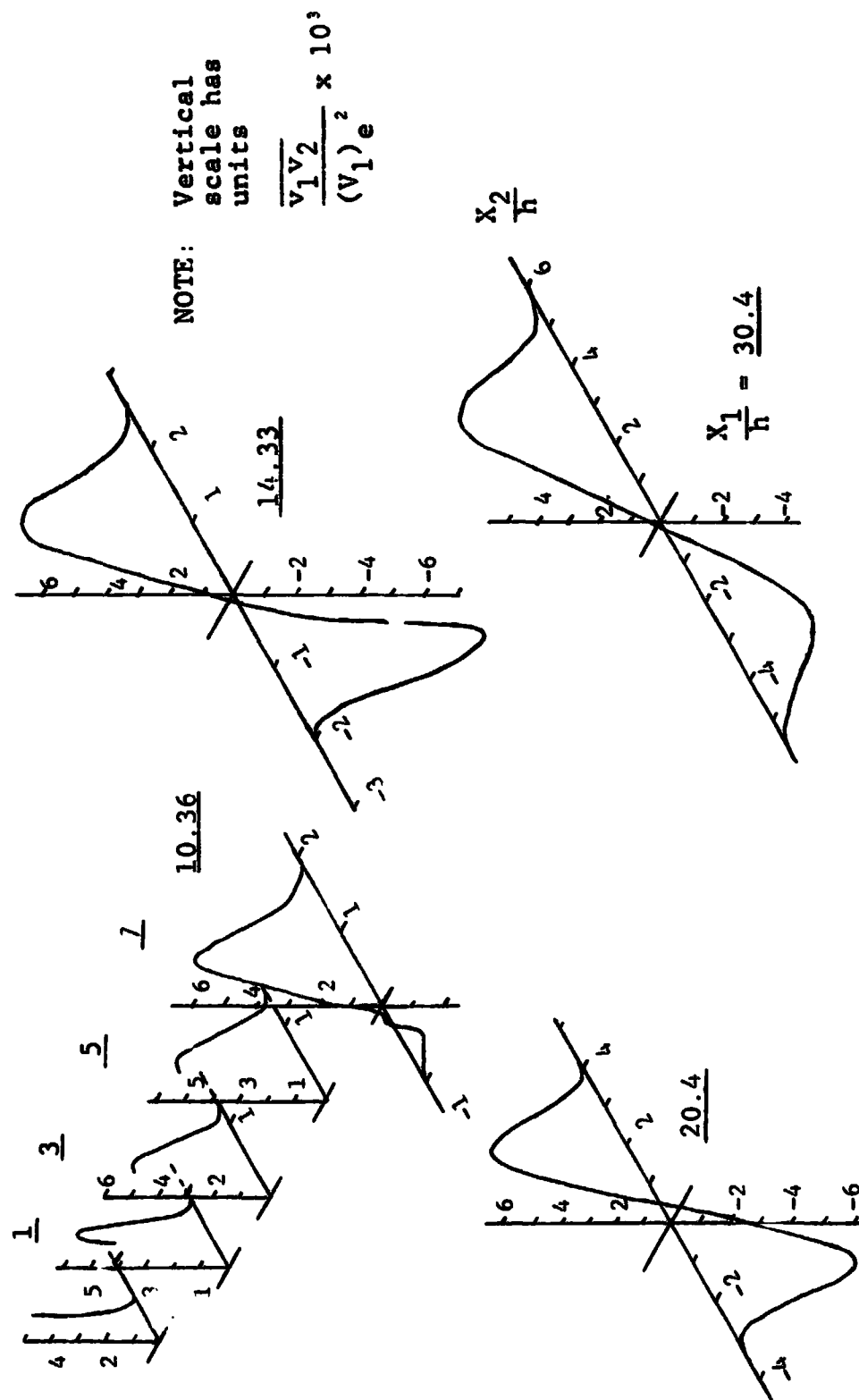


Figure 33. Reynold's Stress Profiles for Slot Nozzle with Flap.

counterparts, while the profiles taken at $X_1/h = 5$ and 7 appear quite similar to those in the free-jet. Higher absolute values of τ^* are also seen in the profiles made in the primary mixing region aft of the flap trailing edge. In the secondary mixing region, near the flap trailing edge ($X_1/h = 10.36$), the absolute values of τ^* are seen to be very small. The absolute value of τ^* in the secondary mixing-region rises and falls rapidly in a manner similar to the other turbulence quantities. The profile measured at $X_1/h = 30.4$ seems to show a tendency toward the anti-symmetric distribution of τ^* found in the free-jet.

A graph of the peak values of the τ^* profiles measured for the free-jet and jet-flap are shown in Figure 34. Since the peak values will be both positive and negative, the maximum values of $|\tau^*|$, are plotted, that is,

$$\frac{|\tau^*|_{\max}}{(V_1)_e^2 \bar{\rho}} = \frac{|\overline{v_1 v_2}|_{\max}}{(V_1)_e^2}$$

In the free-jet $|\tau^*|_{\max}$ appears to increase steadily for the first 9 slot-nozzle heights downstream; then it remains relatively constant to $X_1/h = 20$, after which a steady decay is observed.

The curve plot for the primary mixing-region of the jet-flap shows the distribution of $|\tau^*|_{\max}$ to be

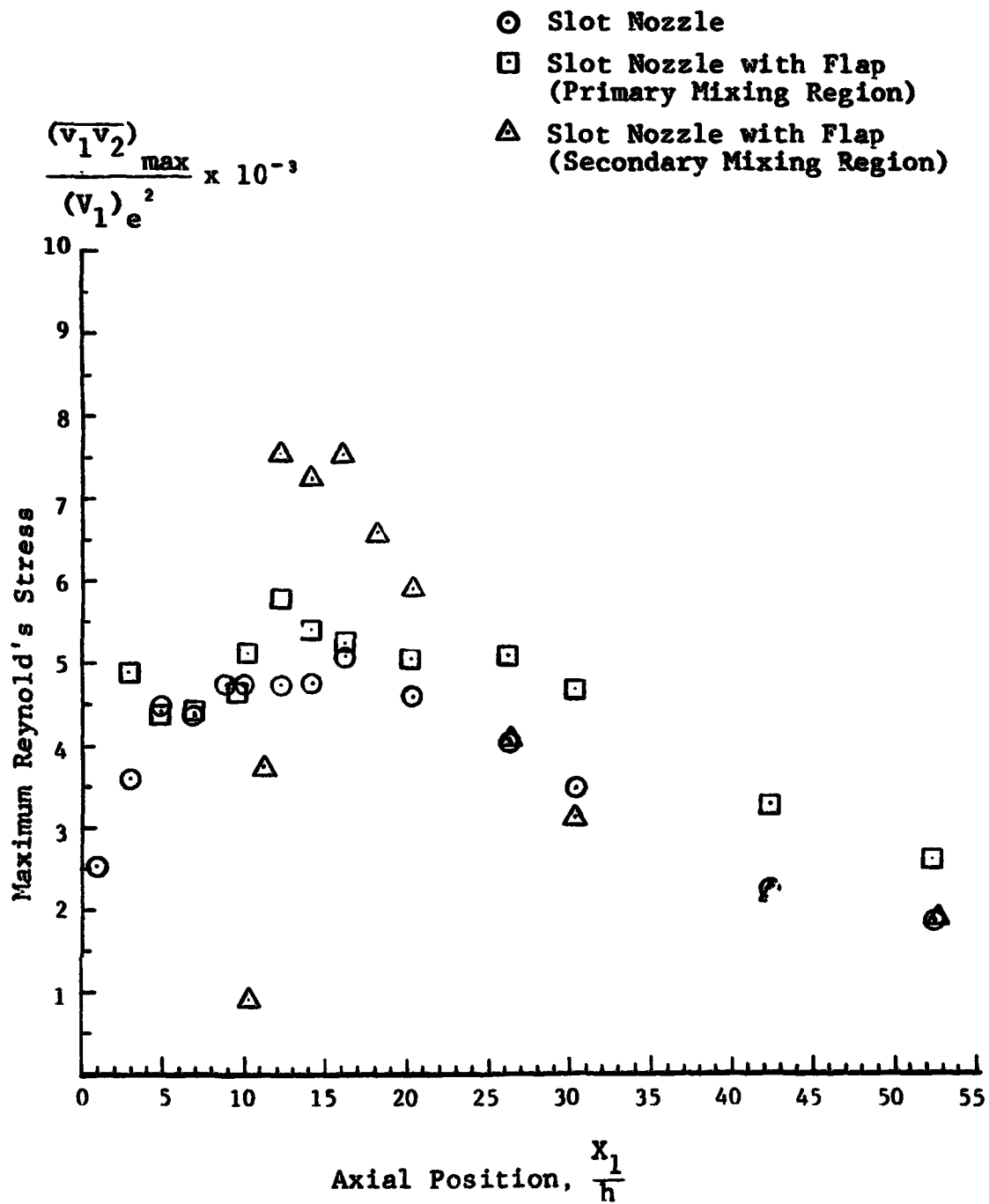


Figure 34. Maximum Values of the Reynold's Stress.

different than in the free-jet mixing region. The values of $|\tau^*|_{\max}$ are, in general, higher than their free-jet counterparts, but of more interest is the fact that, unlike the free-jet, $|\tau^*|_{\max}$ does not increase with axial position for the first 10 slot-heights. Instead, it appears to oscillate about a relatively constant value, in much the same manner as the results presented for Ω_{\max} in Figure 30. A well-defined decay of $|\tau^*|_{\max}$ in the primary region is not seen until after $X_1/h = 30$.

The curve for the secondary mixing-region shows the rapid development of $|\tau^*|_{\max}$ there which has been characteristic of all the turbulence quantities which were measured. However, unlike the curves for ϕ_{\max} and Ω_{\max} in the secondary mixing-region, the curve for $|\tau^*|_{\max}$ has a flat peak, so that $|\tau^*|_{\max}$ retains a relatively high peak value for about 4 slot-nozzle heights, after which a rapid roll-off occurs.

CHAPTER V

ACOUSTIC MEASUREMENTS AND SOURCE LOCATION

1. INTRODUCTION

In this chapter the far-field acoustic data for the jet-flap and slot-nozzle jet are examined and compared. In addition, the characteristics of the acoustic sources associated with the fluctuating momentum and pressures in the jet-flap flow, as measured by the single-sensor hot film and embedded microphones, respectively, are presented. Finally, the contribution of these flow sources to the far-field sound, which is measured at the 45°-microphones, is evaluated using the cross-correlation technique.

2. DIRECTIVITY AND SPECTRA OF THE FAR-FIELD SOUND

Directivity measurements of the far-field sound pressure level (SPL) produced by the jet and jet-flap were obtained using the quarter-circle of microphones as described in Chapter III. The contours of SPL in the X_1X_2 -plane (flyover plane) for the jet-flap and the jet are shown in Figure 35A. The SPL contour of the jet is symmetric with respect to the X_1 -axis, so values are only shown for positive values of ϕ . The maximum SPL which was measured for the jet occurs at $\phi = 45^\circ$.

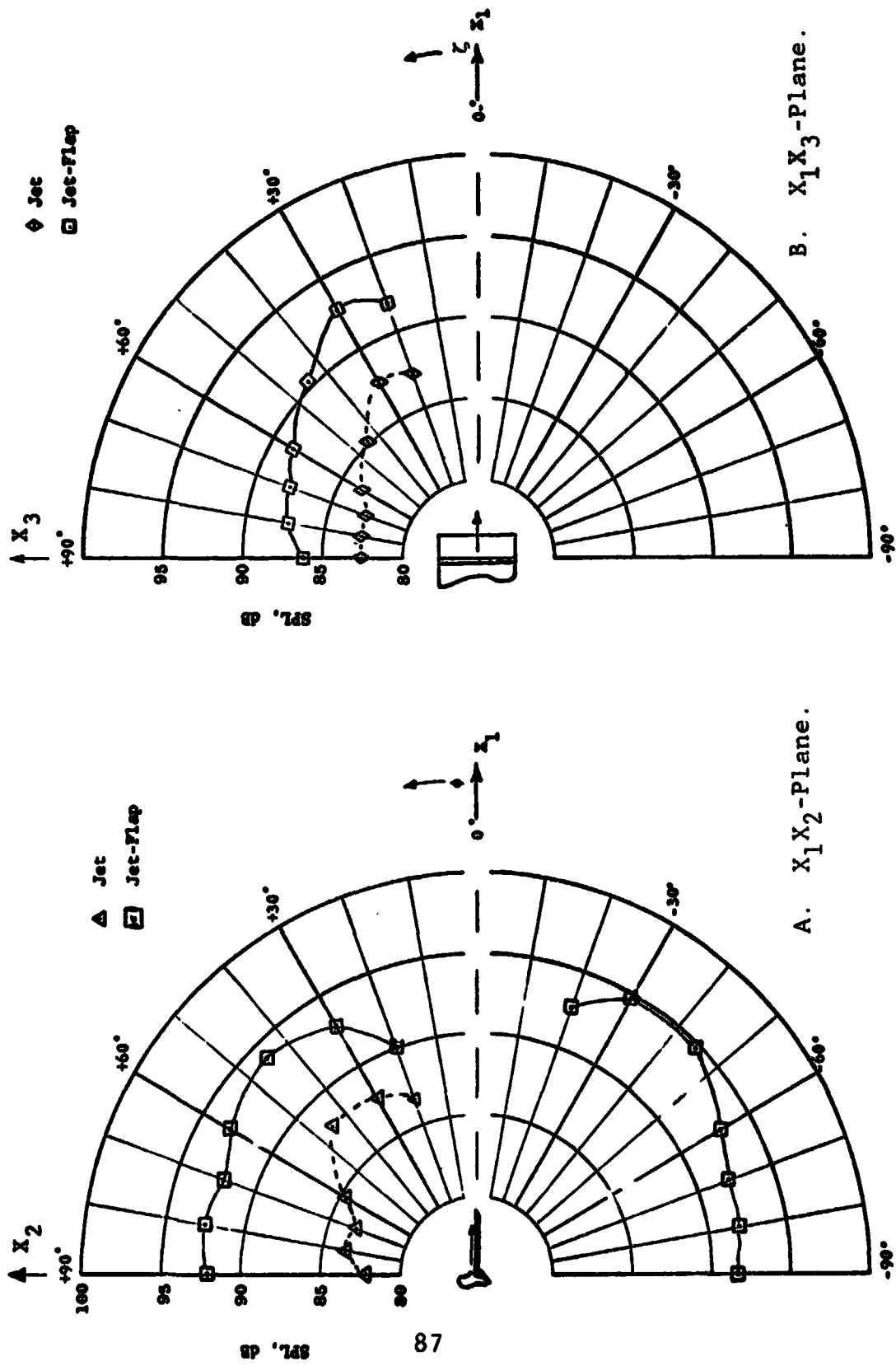


Figure 35. Sound Pressure Level Contours.

The minimum SPL which was measured for the jet occurs at $\phi = 90^\circ$, which is approximately 5 dB below the maximum value.

The addition of the flap to the slot-nozzle jet has a significant effect on the directivity and magnitude of the radiated sound. The SPL's for the jet-flap are much larger for all values of ϕ , and, as might be expected, the SPL contour of the jet-flap is not symmetric with respect to the X_1 -axis. The SPL's at $\phi = -20^\circ, -30^\circ, -45^\circ$ are larger than the corresponding positive ϕ -values; from 60° to 90° the SPL is approximately equal on both sides of the flap. The maximum value of the SPL's which was measured for the jet-flap occurred at $\phi = -45^\circ$, although the value at $\phi = -30^\circ$ was very nearly equal to the -45° -value.

Figure 35A shows that the largest increase in SPL above the SPL generated by the jet, occurs at $\phi = 90^\circ$ and equals about 10 dB.

The greatly increased SPL's and the modification of the directivity pattern caused by the addition of the flap suggest the presence of a fundamentally different acoustic phenomena than that found in free-jet flow. Hayden [14] has shown that the directivity pattern in the X_1X_2 -plane of the noise produced by a jet-flap is similar to that of a point dipole located at and diffracted by the flap trailing edge. Ffowcs Williams and Hall [15] have shown that the noise produced by turbulent eddies

very near the trailing edge have the same directivity pattern in the X_1X_2 -plane as the postulated point dipole of Hayden.

The contours of SPL in the X_1X_3 -plane (sideline plane) for the jet-flap and jet are presented in Figure 35B. The contours for the jet and jet-flap are symmetric with respect to the X_1 -axis in this plane, therefore only SPL's for $+\zeta$ -values are shown. The SPL's for the jet-flap are seen to be about 5 dB above those for the jet for all values of ζ . However, the directivity pattern of the noise produced by the jet-flap is similar in shape to that of the jet, suggesting that the radiation field of the jet-flap flow in the X_1X_3 -plane is not affected the presence of the flap. The contribution of the surface integral in Equation (2-14) is equal to zero, since $\cos \theta$ is zero in the plane of the flap (X_1X_3 -plane). The measured maximum SPL in the X_1X_3 -plane for the jet and jet-flap occurs at $\zeta = 30^\circ$. The maximum SPL's in the X_1X_3 -plane are slightly less (about 1 dB) than their counterparts in the X_1X_2 -plane, suggesting that only a small portion of the sound received at the 45° -microphones in the X_1X_2 -plane is contributed by the surface integral.

Lighthill [7] has shown that the far-field acoustic intensity of the noise which is radiated by a cold, subsonic jet, which is embedded in an unbounded ambient atmosphere,

at rest, varies approximately with the eighth power of the jet exit velocity. This result, which Lighthill deduced from a dimensional analysis of the solution [the volume integral in Equation (2-13)] to his inhomogeneous wave equation, has been well verified for a wide variety of jet flows.

Curle [10], generalizing Lighthill's theory to include solid surfaces in the flow field, derived an equation similar to Equation (2-14). Curle concluded from a dimensional analysis of the surface integral that the far-field acoustic intensity of the noise produced by pressure fluctuations at the solid surface should vary as the sixth power of the characteristic flow velocity, providing that the characteristic dimension of the solid surface is small compared with a typical acoustic wavelength.

The surface of the 3-inch flap used in this investigation does not satisfy Curle's compact surface criterion, since the acoustic wavelength based on the 5000 Hz peak frequency is 2.76 inches. For non-compact surfaces, Ffowcs Williams and Hall have argued that any dimensional analysis based solely on turbulence velocity and length scales is inadequate, since diffraction effects will strongly affect the far-field acoustic intensity. They concluded that the far-field intensity of the sound produced by turbulence very near the surface trailing

edge should vary as the fifth power of the characteristic flow velocity.

Figure 36 shows the variation of the far-field acoustic intensity with jet exit velocity for several microphone positions. For the slot-nozzle jet, the acoustic intensity measured by the 45°-microphone is very nearly proportional to the eighth power of the jet exit velocity. The addition of the flap caused the exponent of $(V_1)_e$ to be lowered, as shown by the -45°-microphone curve, indicating that a portion of the noise which is received at the -45°-microphone is produced by the interaction of the turbulence with the solid surface. The intensity measured at the +90°-microphone in the X_1X_2 -plane is proportional to $(V_1)_e$ raised to a power between 5 and 6, indicating that most of the sound received here is produced by the interaction of turbulence with the solid surface. Recall that the maximum change in intensity as a result of the addition of the flap occurred at the 90°-microphone positions in the X_1X_2 -plane.

One third octave spectra of the sound at $\phi = \pm 45^\circ$ in the flyover plane is displayed in Figure 37A. The peak frequency of the jet noise is 5000 Hz, so that the flow has a peak frequency Strouhal number of .155 based on the jet exit velocity and the slot-nozzle height. The spectrum indicates a broad distribution of acoustic

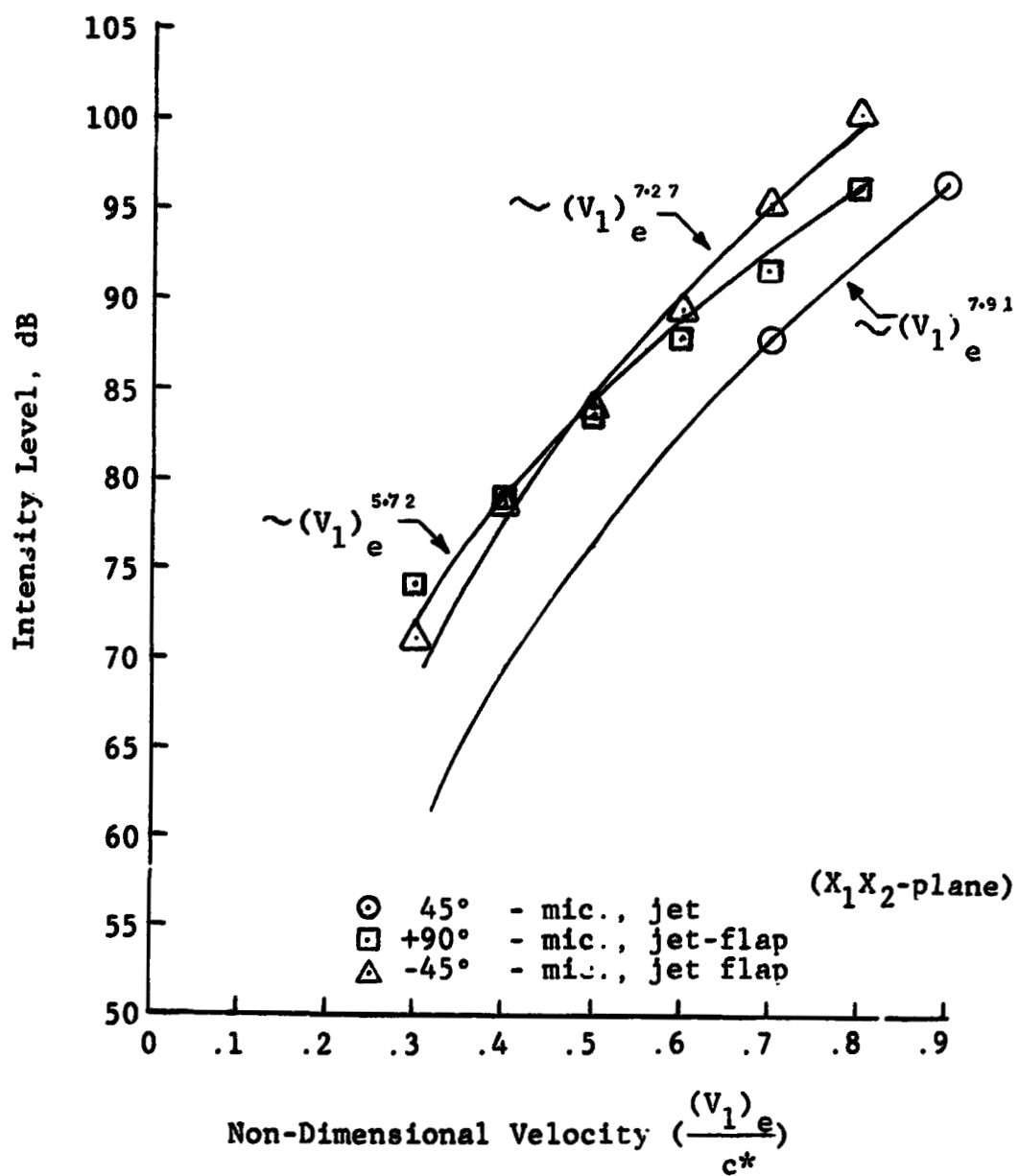


Figure 36. Intensity Level vs. Jet Exit Velocity

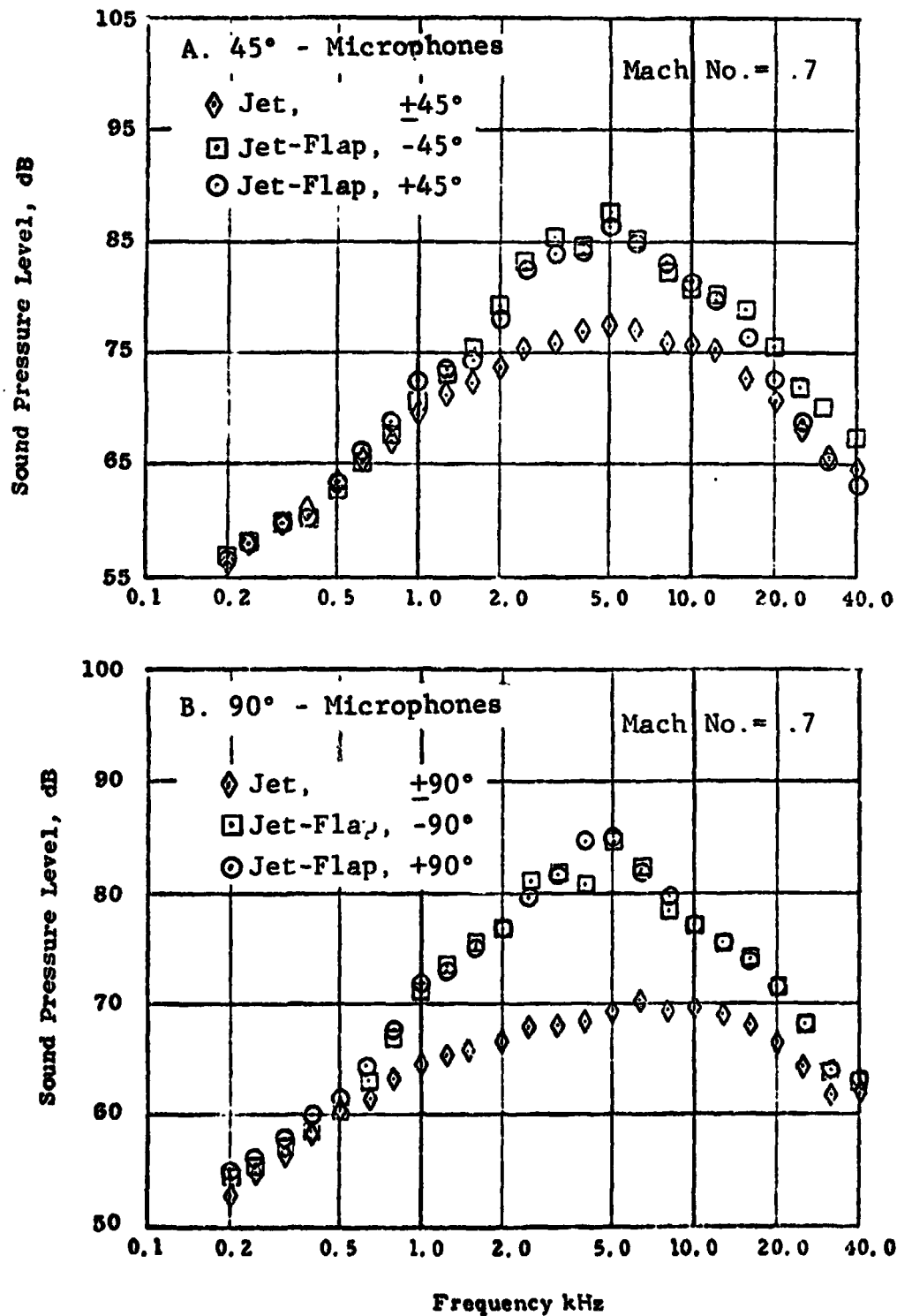


Figure 37. 1/3-Octave Spectra, X_1 - X_2 Plane.

energy. The 6 dB down-points (points where the SPL is 6 dB below its peak value) occur at about 1250 and 20,000 Hz. The addition of the flap causes a concentration of acoustic energy about the peak frequency of 5000 Hz, as evidenced by the 6 dB down-points at 2500 and 8000 Hz on the -45°-curve. For frequencies below 500 Hz, the spectrum for the -45°-microphone (below the flap) signal is almost identical to that of the +45°-microphone (above the flap). From 1250 Hz to 12500 Hz the SPL's of the +45°-spectrum are slightly higher than or equal to those of the -45°-spectrum. Above 12,500 Hz the +45°-spectrum is significantly lower than the -45°-spectrum, indicating that the primary mixing region may act as a shield for the high frequency noise which is produced in the secondary mixing region.

One third octave spectra for the $\pm 90^\circ$ -microphones in the flyover plane are displayed in Figure 37B. The spectrum of the noise produced by the jet indicates a broader distribution of acoustic energy than that of the noise measured at the 45°-microphone; the 6 dB down-points occur approximately at 1000 and 25,000 Hz. The addition of the flap affects the spectrum in the same manner as it did for the 45°-spectra; the acoustic energy is concentrated about the 5000 Hz peak frequency. The -90°-spectrum has slightly lower values than the +90°-spectrum below 1000 Hz, but above 1000 Hz the two spectra

are quite similar with the exception of their values at 4000 Hz.

One third octave spectra for the 30°-microphone in the X_1X_3 -plane are shown in Figure 38A. The spectrum for the jet is shifted to the left relative to the jet spectra in the X_1X_2 -plane, shown in Figure 37, indicating a larger share of the acoustic energy is found at the lower frequencies. This is believed to be the result of high frequency attenuation of the sound which travels across the span of the jet to the 30°-microphone. The 6 dB down points occur around 800 and 8000 Hz. The highest value of SPL occur at approximately half the peak frequency of the jet spectra in the X_1X_2 -plane. The spectra for the jet-flap shows the same concentration of energy about the peak frequency as was seen in the spectra taken in the X_1X_2 -plane.

3. ACOUSTIC SOURCE DISTRIBUTION ON THE FLAP SURFACE

In this section an attempt is made to evaluate the contribution of the surface integral in Equation (2-21) to the far-field sound received at the $\pm 45^\circ$ -microphones. The surface integrand, $R_{p,p}(-\tau_0)$, is evaluated by cross-correlating the signals from two microphones which are embedded in the flap surface with far-field microphones at $+45^\circ$ or -45° , as described in Chapters II and III.

Figure 38B shows the 1/3-octave spectra for the embedded microphones. Microphone 1 is one inch from the nozzle exit plane; microphone 2 is 2.5 inches from the nozzle exit plane and .5 inches from the flap trailing edge. It was shown in Chapter IV that the potential core of the jet extends to the trailing edge of the flap; therefore, the signals of the embedded microphones are expected to represent the fluctuating pressure in the potential core directly above the flap, and the turbulent boundary layer on the flap surface. The fluctuating pressures on the flap surface are a superposition of the pressure fluctuations of the turbulent flow field itself and those of the acoustic near-field associated with the noise produced by the turbulence.

The spectrum for microphone #1 is narrow-band, with the 6 dB down-points occurring at approximately 4000 Hz and 8000 Hz. The spectrum for microphone #2 shows a broader bandwidth and higher SPL's than the first microphone position. Note that the 6 dB down-points occur approximately 3000 Hz to the right and left of the 5000 Hz peak frequency. The broader spectrum and higher SPL levels measured at the second microphone position probably result because the potential core is very thin at this location and the pressure field is more strongly affected by the broadband turbulence fluctuations in the primary mixing region.

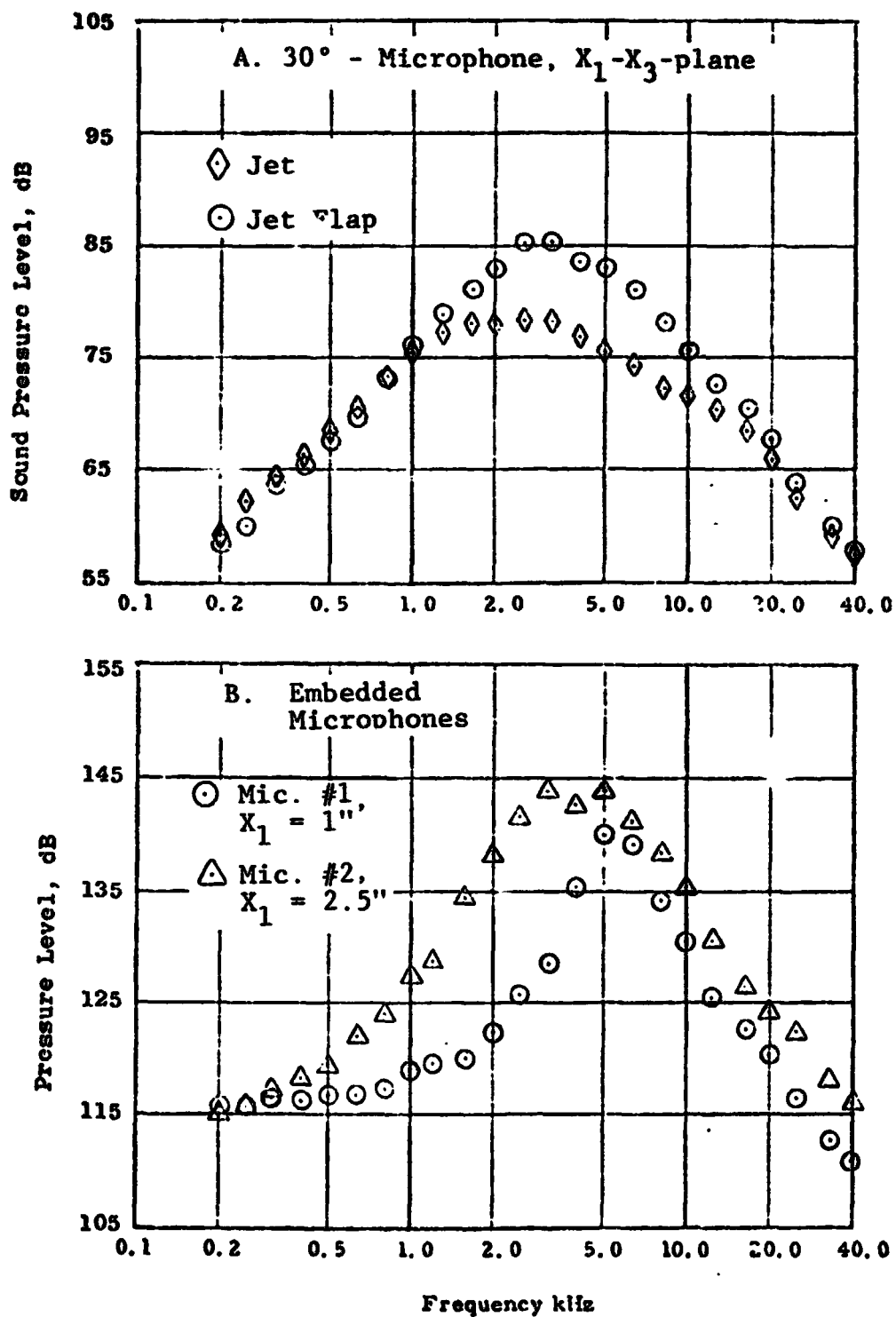


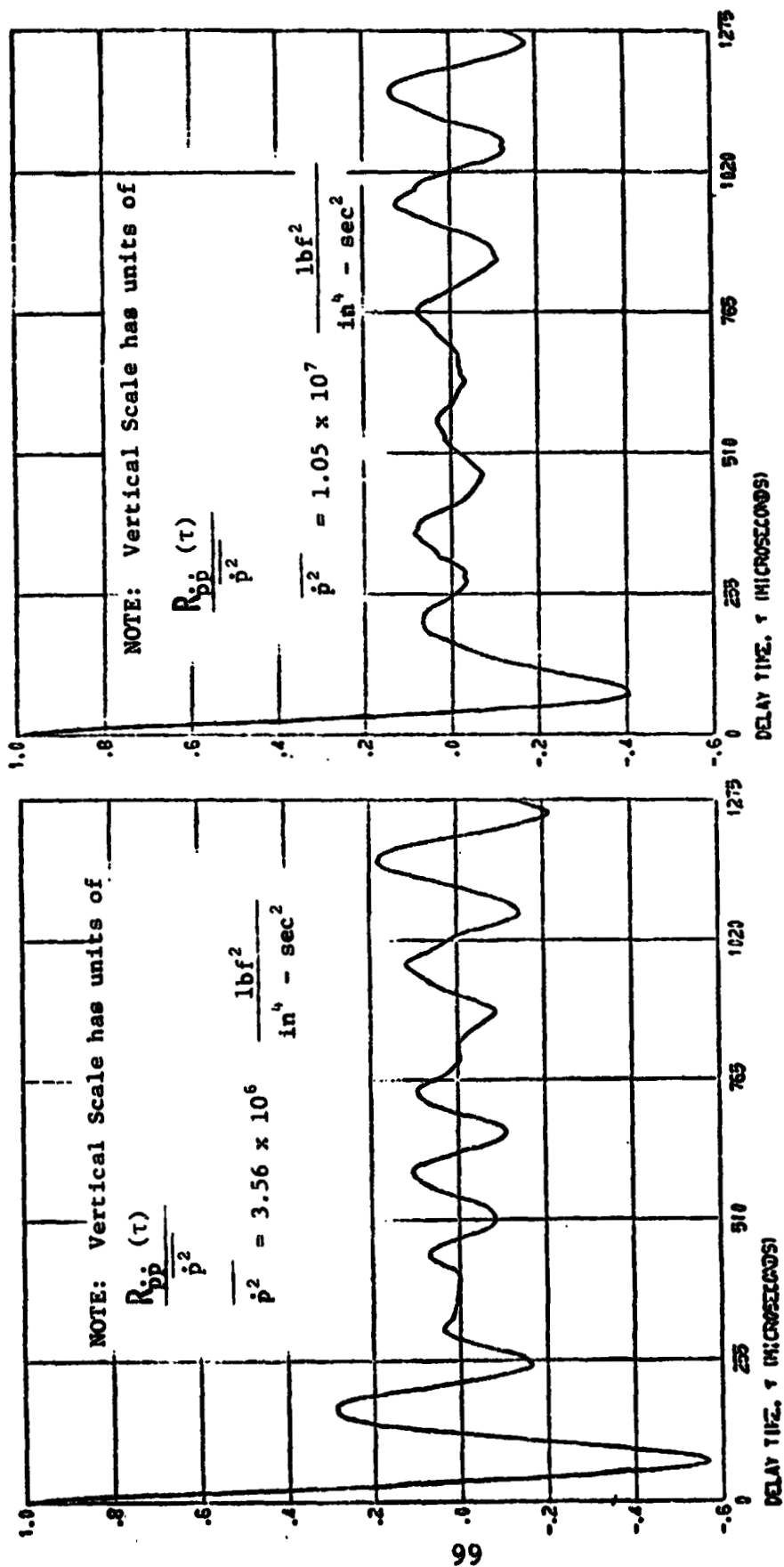
Figure 38. 1/3-Octave Spectra.

Figures 39A and 39B show the autocorrelation function of the time derivative of the signals from microphone 1 and 2 respectively. Both autocorrelation functions seem to indicate a low level periodic component of 5000 Hz buried in the narrow band random signals. Note that the autocorrelation function of the far-field microphones at $+45^\circ$ and -45° shown in Figure 40 also contain a periodic component at 5000 Hz. The embedded microphone signal was differentiated by the analog amplifier described in Chapter III. In the course of performing the cross-correlation analysis, an interesting relationship between p' and its time derivative was noticed:

$$(\dot{p}')_{\text{rms}} \approx 2\pi f_b (p')_{\text{rms}}$$

where f_b is the bandwidth of p' defined by the 6 dB down-points. A similar relationship was found to be true for m_x , which has a broadband spectrum. Therefore, it seems reasonable to suppose that this relationship may have validity for a large class of stationary random processes.

The time derivatives of the signals from the embedded microphones were cross-correlated with the two far-field microphones, located at $\pm 45^\circ$ in the X_1X_2 -plane. The cross-correlation function of the signals from the far-field microphone at $+45^\circ$ and the embedded microphone nearest the nozzle exit is shown in Figure 41A.



A. Embedded microphone 1

B. Embedded microphone 2

Figure 39. Autocorrelation Functions of Embedded Microphones.

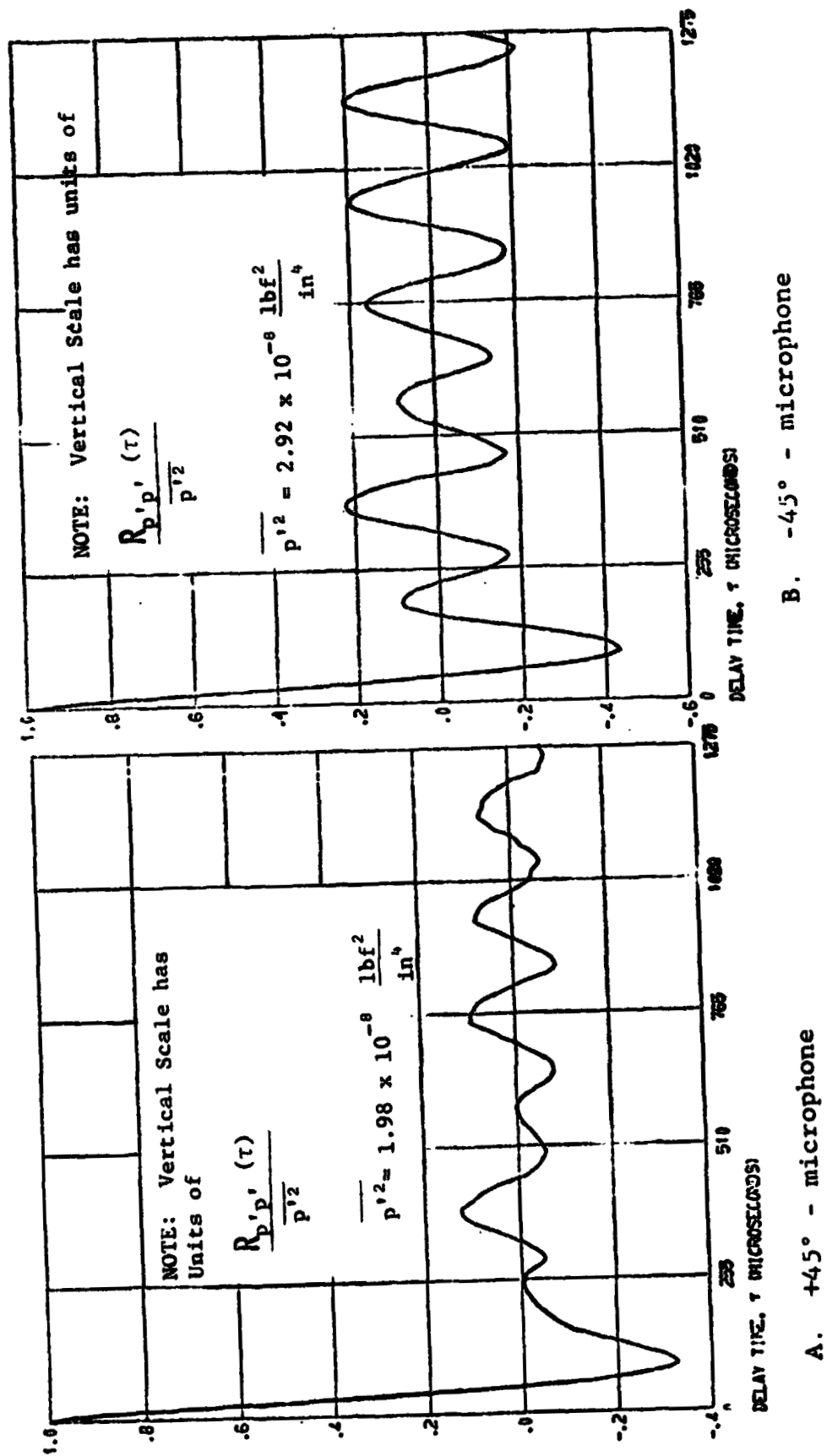


Figure 40. Autocorrelation Functions of the Far-Field Microphones.

It appears to be symmetric about $\tau = 12.25 \times 10^{-3}$ sec., where its maximum value occurs. On each side of the peak there are decaying wave envelopes, which are an indication of narrow bandwidth of the embedded microphone signal. The cross-correlation function of the signals from the second embedded microphone and the +45°-microphone (not shown) is similar in shape to the one shown in Figure 41A, with its maximum value occurring at $\tau = 11.97$ msec. Its maximum value is about twice as large as the maximum value of the cross-correlation function for the first embedded microphone.

The maximum value of the cross-correlation function is expected to occur at

$$\tau = \tau_0 = \frac{r}{c_0} = 11.32 \times 10^{-3} \text{ sec.}$$

However, in practice, the actual acoustic transmission time is seldom equal to τ_0 because part of the transmission path from a source point to an observer in the far-field is through an inhomogeneous media, i.e., the turbulent flow field of the jet. Furthermore, it is difficult to reliably measure the acoustic transmission time directly by inserting a mechanical source into the flow. Fortunately, the flow fluctuations in most turbulent jets are random functions of time. It can be shown that the cross-correlation function of these random fluctuations with the

sound they generate to the far-field has its maximum value at a value of τ corresponding to the acoustic transmission time. Then the integrands of Equation (2-21) are simply the maximum values of the associated cross-correlation functions. But if the flow field is not a random function of time, then there is no guarantee that an absolute maximum value will occur at the acoustic transmission time. Moreover, as the periodic waveform in the embedded microphone autocorrelations shown, the pressure field above the flap surface has a deterministic component.

There is evidence which indicates that the periodic waveform in the embedded microphone signal is caused by discrete flow disturbances which are convected with the flow. Fink [16], using an airfoil which was blown by a circular jet, cross-correlated the fluctuating pressure on the airfoil surface with a far-field microphone. He observed that the maximum value of the cross-correlation function occurred at a larger value of τ than the calculated acoustic transmission time, τ_0 . By moving the position of the embedded surface microphone toward the airfoil trailing edge, the value of τ at which the maximum value of the cross-correlation function occurs (τ_p) approached the calculated value, τ_0 . And by doubling the jet exit velocity, Fink found that the difference between the τ_p and τ_0 was halved. He concluded that turbulent eddies, whose pressure

fields are measured by the embedded microphone, were convected downstream and radiate when they interact with the trailing edge of the airfoil.

Joshi [17], using a jet-flap configuration similar to the one under investigation in this study, observed the same phenomena. He calculated the convection speed of the eddies to be about $.6 (V_1)_e$. In the present investigation, an estimation of the eddie convection speed was made by dividing the distance between the two embedded microphones, 1.5 inches, by the difference between the times where the peak values of $R_{p,p}(-\tau)$ occurred for the $+45^\circ$ -microphone. This gives a convection velocity of $.55 (V_1)_e$. Dividing the convection velocity by 5000 Hz (the frequency of the periodic component in the embedded microphone signals) gives a eddy spacing of 1.06 inches. It is believed that these eddies are convected in the turbulent boundary layer on the flap surface. The convected eddies apparently radiate very little sound while in the boundary layer, but near the flap trailing edge their contribution to the far-field sound is greatly amplified as predicted by the theoretical investigation of Ffowcs Williams and Hall [15]. Apparently these convected eddies are responsible for the 5000 Hz acoustic tone which is evident in the far-field microphone autocorrelation functions. Therefore the peak value of the cross-correlation function in

Figure 41A is not considered a legitimate contribution to the surface integral in Equation (2-21), since it does not represent an acoustic disturbance which is radiated from the flap surface at the position of the first embedded microphone. It is concluded that whatever noise is generated by the fluctuating pressure on the flap surface to the far-field microphone at +45° emanates from the region near the trailing edge.

An estimate of the surface contribution to the far-field sound at the +45°-microphone can be made by assuming that the value of $R_{p,p}(-\tau_o)$ on the last 1/2 inch of flap surface is equal to the peak value of the cross-correlation function for the second embedded microphone. The peak value of $R_{p,p}(-\tau)$ for the second embedded microphone is 2.114×10^{-9} lbf²/in⁶. If $R_{p,p}(-\tau_o)$ is assumed to be constant across the 3.9 inch span of the flow, then the estimate of the surface contribution to the +45°-microphone is given by:

$$(TSC)_{+45^\circ} = \frac{\cos 45^\circ}{4\pi c_o |x_1|} \int_A R_{pp}(-\tau_o) dA,$$

$$(TSC)_{+45^\circ} = \frac{\cos 45^\circ}{4\pi c_o |x_1|} (3.9) (.5) R_{pp}(-\tau_o),$$

$$(TSC)_{+45^\circ} = 4.16 \times 10^{-9} \frac{\text{lbf}^2}{\text{in}^4}$$

The mean square value of the sound, $\overline{p'^2}$, received at the far-field microphone at $+45^\circ$ is $19.8 \times 10^{-9} \text{ lbf}^2/\text{in}^4$. Dividing $(\text{TSC})_{+45^\circ}$ by $\overline{p'^2}$ indicates that about 21 percent of the far-field sound at the $+45^\circ$ -microphone might be generated from the last half-inch of the flap surface.

The cross-correlation function of the signals of the first embedded microphone and the far-field microphone at -45° is shown in Figure 41B. The maximum value occurs at 10.3×10^{-3} seconds, considerably earlier than the value of τ_0 . It does not appear to be symmetric about the maximum value. The vertical scales in Figure 41 have arbitrary units, but the magnitudes of both functions are directly comparable. The appearance of the bottom cross-correlation function suggests that there are two separate values of τ for which there is a high level correlation between the signals of the -45° -microphone and the first embedded microphone. The relative maximum which occurs near 12.5 milliseconds represents the eddy-convection effect, and does not contribute to the surface integral in Equation (2-21). The absolute maximum which occurs at 10.3 milliseconds is believed to result from the cross-correlation of noise, which is received at the embedded microphone and the far-field microphone from a strong acoustic source which is located in the flow, and, as such, is not a

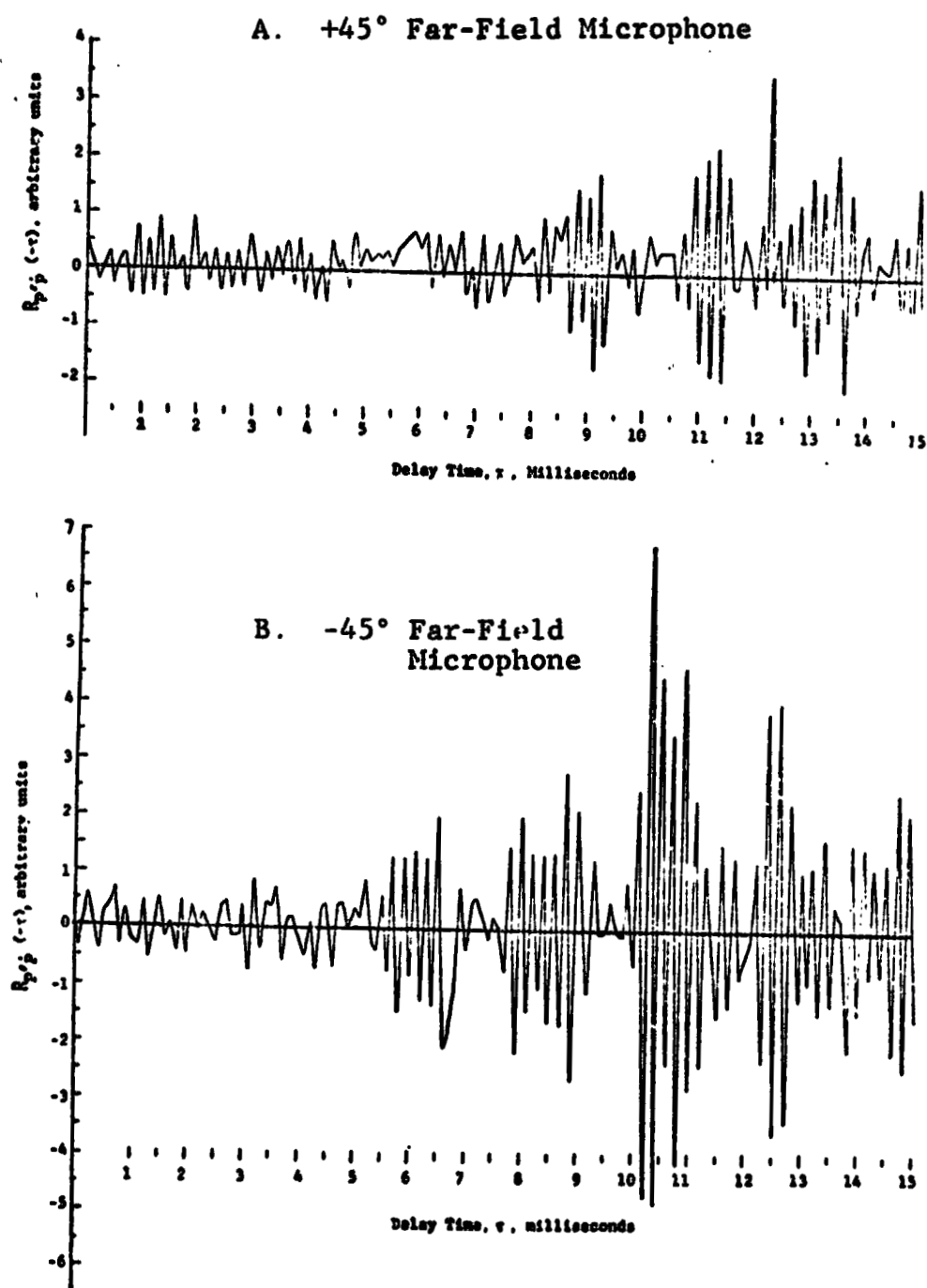


Figure 41. Cross Correlation of Embedded Microphone 1 and the Far-Field Microphones.

legitimate contribution to the surface integral. Recall that the contribution of diffraction and reflection of sound from sources in the flow to the fluctuating flap surface integral, and that the effects of reflection and diffraction on the far-field sound are included in the evaluation of $R_{p,p}(-\tau)$ at the proper delay time, τ_0 . Therefore it appears that only the pressure fluctuations on the flap surface near the trailing edge make a significant contribution to the far-field sound at the -45° -microphone.

Since both cross-correlation functions in Figure 41 use the same embedded microphone signal, it must be concluded that the peak which occurs at 10.3 milliseconds in the bottom figure, but is absent in the top figure, is caused by a strong noise source in the flow which radiates strongly to the -45° -microphone but not effectively to the $+45^\circ$ -microphone. In the next section it will be shown that the source of this noise is the secondary mixing region.

The cross-correlation function of the signals from the second embedded microphone and the far-field microphone is shown in Figure 42. The vertical scales in Figure 42 and 41 are the same, and the magnitudes of the cross-correlation functions may be directly compared. The maximum value of $R_{p,p}(-\tau)$ occurs at $\tau = 11.36$ milliseconds, very close to τ_0 ; the

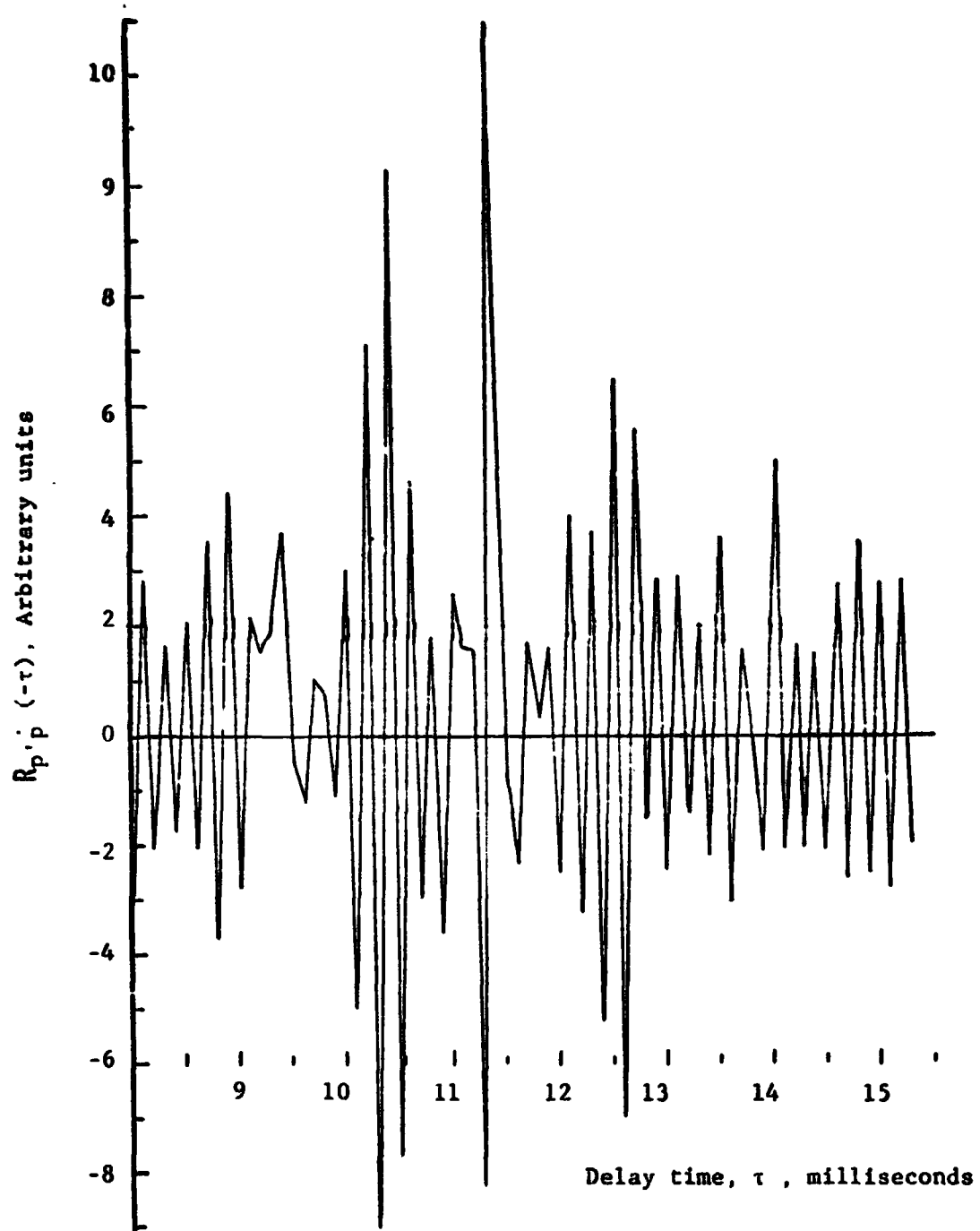


Figure 42. Cross Correlation of Embedded Microphone 2 and the Far-Field Microphone at -45° .

relative maximum which occurred at 10.3 milliseconds in Figure 41B is still in evidence and has a larger value. An estimate of the total surface contribution to the sound measured by the far-field microphone at -45° can be made by the same method used for the $+45^\circ$ -microphone. Then:

$$(\text{TSC})_{-45^\circ} = 8.98 \times 10^{-9} \frac{\text{lb} \cdot \text{f}^2}{\text{in}^6}.$$

Dividing this by the value of $\overline{p'^2}$ for the -45° -microphone indicates the estimated contribution of the surface integral is 30 percent.

4. ACOUSTIC SOURCE DISTRIBUTION IN THE FLOW FIELD

In this section the integrand of the volume integral in Equation (2-21) is evaluated for the $\pm 45^\circ$ -far-field microphones in the X_1X_2 -plane at selected positions in the flow field of the jet-flap by cross-correlating the processed signal of a hot-film probe with the appropriate far-field microphone signal. Details of this technique were given in Chapters II and III. The probe is positioned in the plane of transverse symmetry ($X_3 = 0$), so that the volume integrands are evaluated in the X_1X_2 -plane. At a chosen downstream position (X_1), the volume integrands are evaluated on the flow centerline ($X_2 = 0$) and at the

points of maximum turbulence intensity (X_{2-MTI}) in the primary and secondary mixing regions. The hot-film probe's axial position is confined to the first 20 slot-nozzle heights.

Figure 43 shows the relative magnitude of the rms values of fluctuating momentum, $\sqrt{m_x^2}$, in the flow field of the jet-flap, as measured by the inclined hot film probe. The reference level for the dB-scale is 2.08×10^{-8} lbm/sec. in². The term "+45°-probe" implies the probe orientation which allows the measurement of the momentum component in the direction of the +45°-microphone. That is, the normal to the probe sensor element makes an angle of +45° with the X_1 -axis. Similarly, the term "-45°-probe" implies the same for the -45°-microphone. So in the primary mixing region, the +45°-probe measures the momentum fluctuations in the direction of the ambient atmosphere, but the -45°-probe measures momentum fluctuations toward the jet centerline. In the secondary mixing region the reverse is true; i.e., the -45°-probe measures the momentum fluctuations toward ambient atmosphere and the +45°-probe measures the fluctuations toward the jet centerline.

The large differences in $\sqrt{m_x^2}$ measured at the same points in the flow, using the +45° and -45°-probes,

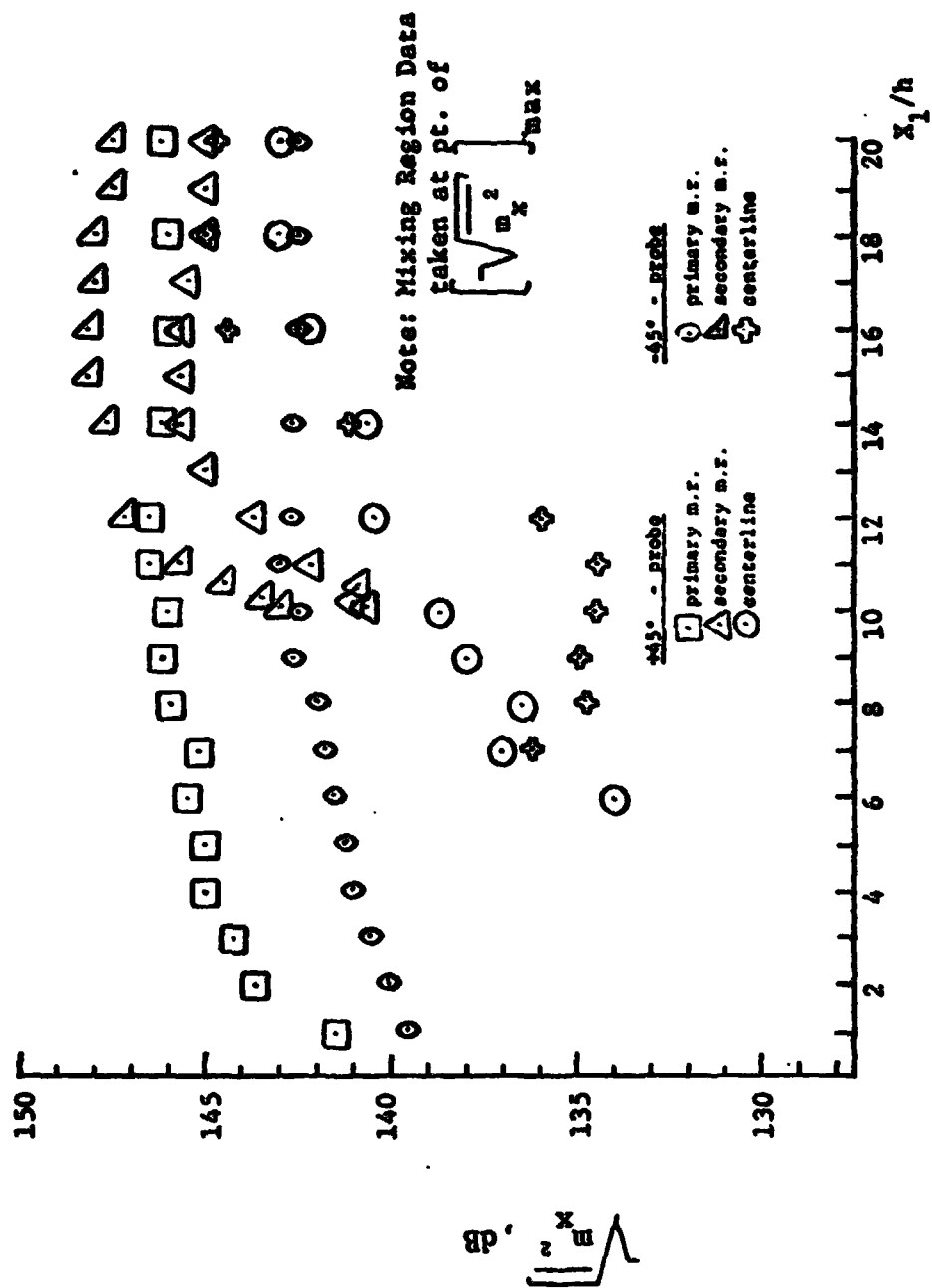


Figure 43. Variation of $\sqrt{u_x^2}$ with Downstream Distance for the Jet-Flap at Mach = 7.

indicate a high level of anisotropy in the jet-flap flow field. There is about a 5 dB difference between the value of $\sqrt{m_x^2}$, as measured by the +45° and -45°-probes, almost everywhere in the primary mixing region; indicating that the momentum fluctuations have a preferred direction toward the ambient atmosphere. This is also evident in the measurements taken in the secondary mixing region; the values of $\sqrt{m_x^2}$ measured by the -45°-probe are about 2.5 dB higher than those measured by the +45°-probe. The same phenomena was observed for the jet without the flap, but the values measured in the jet mixing region are not displayed since they are coincident with the jet-flap values in the primary mixing region. The measurements of $\sqrt{m_x^2}$ on the flow centerline (X_1 -axis) show that the values measured above the flap surface with the +45°-probe are larger than those measured with the -45°-probe. However, aft of the trailing edge the values measured with the -45°-probe begin to increase and become equal to the values measured by the +45°-probe at approximately $X_1/h = 13$. Farther downstream the values measured by the -45°-probe are larger.

Figure 44 shows one third octave spectra for the -45° and +45°-probe at various positions in the jet-flap flow field. The spectrum of $\sqrt{m_x^2}$ at $X_1/h = 8$ is

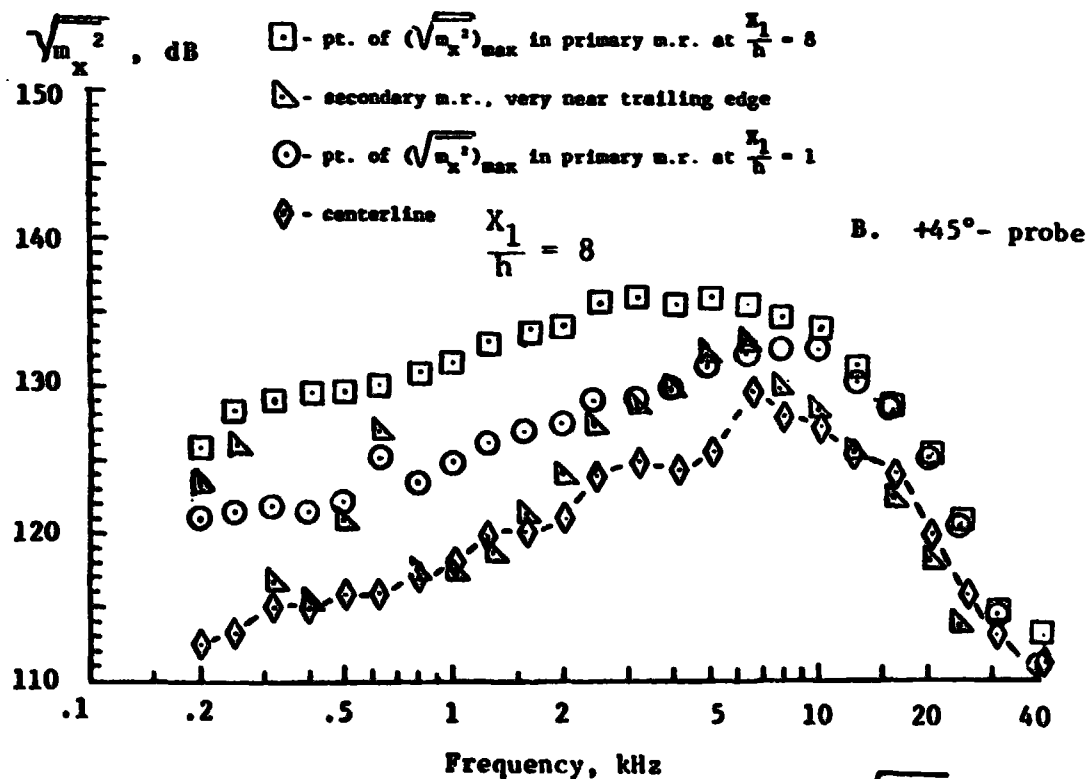
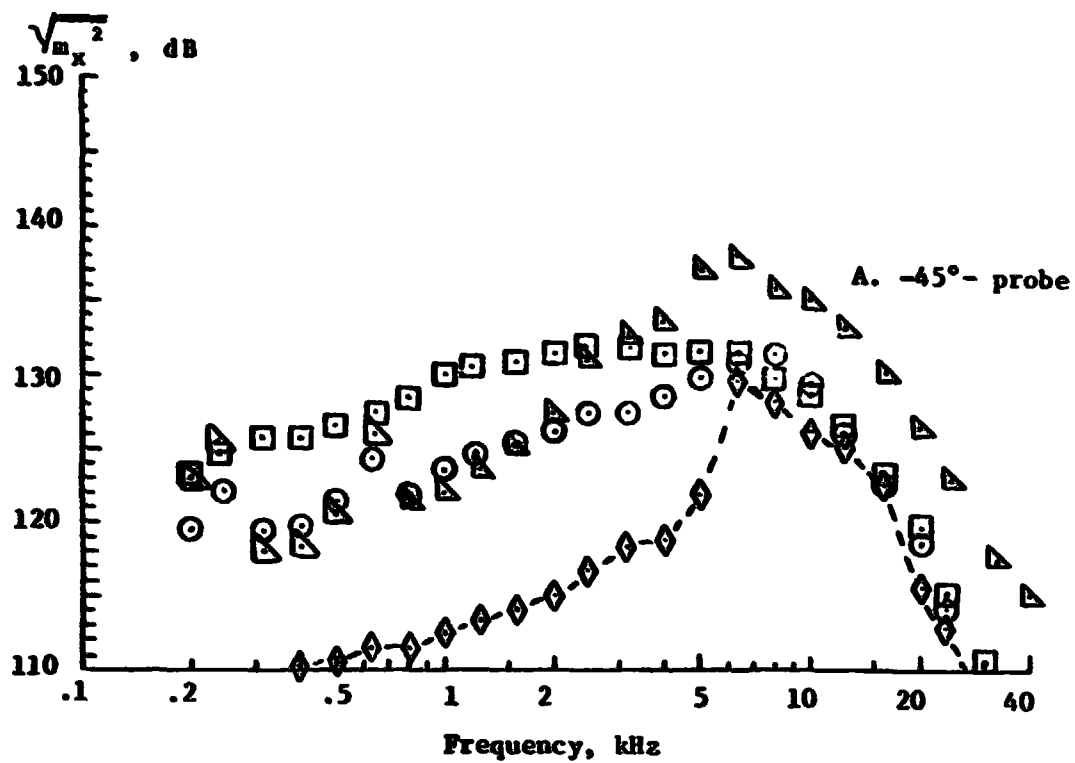


Figure 44. One Third Octave Spectra of $\sqrt{m_x^2}$

extremely broad and does not have a well-defined peak frequency. Comparison of the $X_1/h = 8$ spectrum of the $+45^\circ$ and -45° -probe indicates that the higher value of $\sqrt{m_x^2}$ measured by the $+45^\circ$ -probe is from contributions over the entire frequency range. The spectrum of $\sqrt{m_x^2}$ at $X_1/h = 1$, as measured by the $+45^\circ$ -probe, has its maximum value at 10 kHz. The 6 dB down-points occur at approximately 2 and 17 kHz. The spectrum of $\sqrt{m_x^2}$, measured by the -45° -probe at the same point, indicates generally smaller values over the entire frequency range. The peak value of the spectrum is at 8 kHz and the 6 dB down-points occur at approximately 1.25 and 12.5 kHz.

Near the flap trailing edge, the largest value of $\sqrt{m_x^2}$ is measured by the -45° -probe. The peak frequency of $\sqrt{m_x^2}$ at the trailing edge is 6.3 kHz, and the 6 dB down-points are approximately 2.5 and 15 kHz for the -45° -probe and 2.5 and 10 kHz for the $+45^\circ$ -probe. The low-frequency peaks in the spectra made at the trailing edge and at $X_1/h = 1$ are believed to be caused by the vibration of the probe holder in these high-shear regions. The low levels of $\sqrt{m_x^2}$ on the flow centerline result from the smaller values of the low-frequency components. A comparison of the $+45^\circ$ and -45° -probe spectra suggests that the eddy structure associated with low frequency components is highly anisotropic there.

Figure 45A and 45B shows representative autocorrelation functions of m_x and \ddot{m}_x respectively. The autocorrelation of m_x is typical of a broadband random quantity.

For a stationary random quantity, Z' , Tennekes and Lumley [18] have shown that the power spectral density of $\partial^2 Z' / \partial t^2$ is given by:

$$(\omega)^4 S(\omega),$$

where

$$\omega = 2\pi f$$

$$S(\omega) = \text{power spectral density of } Z'.$$

Therefore for a broadband signal such as m_x , most of the contributions to $\partial^2 m_x / \partial t^2$ will come from frequencies above 10 kHz.

Figure 46 shows a typical pair of cross-correlation functions for the shear and self-noise components. These cross-correlation functions were obtained for the -45°-microphone with the hot-film probe located in the secondary mixing region, 5 slot-nozzle heights from the flap trailing edge. Both cross-correlation functions in Figure 46A have been normalized with respect to their peak values, therefore their magnitudes can not be directly compared. When expressed in physical units the peak value of the shear-noise cross-correlation function in Figure 46A is about ten times larger than the self-noise peak shown

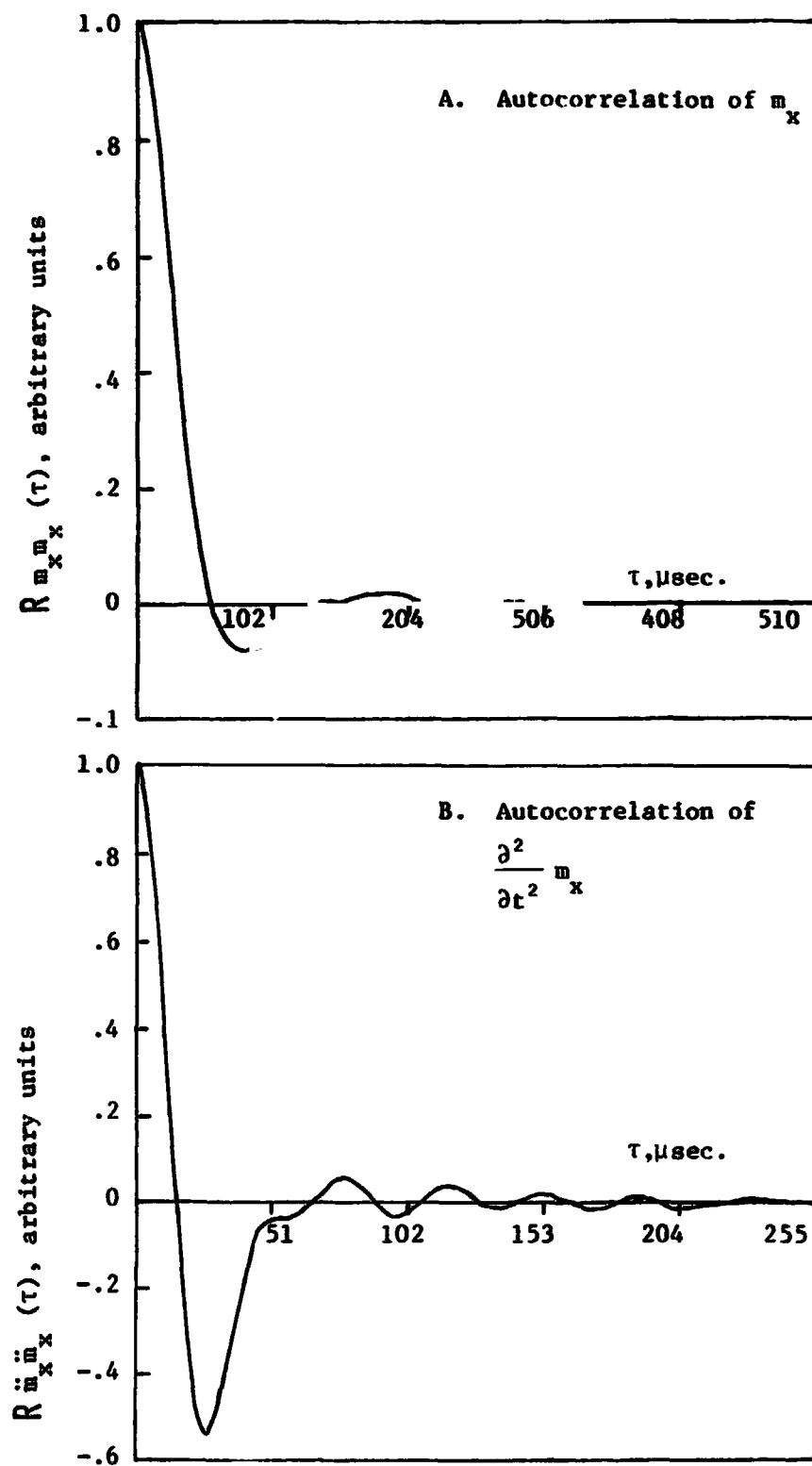


Figure 45. Turbulence Autocorrelation Functions ($X_1 = 7$; Primary M.R.).

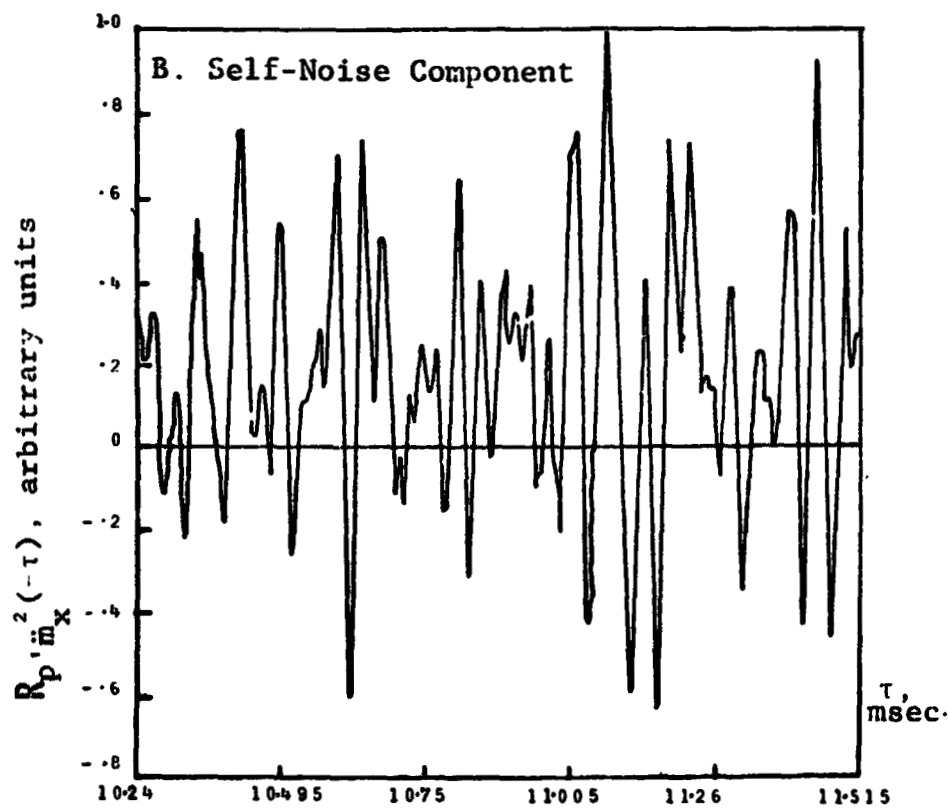
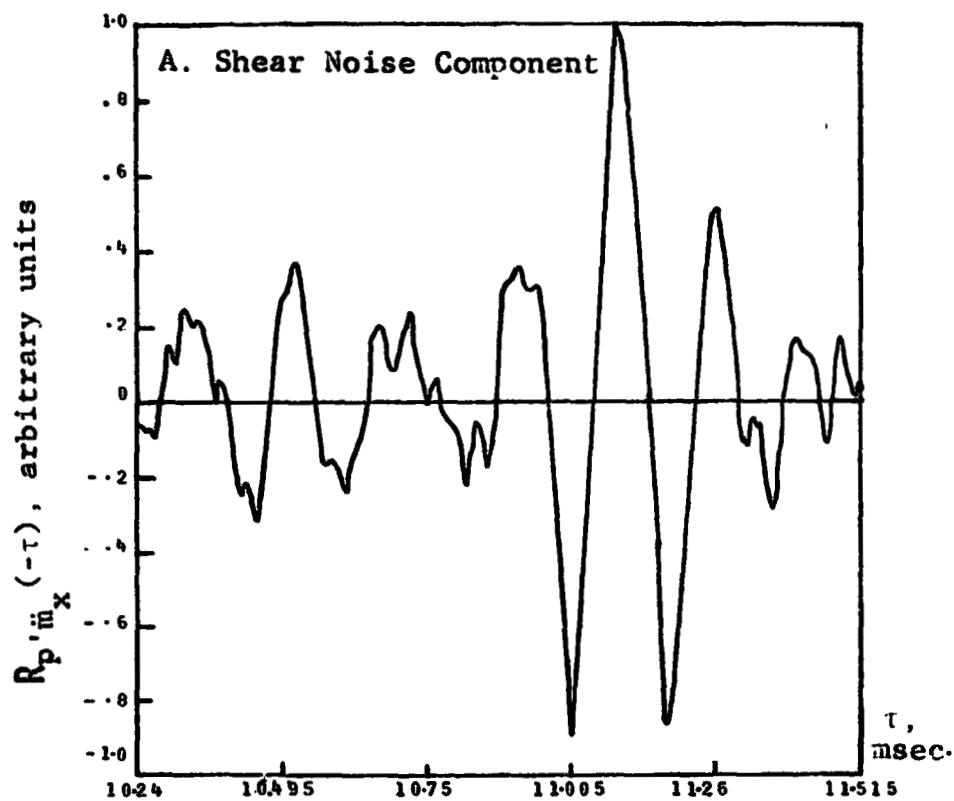


Figure 46. Shear and Self Noise Components ($X_1/h = 15$, Sec. Mix. Reg.).

below. The self-noise component was found to be at least an order of magnitude less than the shear-noise component at almost all points in the flow where a cross-correlation analysis was performed.

The delay time range, 10.24-11.515 milliseconds, represents the "window" of the F.S.C. correlator at a sampling period of 5 microseconds. The width of the window is given by the product of the sampling period and the number of memory bins available in the machine. The F.S.C. correlator has 256 memory bins. The window can be shifted on the τ -scale so that the cross-correlation function can be computed for the τ -range of interest. The cross-correlation functions for the surface microphones in Figure 41 are actually composites, made by connecting the several parts of the function which was computed in adjacent windows.

The acoustic source strength per unit volume is defined as:

$$v = \frac{1}{4\pi p_0 |x_1| \gamma} \left[2 \bar{M}_x R_p' \ddot{m}_x (-\tau_0) + R_p' \dot{m}_x^2 (-\tau_0) \right]$$

Figure 47 shows the axial acoustic source strength distribution in the jet-flap flow for the far-field microphone at $+45^\circ$. These values have been corrected for the error discussed in Appendix A. In the primary mixing region above the flap surface, the value of ∇ appears to remain relatively constant to $X_1/h = 7$. At $X_1/h = 8$, ∇ has a relative maximum and gradually decreases until $X_1/h = 10$, where ∇ again remains approximately constant to $X_1/h = 12$. From $X_1/h = 12$ to $X_1/h = 16$ there is a gradual increase in the value of ∇ , after which it begins a steady decay. The values of ∇ at $X_1/h = 2, 4, 6$ in the primary mixing region are not displayed, because the insertion of the hot-film probe holder caused the generation of a powerful acoustic tone which contaminated the cross-correlation function. The effect of extraneous noise generation (caused by the presence of the probe holder in the flow) on the measured cross-correlation functions is discussed in Appendix B. The values of ∇ on the flow centerline are significantly larger than those found in the primary mixing region. This result is quite interesting, considering the fact that there exists a remnant of the potential core above the flap surface, as was seen in Chapter IV. Actually the values of the shear component, $R_{p,m_x}(-\tau_0)$, have

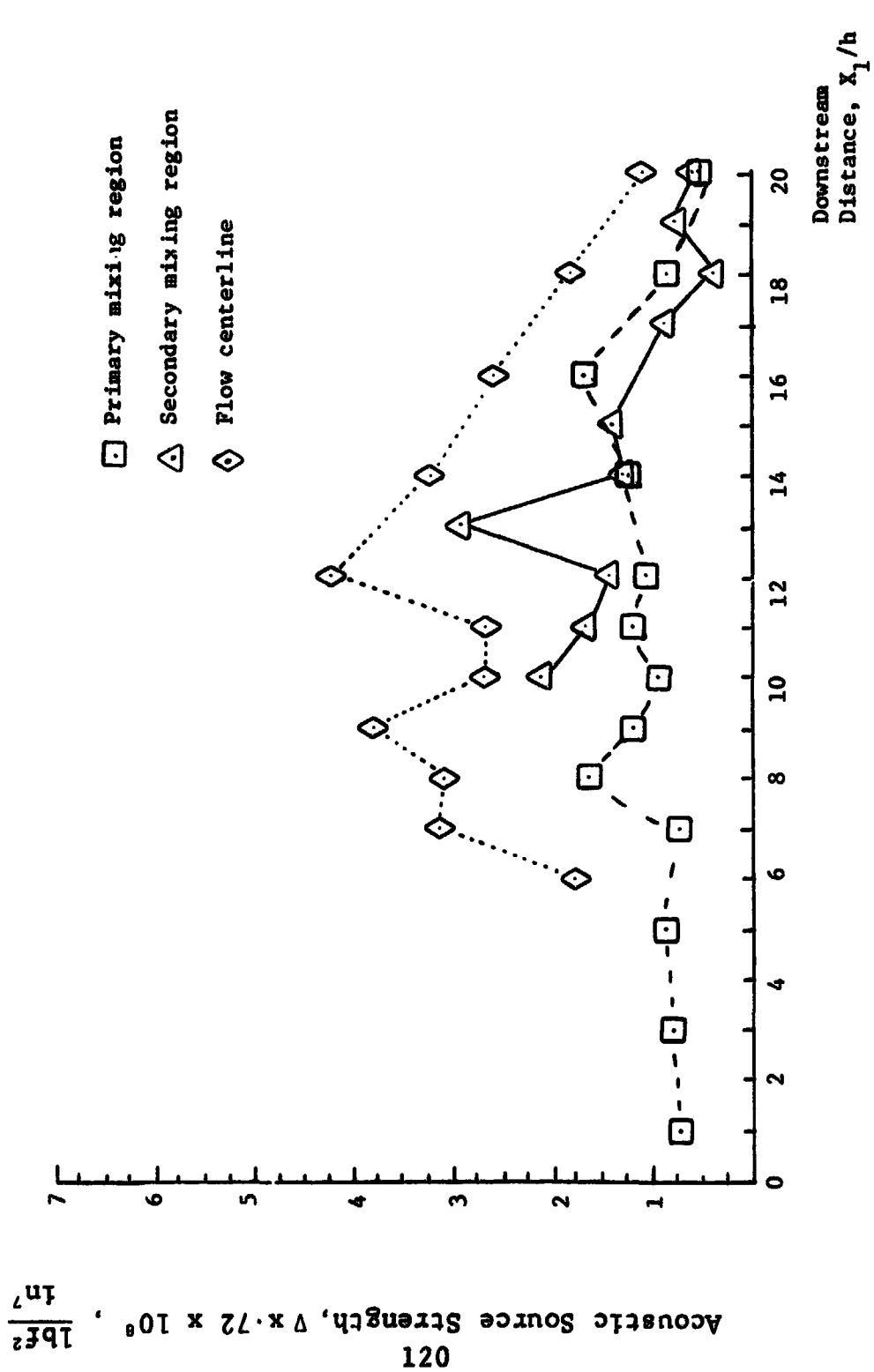


Figure 47. Axial Distribution of Acoustic Source Strength in the Jet-Flap Flow Field for the -45°-Microphone.

about the same value here as in the primary mixing region, but the fact that it is multiplied by the large value of \bar{M}_x on the centerline is responsible for the large values of ∇ . The centerline distribution increases steadily as the potential core becomes turbulent until a relative maximum is reached at $X_1/h = 9$. A sharp drop is seen at $X_1/h = 10$ and 11. The absolute maximum occurs at $X_1/h = 12$, after which a rapid roll-off occurs.

The distribution of ∇ in the secondary region shows a relative maximum near the flap trailing edge. The value of ∇ then decays until $X_1/h = 12$ where it appears to level-off, and at $X_1/h = 13$ the absolute maximum occurs. Recall from Chapter IV that the maximum values of the axial and transverse turbulence intensities rise sharply in the same region where ∇ decreases. The maximum value of ∇ in the secondary mixing region occurs near the point of maximum transverse turbulence intensity in the secondary mixing region. The value of ∇ drops to about the same as that in the primary mixing region at $X_1/h = 14$, and begins a steady decay with increasing downstream distance.

Figure 48 shows the axial acoustic source strength distribution of the jet-flap flow field for the far-field microphone at -45° . These values of ∇ have also been corrected for the hot-film measurement error discussed

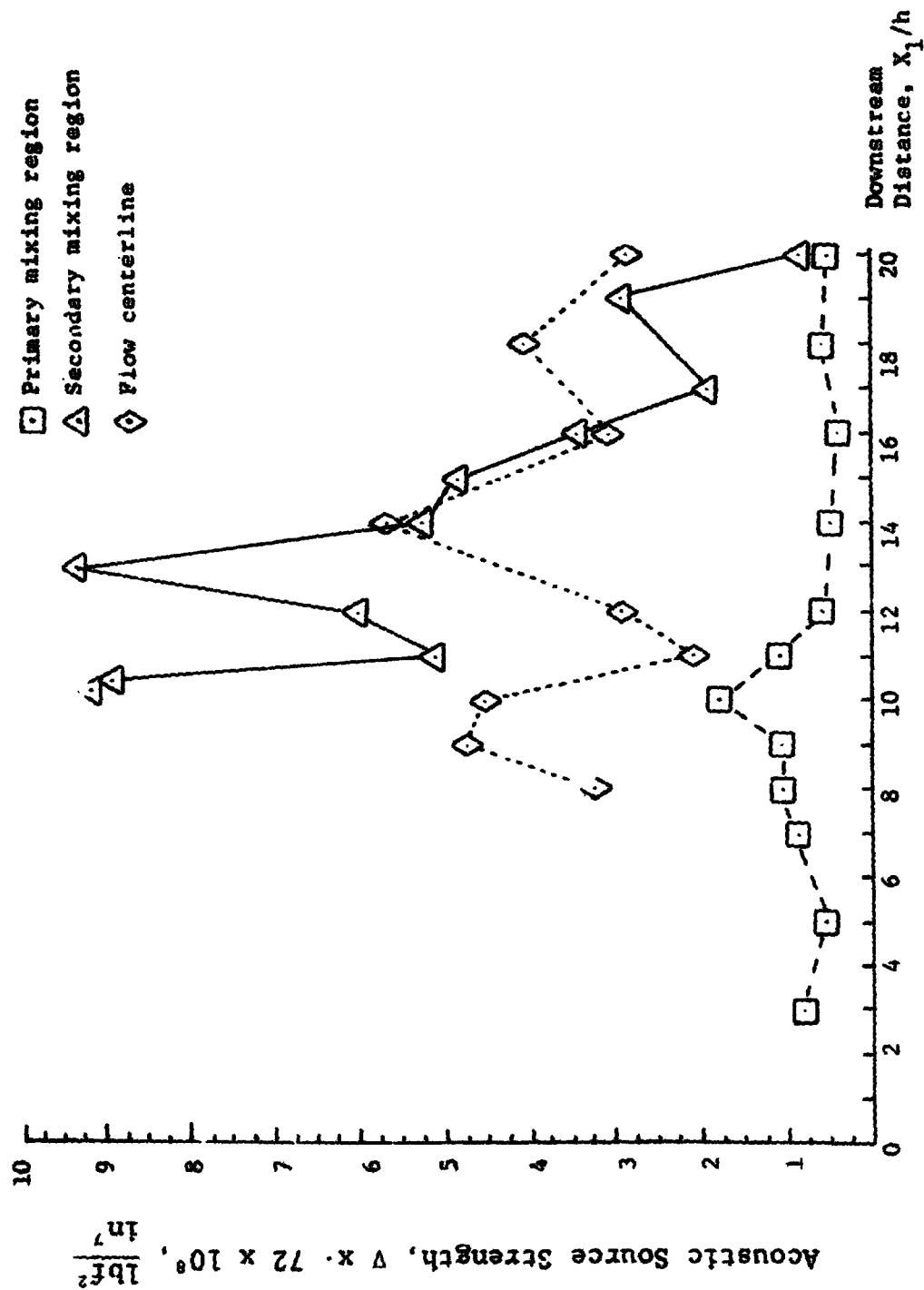


Figure 48. Axial Distribution of Acoustic Source Strength in the Jet-Flap Flow Field for the +45° - Microphone.

in Appendix A. The values of ∇ in the secondary mixing region are seen to be much larger here than in Figure 47 indicating that the sound which is generated in the secondary region is radiated much more effectively to the -45° -microphone than to the $+45^\circ$ -microphone. Also notice that the shape of the ∇ -distribution in the secondary mixing region is different for the two far-field microphones. The two peak values of ∇ are approximately equal for the -45° -microphones; whereas for the $+45^\circ$ -microphone, the maximum clearly occurs near the point of maximum transverse turbulence intensity in the secondary mixing region. As before, the value of ∇ drops sharply after its first maximum, where the axial and transverse turbulence intensities are rapidly rising. The relative maxima which occur close to the flap trailing edge are believed to be caused by the amplification effect of the edge, as predicted by the investigation of Ffowcs Williams and Hall [15]. It is important to note in Figure 48 that this amplification effect decreases rapidly with distance from the flap trailing edge. The relative minimum at $X_1/h = 11$ probably represents the downstream limit of the amplification effect, after which ∇ seems to rise with the increasing turbulence intensity of the secondary mixing region. Downstream of the maximum at $X_1/h = 13$, the value of ∇ in the secondary mixing

region drops very rapidly. The decay of V in the secondary mixing region is much more gradual for the $+45^\circ$ -microphone.

The values of V on the centerline are generally larger for the -45° -microphone than for the $+45^\circ$ -microphone. Of more importance is the fact that the centerline distribution of V decays much more rapidly for the $+45^\circ$ than for the -45° -microphone. It is also interesting to note the different occurrences of relative minima and maxima in the two centerline distributions. For example, the centerline distribution for the $+45^\circ$ -microphone has a relative maximum at $X_1/h = 12$, but the value of V there is comparatively low for the -45° -microphone.

The distribution of V in the primary mixing region above the flap for the -45° -microphone appears about the same as that for the $+45^\circ$ -microphone, indicating that the flap does not act as a shield for the noise which is generated in the primary mixing region above the flap. The maximum value of V in the primary region occurs above the flap trailing edge at $X_1/h = 10$, after which the value of V decreases until $X_1/h = 12$; the value of V then remains relatively constant until $X_1/h = 20$.

CHAPTER VI

SUMMARY AND CONCLUSIONS

An experimental investigation was performed in an attempt to establish the acoustic sources in a jet-flap configuration for two far-field microphones located 45° above and below the plane of the flap surface. The method employed for source location uses the causality principle in that a source fluctuation is related to the radiated sound by a cross-correlation method. The acoustic source strength distribution in the turbulent flow field was measured by cross-correlating a processed signal from an inclined hot-film anemometry probe with the signal from a far-field microphone. An estimate of the contribution made by the sources associated with the fluctuating pressure on the flap surface to the sound received at a far-field microphone was made by cross-correlating the processed signals of microphones embedded in the flap surface with the far-field microphone signals. In addition, detailed fluid dynamic measurements were made in the flow field of the jet-flap using dual-sensor hot-film anemometry probes and compared with those made in the flow field of the slot-nozzle jet without the flap. Profiles of the Reynold's stress and the axial and transverse mean

velocities and turbulence intensities were measured at various axial positions.

The fluid dynamic investigation indicated that the turbulence quantities which were measured in the primary mixing region above the flap surface differed little from those measured at the same axial position in the slot nozzle jet without the flap. An exception was the Reynold's stress profiles. The maximum values of the profiles in the primary mixing region above the flap had relatively high constant values, but the maximum values of the profiles for the slot-nozzle jet increased almost linearly with axial position until they reached approximately the same value observed in the primary mixing region. The presence of the flap extends the length of the potential core, since along the length of the flap, turbulent mixing occurs only above the flap surface.

Downstream of the flap trailing edge a secondary mixing region is formed, where high values of mean shear and turbulence intensity were found. The dynamics of the turbulence in the secondary mixing region were found to be different than those in the primary region. The maxima of the Reynold's stress and axial and transverse turbulence intensity profiles indicated that, whereas the maximum values of the measured turbulence quantities increased gradually or remained constant with axial

position in the primary mixing region above the flap, their maximum values in the secondary region increased very rapidly over a relatively short axial distance to peak values much larger than the corresponding peak values in the primary region. After reaching their peak value, the maxima of the profiles of the turbulence quantities decayed very quickly, so that within a few slot-nozzle heights downstream, the values in the secondary and primary regions were approximately equal.

The largest values of all the measured turbulence quantities occurred in the secondary mixing region. That of the axial turbulence intensity was measured about 6 slot-nozzle heights downstream of the flap trailing edge, but the largest value of the transverse turbulence intensity occurred about 4 slot-nozzle heights downstream of the trailing edge. In contrast to the well-defined peak values of the transverse and axial turbulence intensities, the Reynold's stress had a plateau from about 1 to 6 slot-nozzle heights downstream of the flap trailing edge.

Measurements made in the primary mixing region aft of the flap trailing edge showed that the turbulence quantities there had relatively constant values to about 15 slot-heights downstream of the edge, after which a well-defined decay is established. Measurements made

with the single-sensor hot-film probes indicated that the turbulence structure in both mixing regions was highly anisotropic. It was also shown that the rms-value of the time derivative of a fluctuating turbulence quantity is proportional to the bandwidth of that quantity.

From the cross correlation experiments it was concluded that whatever contribution the fluctuating pressure on the flap surface makes to the sound received at the two far-field microphones must come from a portion of the flap surface very near the trailing edge. It was estimated that 21 percent of the mean square value of the acoustic pressure measured at the far-field microphone at 45° above the flap surface might be radiated by the last half inch of the flap surface. Similarly for the far-field microphone at 45° below the flap surface, the last half inch of the flap was estimated to radiate 30 percent of the mean square value of the sound which was measured there.

In the flow field, the correlation analysis showed that the acoustic sources in the secondary mixing region were strongly directional, radiating much more effectively to the -45° -microphone position than to the $+45^\circ$ -microphone. The acoustic source strength in the secondary mixing region had two relative maxima, one of which occurred very near the flap trailing edge and the other of which

occurred 3 slot-heights downstream of the flap trailing edge. For the $+45^\circ$ -microphone the highest value of acoustic source strength in the secondary region was measured at the second relative maxima, 3 slot-heights downstream of the flap trailing edge. But for the -45° microphone the two maxima in the secondary region had approximately the same value. The high values of the acoustic source strength very near the flap trailing edge occurred where the axial and transverse turbulence intensities and Reynold's stress had relatively low values. A rapid decrease in acoustic source strength occurred with downstream displacement from the edge, at the same place where the turbulence intensities and Reynold's stress were rapidly rising. This decrease continued until about one slot-height was reached, where the value of the acoustic source strength increased rapidly to its relative maximum 3 slot-heights downstream of the edge. It was concluded that the high values of acoustic source strength very near the flap trailing edge where low levels of turbulence were measured resulted from the edge-amplification effect predicted by the theoretical work of Ffowcs Williams and Hall [15]. The acoustic source strength maxima which occurred 3 slot-heights downstream of the edge, was located 2 slot-heights ahead of the position of peak axial turbulence intensity, but very

near that of the peak transverse turbulence intensity and at a point where a high level of correlation existed between the axial and transverse flow fluctuations.

The acoustic source strength distribution measured in the primary mixing region indicated that the presence of the flap does not act as a shield against the noise which is produced in the primary mixing region above its surface. Furthermore, it appears that out to about 12 slot-heights from the nozzle exit plane the acoustic sources in the primary region contribute almost equally to the sound received at both far-field microphones, however farther downstream the sources in the primary region appear to contribute more to the $+45^\circ$ -microphone.

High values of acoustic source strength for both far-field microphones were measured along the flow centerline. In fact, the highest value of acoustic source strength which was measured for the $+45^\circ$ -microphone occurs on the flow centerline, 2 slot-heights downstream of the flap trailing edge. The centerline acoustic source strength distribution which was measured for the -45° -microphone had slightly larger values than that measured for the $+45^\circ$ -microphone, and was seen to decay slower with downstream distance. The existence of strong acoustic sources on the flow centerline was also found by Seiner [5] for the circular jet.

Based upon the results of the present investigation, it seems reasonable to conclude that a large portion of the flyover noise which would be generated by an aircraft equipped with a USB device will come from the secondary mixing region. However, it may be possible to reduce the noise emission from the secondary mixing region by relatively easy modifications to the flap surface, since it has been shown by Yee [19] that the noise which is generated by the secondary mixing region is closely related to the turbulence structure in the boundary layer of the blown-surface. For example, using a jet-flap configuration similar to the one tested in the present investigation, Yee has shown that significant noise reductions can be achieved by roughening of the flap surface. The immediate effect of roughening is to increase the thickness of the turbulent boundary layer on the flap, which in turn reduces the value of mean shear in the secondary mixing region. The lower values of mean shear in the secondary region retard turbulence production, and hence decrease the turbulence intensity levels associated with high acoustic emission there. Also, the possibility that the changes in the turbulence structure of the boundary layer may reduce the edge amplification effect should not be overlooked. The

cross-correlation technique should be useful tool in determining the effect of flow field modifications on far-field sound generation.

BIBLIOGRAPHY

BIBLIOGRAPHY

1. Dorsch, R. G., E. A. Kresja and W. A. Olsen. "Blown Flap Noise Research," American Institute of Aeronautics Paper No. 71-745, June 1971.
2. Schrecker, G. O. "Turbulence and Aerodynamic Noise Characteristics of Jet Flap Type Exhaust Flows," Ph.D. Dissertation, The University of Tennessee Space Institute, Tullahoma, Tennessee, December 1972.
3. Grosche, F. R. "Zur Schallerzeugung durch einem turbulenten Luftstrahl über einer endlich grossen ebenen Platte," Mitteilungen aus dem Max-Planck-Institut für Stromungsforschung und der Aerodynamischen Versuchsanstalt, Selbstverlag Max-Planck-Institut für Stromungsforschung und Aerodynamische Versuchsanstalt, Göttingen, Nr. 45, 1969.
4. Lee, H. K. and H. S. Ribner. "Direct Correlation of Noise and Flow of a Jet," Journal of the Acoustical Society of America, Volume 52, Number 5, May 1972.
5. Seiner, J. "The Distribution of Jet Source Strength Intensity by Means of a Direct Correlation Technique," Ph.D. Dissertation, The Pennsylvania State University, August 1974.
6. Siddon, T. E. "Surface Dipole Strength by a Cross Correlation Method," Journal of the Acoustical Society of America, Volume 53, Number 2, February 1973.
7. Lighthill, M. J. "On Sound Generated Aerodynamically-I. General Theory," Proceedings of the Royal Society of London, Series A, Volume 211, May 1952.
8. Stratton, J. A. Electromagnetic Theory. New York: McGraw-Hill Book Company, Inc., 1941.
9. Fuchs, H. V. and A. Michalke. "Aerodynamic Noise Theory," Progress in Aerospace Sciences, Pergamon Press, Oxford, Volume 14, 1973.

10. Curle, S. N. "General Theory of Aerodynamic Sound," Noise and Acoustic Fatigue in Aeronautics. London: John Wiley and Sons Ltd., 1968.
11. Curle, S. N. "The Influence of Solid Boundaries Upon Aerodynamic Sound," Proceedings of the Royal Society of London, Series A, Volume 231, No. 1184, July 1955.
12. Lilley, G. M. "On the Noise from Air Jets," Aeronautical Research Council No. 20376, September 1958.
13. Shubauer, G. B. and C. M. Tchen. Turbulent Flow. Princeton, New Jersey: Princeton University Press, 1962.
14. Hayden, R. E. "Sound Generation by a Turbulent Wall Jet Flow Over a Trailing Edge," Master's Thesis, Prudue University, August 1969.
15. Ffowcs Williams, J. E., and L. H. Hall. "Aerodynamic Sound Generation by Turbulent Flow in the Vicinity of a Scattering Half Plane," Journal of Fluid Mechanics, Volume 40, Number 4, March 1970.
16. Fink, M. R. "Scrubbing Noise of Externally Blown Flaps," Progress in Astronautics and Aeronautics, Volume 45, March 1975.
17. Joshi, M. C. "Acoustic Investigation of Upper Surface Blown Flaps," Ph.D. Dissertation, The University of Tennessee Space Institute, Tullahoma, Tennessee, March 1977.
18. Tennekes, H. and Lumley, J. A First Course in Turbulence. Cambridge, Mass.: M.I.T. Press, 1972.
19. Yee, P. M. "An Experimental and Theoretical Investigation Concerning the Aeroacoustic Characteristics of the Rough Jet Flap," Master's Thesis, The University of Tennessee Space Institute, Tullahoma, Tennessee, December 1974.
20. Mojola, O. O. "A Hot-Wire Method for Three-Dimensional Shear Flows," DISA Information, Number 16 July 1974.

21. King, L. V. "On the Convection of Heat From Small Cylinders in a Stream of Fluid: Determination of Convection Constants of Small Platinum Wires with Application to Hot-Wire Anemometry," Phil. Trans. Royal Soc. London, A214, 1914.
22. Norman, B. "Hot-Wire Anemometer Calibration at High Subsonic Speeds," DISA Information, Number 5, June 1967.
23. Hinze, J. O. Turbulence, New York: McGraw-Hill Book Company, Inc., 1975.

APPENDICES

APPENDIX A

USE OF A HOT-FILM PROBE FOR THE MEASUREMENT OF M_x

A constant-temperature type hot-film probe consists of a very small cylindrical filament of quartz fiber which has been coated with an electrical conductor. The probe is connected to a control-box which contains electronic circuitry. The probe and control-box constitute the constant-temperature anemometer. The filament is heated by an electric current, and the electronic circuitry regulates the current so as to keep the filament resistance, and hence the filament temperature, at a constant selected value. When the probe is inserted into a flow, the amount of thermal energy carried away from the filament per unit time will equal the amount of electrical power supplied to it. The relationship between applied power and flow parameters can be found through calibration with known flows.

For a general 3-dimensional, incompressible, shear flow, Mojola [20] suggests a relationship as a modification of King's law [21]:

$$P = A + B \left| \vec{V}_{\text{eff}} \right|^{1/n}, \quad (\text{A-1})$$

where

P = instantaneous value of the power lost
by the probe filament,

$|\vec{V}_{eff}|$ = the magnitude of an effective cooling velocity vector at the probe filament,

and A, B, and n are constants for a given probe and flow. However, for subsonic compressible flows Norman [22] has shown that the power loss from the filament is a function of the specific momentum of the flow, so that Equation (A-1) is rewritten as:

$$P = A + B |\vec{M}_{eff}|^{1/n}, \quad (A-2)$$

where

$$|\vec{M}_{eff}| = \rho |\vec{V}_{eff}|$$

Equation (A-2) can be written in terms of voltage outputs from the anemometer, so that:

$$E^2 = E_o^2 + b |\vec{M}_{eff}|^{1/n}, \quad (A-3)$$

where

E = the instantaneous value of the anemometer output voltage,

E_o = the value of the anemometer output voltage when there is no flow over the filament

b = a constant for a given flow and probe.

The output voltage of anemometer, E , is a non-linear function of the effective momentum, as is evident from Equation (A-3). A linear relationship between voltage and effective momentum can be established using an electronic linearizer. The linearizer uses analog circuitry to compute the function

$$\begin{aligned}
 V_L &= \kappa (E^2 - E_0^2)^n \\
 &= \kappa \left[\left[b |\vec{M}_{eff}| \right]^{1/n} \right]^n .
 \end{aligned}$$

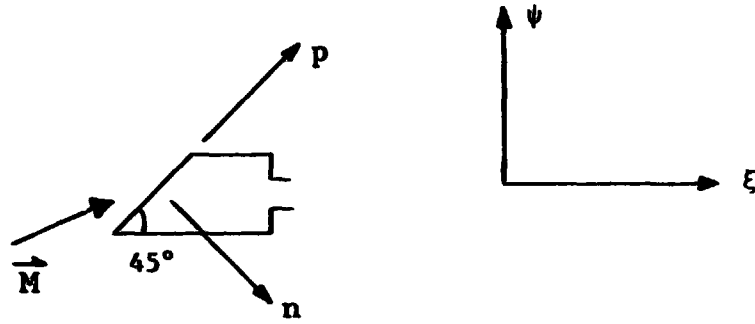
or

$$V_L = \beta |\vec{M}_{eff}| , \quad (A-4)$$

where,

- κ = a constant determined by the linearizer circuitry
- $\beta = \kappa b^n$, constant of proportionality determined by a calibration experiment with a known flow.

Consider a hot-film probe which is acted upon by an instantaneous momentum vector, \vec{M} , as shown in the figure below. Two orthogonal systems are shown, the $\xi\psi Z$ -system and the $\eta\phi Z$ -system. The $\eta\phi Z$ -system is attached to the probe sensor filament, and is inclined 45° to the ξ -axis. The Z axis is normal to the plane of the paper.



In the $\xi\psi Z$ -System \vec{M} is written as:

$$\vec{M} = M_\xi \vec{e}_\xi + M_\psi \vec{e}_\psi + M_Z \vec{e}_Z,$$

where

$\vec{e}_\xi, \vec{e}_\psi, \vec{e}_Z$ = unit vectors in the ξ, ψ, Z directions respectively.

M_ξ, M_ψ, M_Z = the momentum components in the ξ, ψ, Z directions respectively.

In terms of ξ - ψ - Z components, \vec{M} is expressed in the npZ -system as:

$$\begin{aligned} \vec{M} = & \cos 45^\circ \left[(\bar{M}_\xi + m_\xi) - (\bar{M}_\psi + m_\psi) \right] \vec{e}_n + \\ & \cos 45^\circ \left[(\bar{M}_\xi + m_\xi) + (\bar{M}_\psi + m_\psi) \right] \vec{e}_p \\ & + (\bar{M}_Z + m_Z) \vec{e}_Z, \end{aligned} \quad (A-5)$$

where,

$$M_{\xi} = (\bar{M}_{\xi} + m_{\xi}) ,$$

$$M_{\psi} = (\bar{M}_{\psi} + m_{\psi}) ,$$

$$M_Z = (\bar{M}_Z + m_Z) ,$$

M_{ξ}, M_{ψ}, M_Z = the mean value of M_{ξ}, M_{ψ}, M_Z ,
respectively,

m_{ξ}, m_{ψ}, m_Z = the deviation of the instantaneous
components from their mean values.

Equation (A-5) is more compactly written as:

$$\vec{M} = M_n \vec{e}_n + M_p \vec{e}_p + M_Z \vec{e}_Z , \quad (A-6)$$

where M_n and M_p , the momentum components normal and parallel
to the sensor axis respectively, are given by:

$$M_n = \cos 45^\circ \left[(\bar{M}_{\xi} + m_{\xi}) - (\bar{M}_{\psi} + m_{\psi}) \right] ,$$

$$M_p = \cos 45^\circ \left[(\bar{M}_{\xi} + m_{\xi}) + (\bar{M}_{\psi} + m_{\psi}) \right] .$$

Several incompressible-flow studies, including
Mojola [20] and Hinze [23], indicate that an effective
velocity vector can be expressed in terms of the
components of the actual velocity vector which are normal
and parallel to the sensor filament. It seems reasonable
to generalize this procedure in order to formulate an

expression for the effective momentum vector in terms of the p and n components; therefore,

$$\vec{M}_{\text{eff}} = M_n \vec{e}_n + M_z \vec{e}_z + \alpha M_p \vec{e}_p, \quad (\text{A-7})$$

where α is the direction-sensitivity constant which varies between .1 and .3, depending on the aspect ratio of the sensor filament and the filament material. The aspect ratio of the DISA R02 probe filament is 17.85, and it consists of a nickel film deposited on a quartz fiber. Siener [] has used a similar probe with a length - diameter ratio of 33, taking $\alpha = .23$. Since α is expected to increase with decreasing aspect ratios, α is estimated to be between .23 and .3 for the R02 probe.

The magnitude of \vec{M}_{eff} is given by:

$$|\vec{M}_{\text{eff}}| = \left\{ M_n^2 + (M_z + m_z)^2 + \alpha^2 \cos^2 45^\circ \left[(\bar{M}_\xi + m_\xi) + (\bar{M}_\psi + m_\psi) \right]^2 \right\}^{1/2}, \quad (\text{A-8})$$

For slot-nozzle jet flows the following estimates can be made: (taking \bar{M}_ξ as mean value of the axial momentum flux)

$$\frac{\bar{M}_\psi}{\bar{M}_\xi} \sim \frac{m_\xi}{\bar{M}_\xi} \sim \frac{m_\psi}{\bar{M}_\xi} \sim \frac{m_z}{\bar{M}_\xi} = 0 (\epsilon),$$

and

$$\frac{\bar{M}_z}{\bar{M}_\xi} = 0 (\epsilon^2) ,$$

where,

$$\epsilon \ll 1.$$

Using the above estimates Equation (A-8) can be expanded and reduced to:

$$|\vec{M}_{\text{eff}}| = M_n \left\{ \frac{1 + 2\epsilon^4 + 6\epsilon^2 + (\alpha^2)(1 + 11\epsilon^2 + 4\epsilon)}{(1 - 2\epsilon^2)} \right\}^{1/2} \quad (\text{A-9})$$

A reasonable estimate of ϵ can be made using the value of $\sqrt{\epsilon^2}$, which may be as high as .15 in the mixing regions of the jet-flap. Taking $\epsilon = .15$ and $\alpha = .25$, Equation (A-9) yields:

$$|\vec{M}_{\text{eff}}| \approx 1.12 M_n .$$

Therefore, this result indicates that if the assumption is made that the linearized hot-film response voltage is proportional to the momentum component normal to the sensor filament, then an error of about 12% will be generated for measurements in the highly turbulent regions of the jet.

That is, the measurements will indicate that \bar{M}_n and m_n are about 12% higher than their actual values, so that the measurement of M_x for the cross-correlation analysis will be correspondingly in error.

In order to correct the hot-film data which is used in the cross-correlation analysis a correction factor is introduced:

$$(CF)_p = \frac{\text{assumed measured quantity}}{\text{actual measured quantity}}$$

$$(CF)_p = \frac{\beta M_n}{\beta |\vec{M}_{eff}|} \frac{M_n}{1.12 M_n} \approx .893 \quad (A-10)$$

All of the hot-film data taken for the cross-correlation analysis will be multiplied by this factor. Of course the correction factor is a function of turbulence intensity, so that the use of (A-10) will over-compensate data taken in relatively low-turbulence regions. However, the upper limit of $(CF)_p$ is determined by the value of α . For $\alpha = .25$ and laminar flow the limiting value of $(CF)_p$ is .97. And since most of the data taken for the correlation analysis is at the points of maximum turbulence intensity in the jet's mixing region, the estimate of Equation (A-10) seems in order.

APPENDIX B

PROBE NOISE

Although the hot-film probe and its holder are quite small, their insertion into the flow caused considerable noise generation (probe noise). There were two distinct types of probe noise which were encountered during the experiment. A loud acoustic tone of 5000 Hz was generated when the probe holder was in the proximity of the flap trailing edge. It was shown in Chapter V that the fluctuating pressure above the flap surface has a periodic component of the same frequency. The presence of the probe holder near the trailing edge apparently creates an acoustic-feedback loop, so that the sound produced by the holder travels upstream and causes vortices to be shed from the nozzle lip at the same frequency. Evidence of this vortex structure is the presence of the periodic waveform in the autocorrelation function of m_x measured at $X_1/h = 4$ in the primary mixing region and shown in Figure 49. The period of the waveform is 205 microseconds, which corresponds to a frequency of approximately 5000 Hz. Compare this autocorrelation function with Figure 45A in Chapter V, which is the autocorrelation function of m_x in the primary mixing region when no tone is generated by the probe holder.

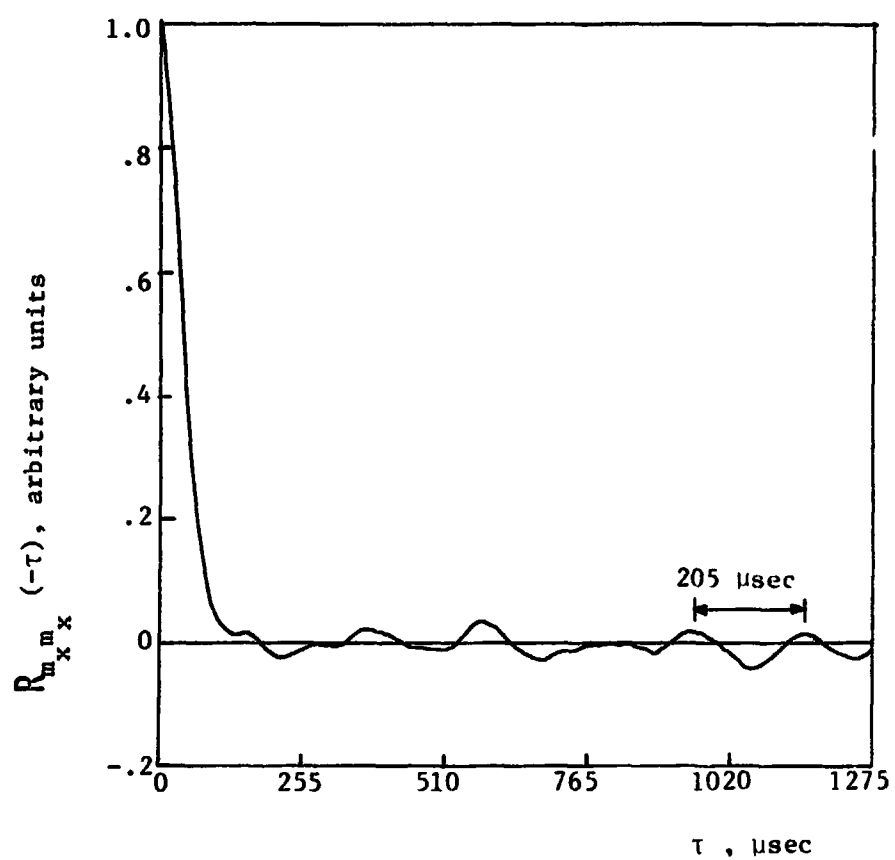


Figure 49. Autocorrelation Function of m_x at $X_1/h = 4$.

The presence of a large periodic component in both \ddot{m}_x and p' also makes their cross-correlation function periodic, without a well-defined peak value. Therefore, the cross-correlation function becomes extremely difficult to interpret under these conditions, and no values of the acoustic source strength are computed for $X_1/h = 1, 2, 4, 6$ for the -45° -microphone, and $X_1/h = 2, 4, 6$ for the $+45^\circ$ -microphone.

The insertion of the probe and probe holder at other points in the flow caused the generation of broadband noise. The intensity levels of probe noise which were received at the $+45^\circ$ and -45° -microphones are displayed in Figure 50. The dB-level for each scale is referenced to the value of $\overline{p'^2}$ measured by the respective microphone without the insertion of the probe in the flow. It was determined that the interaction of the flow field with the long stem of the probe holder (see Figure 14 in Chapter III) was responsible for this broadband noise generation.

In order to ascertain the effect of these high levels of extraneous noise on the measured cross-correlation functions, some experiments were performed at the U.T.S.I. aeroacoustics laboratory. In one experiment random noise generators and loud speakers were used to simulate the noise produced at a point in the flow and the noise

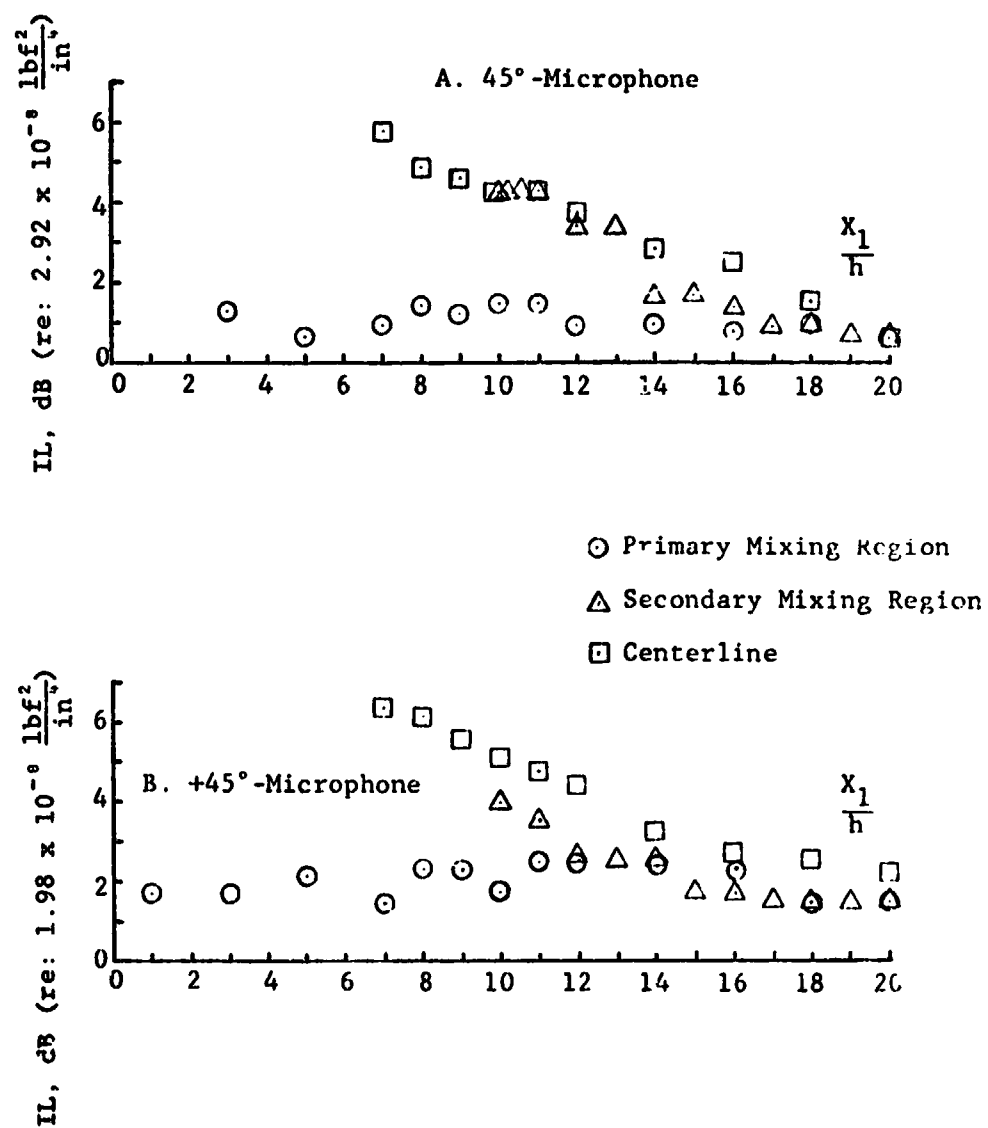


Figure 50. Probe Noise Intensity Levels.

generated by the stem of the probe holder. Figure 51 is a schematic of the test set-up. Each channel has its own random noise generator, power amplifier, and loudspeaker. The sound generated by the loudspeaker in Channel 1 simulates the noise which is radiated from a point in the flow. The voltage which drives the speaker is analogous to the anemometer output voltage. The sound generated by the loudspeaker in Channel 2 simulates the noise produced by the stem of the probe holder. A microphone is placed in the acoustic far-field of the speakers, and a cross-correlation between the voltage input to speaker #1 and the sound received at the far-field microphone is performed, with no extraneous noise being generated by Channel 2. Cross correlation of the input voltage of speaker #1 and the output of the far-field microphone is then conducted while extraneous noise is produced by Channel 2. Even when the SPL of the noise produced by Channel 2 was 12 dB higher than the noise produced by Channel 1, there was no change in the shape or magnitude of the cross-correlation function. Therefore, it is concluded that if the turbulence measured by the hot-film probe and the noise produced at the probe holder stem is random and independent (uncorrelated), there will be no effect on the cross-correlation function of the hot-film and far-field microphone signals.

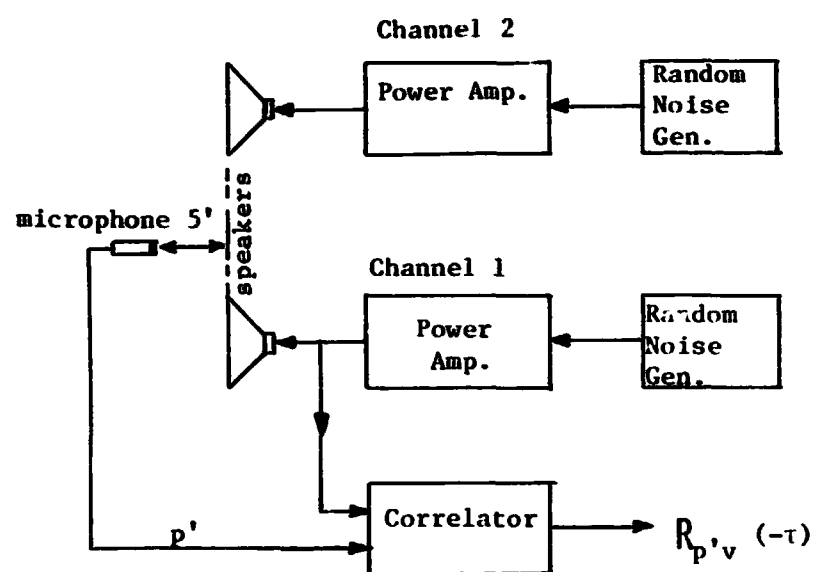


Figure 51. Test Schematic.

The noise produced at the probe holder stem is caused by the interaction of the surface with the local turbulent flow field. Therefore, if the turbulence at the hot-film probe position is uncorrelated with the turbulence at the probe holder stem, then the cross-correlation function should not be affected by the probe noise. In order to determine this, knowledge is required about the length a typical turbulent eddy travels before it loses its identity through interaction with other eddies in the flow. A relevant measurement to determine this length is the longitudinal space-time correlation of the turbulent flow fluctuations. This is accomplished by cross-correlating the signals of two hot-film probes, one of which is fixed at a point in the flow, and the other of which is displaced axially behind the stationary probe. This measurement has been carried out in the mixing region of low-speed round jets by several investigators (cf. Seiner [5]). They have shown that as the displacement between the probes increases, the peak of the cross-correlation function occurs at larger values of τ , and the amplitude of the peak decreases. For a 2-inch diameter circular jet with an exit Mach number of .3, Seiner found that with the hot-film probe displacement equal to 1.4 jet-diameters the peak value of the cross-correlation function was about 1/4 the value

of its maximum peak when the two probes are coincident. Therefore, it seems that the eddy lifetime is very brief. Recall that the probe holder stem is approximately 8 slot-nozzle heights downstream of the probe sensor element. Figure 52 shows the space-time correlation curves measured in the mixing region of the circular jet by Seiner.

Unfortunately, there seems to be no space-time correlation data available for slot nozzle jets similar to the one under investigation, so an attempt was made to measure the effect of probe noise on the measured cross-correlation functions in a more direct fashion at the U.T.S.I. aeroacoustics laboratory.

It was decided that a comparison between the cross-correlation functions of a hot-film signal and a far-field microphone signal measured with and without extraneous noise would be useful. However, since the analog differentiators were not available at U.T.S.I.; $R_{p', \ddot{m}_x}(-\tau_0)$ could not be measured directly. But it can be shown (see Lee and Riber [4] or Seiner [5]) that

$$R_{p', \ddot{m}_x}(-\tau_0) \propto \int_0^{\infty} f_0 S_{p', \ddot{m}_x}(-\tau) \left| \frac{d f_0}{d \tau} \right|_{\tau = \tau_0}$$

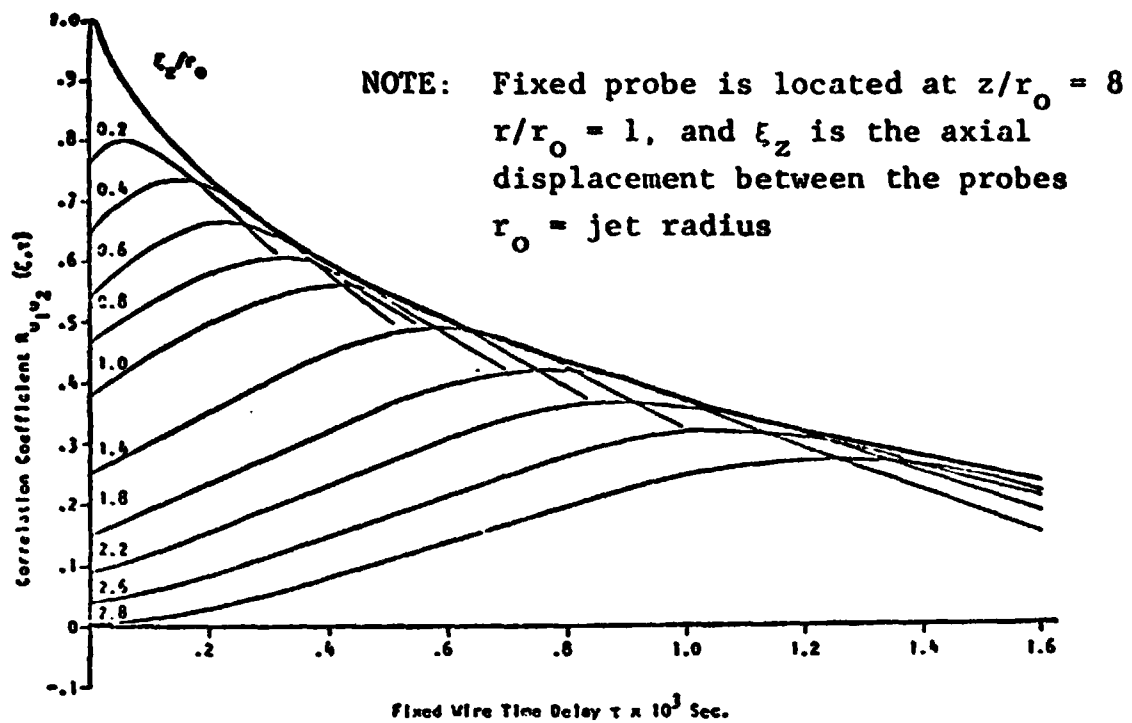


Figure 52. Space-time Correlation Curves for a Circular Jet (2-Inch Diameter; Exit Mach Number = .3).

Source: Seiner, J. M. "The Distribution of Jet Source Strength Intensity by Means of a Direct Correlation Technique," Ph.D. Dissertation, The Pennsylvania State University, 1974.

where

- f_o = the center frequency of an analog bandpass filter whose bandwidth is proportional to f_o .
- $S_{p'm_x}(-\tau)$ = the function obtained by cross correlating the outputs of two identical bandpass filters, with center frequency f_o , which have as their inputs p' and \ddot{m}_x , respectively.

Therefore, a number of cross-correlation functions were measured for the signals of m_x and p' , filtered at various center frequencies by B & K 1/3-octave filter sets.

A hot-film probe was carefully inserted into the shear layer of the slot-nozzle jet under investigation. The probe was placed 3 slot nozzle-heights downstream of the nozzle exit-plane, in such a way that only the sensor filament was immersed in the flow. Acoustic measurements were taken before and after inserting the probe by a far-field microphone which was 4 feet from the probe, and no measurable noise was produced by the presence of the probe in the flow. The filtered hot-film and microphone signal was then cross-correlated for various center frequencies. Then a 1/16" - diameter aluminum rod was placed 2.4 inches downstream of the probe in order to simulate the probe holder stem. The insertion of the rod

increased the SPL 8 dB at the far-field microphone. The cross-correlation functions of the filtered hot-film probe and microphone signals were again measured. Figure 53 shows the cross-correlation function of m_x and p' filtered at 6300 Hz with and without the extraneous noise generated by the rod. The vertical scale on both graphs are the same, so a direct comparison of the amplitudes is possible. The peak value of the cross-correlation function with the simulated probe noise has a lower value than that for the uncontaminated function. However, generally the reverse was true. In any event, the difference in the peak values of the contaminated and uncontaminated cross-correlation functions generally fell within range of repeatability that it was possible to achieve when cross-correlating the same signal successively.

Figure 54A shows the peak values of the cross-correlation functions of m_x and p' filtered by the 1/3-octave filters. It was not possible to obtain cross correlations for the higher center frequencies. This may be because the test room was not anechoic and the reflection of the high frequency sound in the room made the resolution of a well-defined peak impossible. Recall that it is the area under the two curves that is proportional to $R_{p', m_x}(-\tau_0)$. Another test was conducted

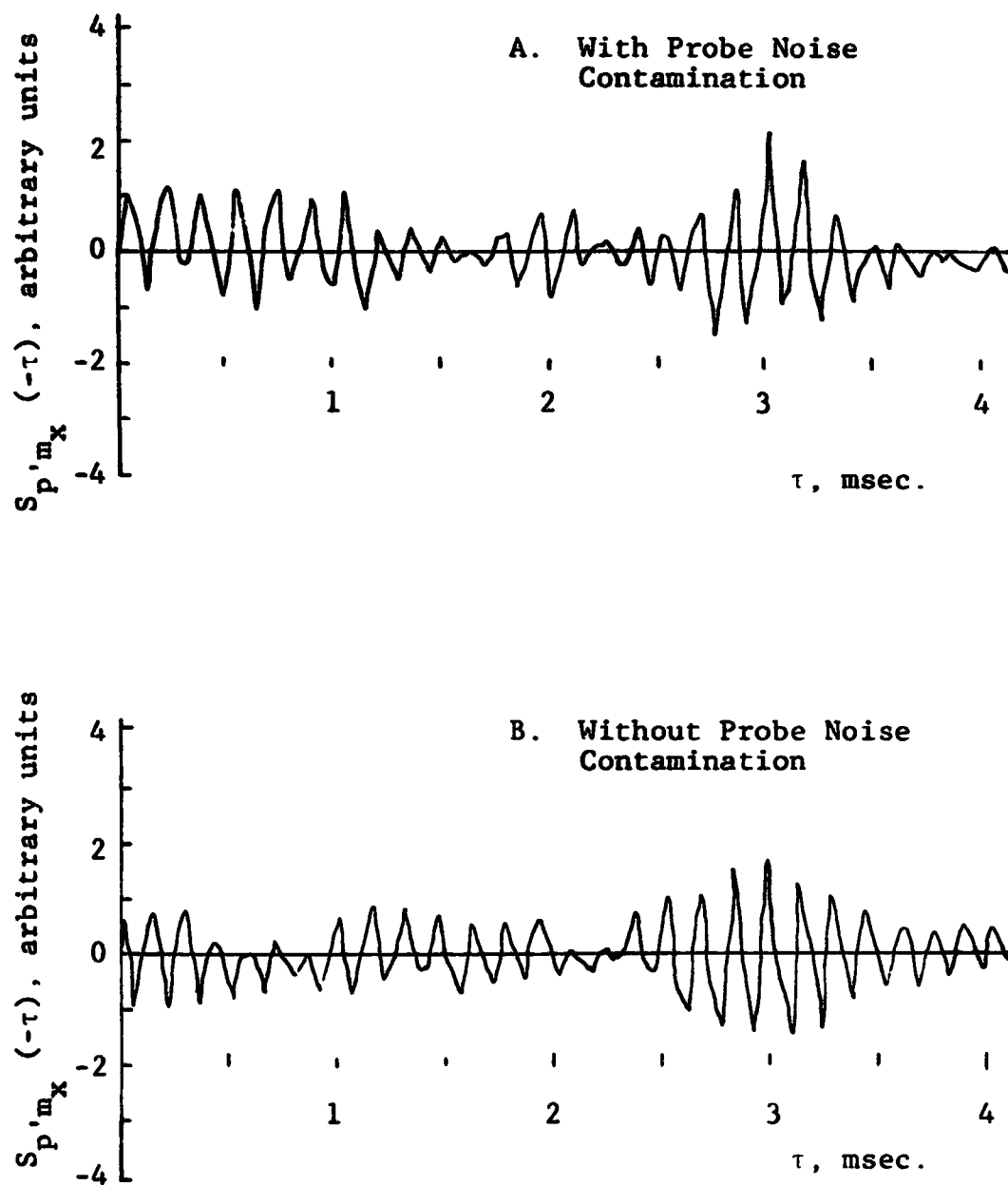


Figure 53. Effect of Probe Noise on the Value of $S_{p'm_x}(-\tau_0)$ Measured for $f_0 = 6300$ Hz.

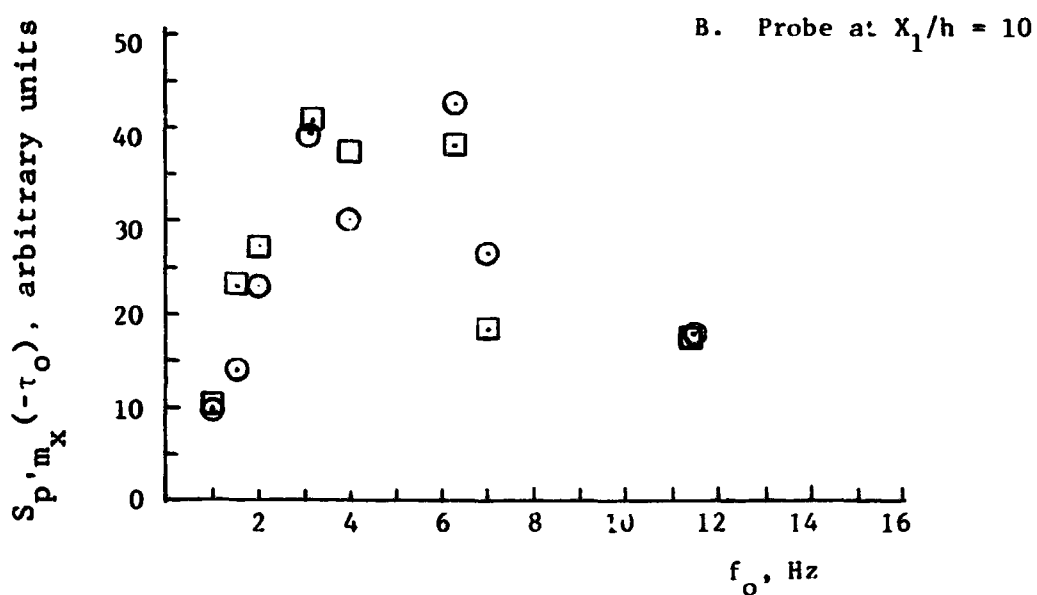
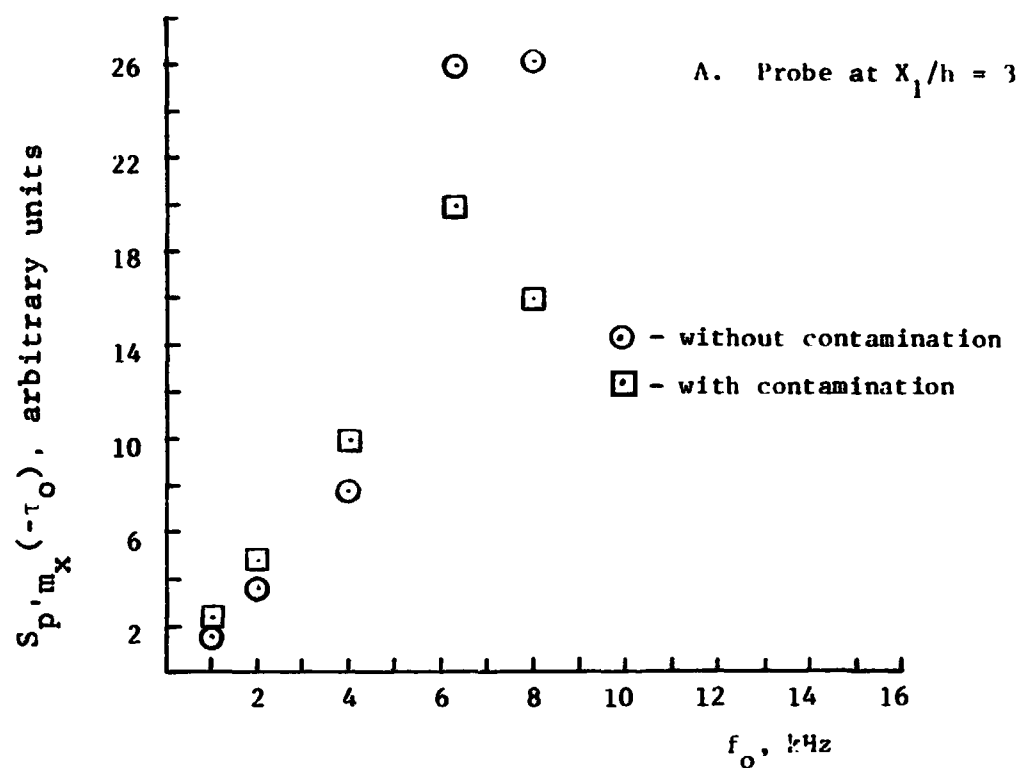


Figure 54. The Effect of Probe Noise Contamination on the Measurement of $S_{p'm_x}(-\tau_o)$

with the probe in the mixing region 10 slot-nozzle heights from the nozzle exit plane. In this test the insertion of the rod increased the SPL only by about 1 dB over the SPL generated by the flow. The results were similar to the first test and are shown in Figure 54B. Based on this data it seems reasonable to conclude that the noise which is generated at the probe-holder stem is not correlated with the turbulent flow fluctuations 8 slot-nozzle heights upstream.